MOLECULAR MECHANISMS OF CELL MIGRATION IN AMOEBOID CELLS

by

Xiaoguang Li

A dissertation submitted to Johns Hopkins University in conformity with the requirements for the degree of Doctor of Philosophy

Baltimore, Maryland

December 2020

Abstract

Chemotaxis is critical during development, tissue repair, immune response and cancer metastasis. The excitable network hypothesis can account for recent observations of propagating waves of signal transduction and cytoskeleton events as well as behaviors of migrating cells. However, the molecular feedback loops involved in these networks that bring about excitability are poorly understood. We show that during random migration and in response to chemoattractants, cells maintain complementary spatial and temporal distributions of Ras activity and PI(3,4)P2 in *Dictyostelium* cells. In addition, depletion of PI(3,4)P2 leads to elevated Ras activity, cell spreading and altered migratory behavior. Furthermore, RasGAP2 and RapGAP3 bind to PI(3,4)P2 and the phenotypes of cells lacking these genes mimic those with low PI(3,4)P2 levels, providing a molecular mechanism. These findings suggest that Ras activity drives PI(3,4)P2 down causing the PI(3,4)P2-binding GAPs to dissociate from the membrane, further activating Ras, completing a positive feedback loop essential for excitability.

Furthermore, we demonstrated that there is an ongoing flow of vesicular PI(3,4)P2 through the cell and a compensatory forward flow along the membrane, which establishes a back-to-front gradient of PI(3,4)P2. Specifically, first, we show that PI(3,4)P2 localized to the lagging edge of *Dictyostelium* and neutrophils. Surprisingly, this lagging edge component also localizes to retracting leading edge protrusions and nascent macropinosomes, even in the absence of PIP3. Second, PI(3,4)P2 is internalized on macropinosomes and transported on microtubules into the cytosol. Once internalized, the macropinosomes break up into smaller PI(3,4)P2-enriched vesicles, which dock and fuse to the plasma membrane at the cell rear. Third, we determined that the PI(3,4)P2 molecules incorporated at the back diffuse along the membrane towards the front, where they are degraded. Last, a stochastic mathematical model confirmed that this cycle

brings about a stable back-to-front gradient. This reverse fountain flow of PI(3,4)P2 in establishing the back-to-front gradient could be essential for polarity in cell migration. Taken together, our findings uncovered a mutually inhibitory Ras-PI(3,4)P2 mechanism essential for excitability, and shed light on the dynamics and role of PI(3,4)P2 in regulating polarity in cell migration. Our work provides novel frameworks to control cell migration in many physiological processes.

Primary Reader and Adviser: Dr. Peter Devreotes

Secondary Reader: Dr. Erin Goley

Acknowledgements

I would like to give my utmost thanks to my excellent mentor Dr. Peter N. Devreotes for his guidance, support, encouragement and unparalleled brainstorming abilities along the journey. I would like to thank all members of Dr. Peter Devreotes and Dr. Pablo Iglesias labs for helpful suggestions. I would like to thank Dr. Marc Edwards, Dr. Zan Chen, Dr. Yang Liu, Dr. Pablo Iglesias, Dr. Sayak Bhattacharya, Debojyoti Biswas, Dhiman Sankar Pal, Nilmani Singh and Dr. Jie Chen for great collaboration.

I would like to extend my gratitude to my thesis committee, including Dr. Carolyn Machamer, Dr. Erin Goley, Dr. Geraldine Seydoux, and Dr. Shigeki Watanabe. I appreciate helpful suggestions from members from the laboratories of Dr. Douglas Robinson, Dr. Chuan-Hsiang Huang, and Dr. Miho Iijima.

I sincerely thank Dr. Yang Liu, Dr. Zan Chen, Wei Xu, Hanjie Jiang, Dr. Chao Yang, Dr. Yize Li, Dr. Hideaki Matsubayashi, Brady D. Goulden and Dr. Brian Graziano for the biological tools and for technical consultant in my projects. I would like to thank support from Dr. Natasha Zachara, Dr. Stephen Gould, Dr. Ryuya Fukunaga, and Darlene Sutton in Biological Chemistry Department, and Brigitte Walsh, Jinna Kim and Wendy Wu in Cell Biology Department. I appreciate all the support from Department of Cell Biology, Department of Biological Chemistry, and JHU Microscope Facility.

I would like to thank American heart association for providing me the predoctoral AHA fellowship. I would like thank U.S. Food and Drug Administration for providing me the ORIES fellowship and thank Dr. Jinzhong Liu for the great mentorship at FDA. I would like to thank peers from outside JHU for providing biological tools and suggestions on my work.

Finally, I would like to thank my family and friends for their unconditional love and support. I share my happiness and pride in completing my Ph.D. with them.

Table of Contents

List of Figures

Chapter 1

Introduction

Modified from:

Xiaoguang Li, Yuchuan Miao, Dhiman Sankar Pal, Peter N. Devreotes**.** Excitable networks controlling cell migration during development and disease. *Seminars in Cell & Developmental Biology*, Volume 100, April 2020, Pages 133-142

1.1 Importance of directed cell migration

Throughout phylogeny, migrating cells possess an internal compass which enables them to sense and move towards or away from gradients of extracellular, soluble chemoattractants or repellants, respectively. In-depth studies over the past century have revealed that chemotaxis plays a crucial role in the development and physiology of uni- and multicellular organisms. In bacteria, archaea and protozoa, cells perform chemotaxis for the purposes of seeking nutrients in the environment, intercellular aggregation and multicellular morphogenesis, and spreading infection within the host (1-3). Apart from chemotaxis, cells possess the ability to sense and move along gradients of other environmental stimuli, such as light, electric fields(4, 5), surface stiffness(6), shear forces, temperature(7), and substrate-bound signaling molecules(8-10).

In metazoans, directed cell migration is required during embryonic development and in adults. During embryogenesis, concerted movement of epithelial sheets bring about gastrulation, while precursor cells residing in different stem cell regions, such as neural crest, brain ventricles, somites and primitive streak, leave their niche and move towards their target sites (11-15). In adults, guided migration is critical for several processes such as trafficking of immune cells towards invading pathogens, coordinated movement of keratinocytes and fibroblasts into the wound site during its healing, motility of sperm towards the egg during fertilization, homing of endogenous stem cells to maintain tissue homeostasis (16-19).

Irregularities in directional migration gives rise to congenital abnormalities, such as neuronal migration disorders, and inflammatory diseases, such as various allergies and infections, atherosclerosis, angiogenesis and cancer metastasis (20-23). The concepts outlined here also shed light on understanding cell migration in development and diseases.

1.2 Varied cellular protrusions in a vast range of physiological functions

Migratory cells move with the help of a diverse array of morphological appendages, which lead to different migration modes. Bacteria, protozoa and sperm rely on flagella and cilia for propulsion and movement (24, 25). Leukocytes and amoebae move by rhythmically extending and retracting discrete actin-rich protrusions, which may appear as wide cup-like structures at the top and sides of the cell or narrower ones situated closer to the substratum. These are traditionally referred to as macropinosomes or pseudopods, respectively (Figure 1A and B) (23, 26, 27). In certain cases of amoeboid motion, due to contractile pressure, the plasma membrane detaches from the actomyosin cortex and causes cytoplasmic extensions or 'blebs' to appear (Figure 1C) (28-30). Keratocytes glide with the help of a single, broad, actin-filled, anterior protrusion and can preserve their shape and direction during motion (30, 31). Mesenchymal cells, such as fibroblasts, move on the extracellular matrix (ECM) with the help of sheet-like lamellipodia and thin, finger-like filopodia, which form at the leading edge of the cell (Figure 1D and E) (32, 33). The attachment to the ECM causes these cells to move at a speed of 0.2-1 μm/min, while cells displaying amoeboid or keratocyte-like migration move at a speed of 5-20 μm/min (34).

Under different physiological conditions, variations of this general scheme can give rise to a diversity of protrusions and migration modes in cells. 1) Blood cells of myeloid and monocytic lineages or metastatic cancer cells form actin-rich ventral projections called podosomes or invadopodia, respectively, which degrade the ECM through secretion of matrix metalloproteinases, and help cells migrate across extracellular barriers (Figure 1F) (35). Interestingly, in patients suffering from Wiskott–Aldrich syndrome, dendritic cells and macrophages have defective podosome formation (36). 2) Polarized epithelial cells display acto-myosin enriched apical regions with broad, F-actin rich lamella-like protrusions at the baso-lateral surface. Their migration is limited due to intercellular interactions (Figure 1G) (37,

38). 3) During oogenesis and embryogenesis, cells move collectively, including Drosophila border cell clusters, which detach from the follicular epithelium and migrate toward the oocyte (39, 40); Drosophila tracheal cell clusters, which branch out to form the tracheal system and zebrafish lateral line primordium, which migrates to form the lateral line sensory system (Figure 1H) (41). 4) Though not technically cell migration, the process of cytokinesis resembles two cells migrating away from each other. Consistently, F-actin rich protrusions and myosin, which segregate to the anterior or posterior regions of migrating cells move to the poles or furrow of dividing cells during cytokinesis (Figure 1I) (42, 43). Thus, varied actin-dependent protrusions are crucial for a vast range of cellular functions, including morphogenesis, tissue regeneration, immunity and cell division.

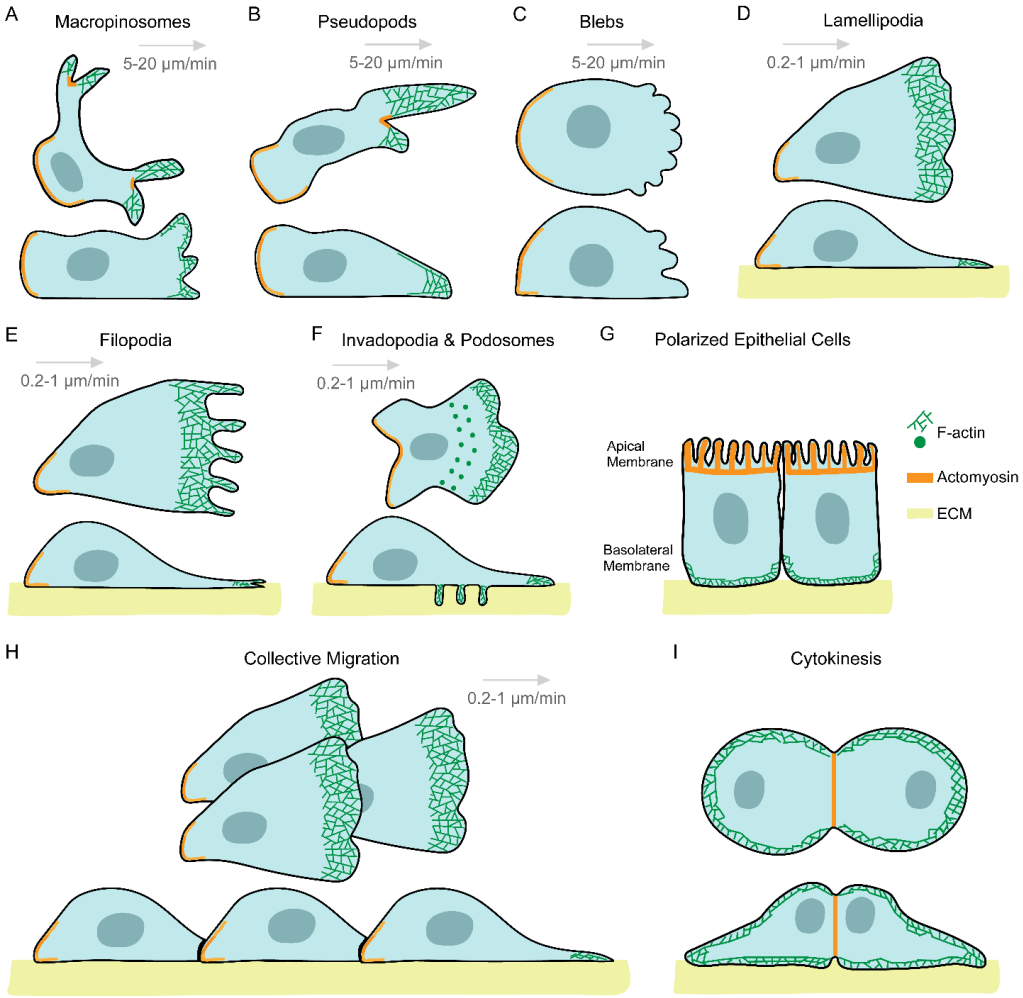

Figure 1. Snapshots of diverse cellular protrusions.

Throughout the illustration, all cells and their protrusions are shown in top (upper) and side (lower) views, except for polarized epithelial cells (G), which is shown only in side view. F-actin is denoted as mesh of green lines, acto-myosin as a heavy orange line, and the extracellular matrix (ECM) is shown in yellow. For migratory cells, the direction of migration is from left to right, as shown with a grey arrow. The respective migratory speeds are mentioned below each grey arrow. Wide and cup-shaped macropinosomes (A) or narrower and longer pseudopods (B) are F-actin rich structures which extend and retract rhythmically near the top and sides of the amoeboid cell, or near the substratum, respectively. (C) In some instances, cells move with the help of bulky cytoplasmic structures or 'blebs' which form by detachment of cell membrane from the actomyosin cortex due to contractile pressure. Cells move at a fast speed of 5-20 μm/min with the help of macropinosomes, pseudopods or blebs. (D) Fibroblasts move on the ECM with the help of a broad, thin, F-actin filled anterior protrusion called lamellipodia. The actin network of these structures sometimes protrudes further to form thin, finger-like projections called filopodia (E). Due to the focal adhesion-based attachment of these cells to the ECM, they move at a far slower speed of 0.2-1 μm/min. (F) Macrophages and some cancer cells form polymerized actin-rich ventral protrusions, referred to as podosomes or invadopodia, which also secrete metalloproteases to degrade the ECM. (G) Epithelial cells polarize along the apical-basal axis and migrate very slowly as epithelial sheets. (H) During oogenesis and embryogenesis, actin polymerization directly pushes forward the plasma membrane of *Drosophila* border cells and Xenopus neural crest cells in the form of a broad lamellipodia, and help the cells to migrate collectively. (I) During cytokinesis, F-actin and actomyosin localize to the poles and cleavage furrow, giving the dividing cell the appearance of two cells migrating away from each other.

1.3 Spatiotemporal regulation of signal transduction and cytoskeletal networks

In migrating cells, many of the signaling molecules, including both lipids and proteins, that mediate polarity and directed cell migration are selectively localized or activated at the leading edge. While others, initially present on the membrane/cortex dissociate from the protrusions. These asymmetrically distributed molecules are referred to as "front" or "back", respectively. A growing list of such spatially restricted molecules is shown in Figure 2A. For example, front events such as Ras, TORC2, PI3K activation, PKB localization or PIP3 accumulation occur at the tips of protrusions of the vegetative and polarized cells, and back events such as PTEN or Myosin II dissociation from pseudopods and localization to the tail of the cells (44-47). We use the terms "events" or "activities" throughout the review to refer to localization/accumulation or activation/deactivation of components. These complementary distributions of molecules and activities are a crucial first step in establishing polarity and guiding cell migration and are maintained even in the absence of a chemoattractant gradient (Figure 2B). The same

complementary pattern of front and back events is observed even when the actin skeleton is disrupted by Latrunculin A. As shown in Figure 2C, in Latrunculin A-treated cells, front components such as PI3K are localized in the cytosol and back components like PTEN are on the membrane. In response to uniform chemoattractant, front components redistribute evenly over the cortex or membrane, whereas back components translocate into the cytosol. When the cells are exposed to a gradient of chemoattractant, front events show an accumulation in a 'dancing crescent' whose orientation oscillates around the direction of the gradient. The behavior of the back events such as PI(3,4)P2 accumulation is diametrically opposed and faces away from the gradient (48) (Figure 2C).

There are situations which parallel migration where these complementary distributions are conserved. For example, during macropinocytosis, the extending edges of the forming cups are decorated with front components like PIP3, whereas back components like PTEN localize to the base (Figure 2D) (49). During cytokinesis, back components move uniformly to the membrane, while front components localized to the cytosol. As the cell elongates, front proteins associate with the cell membrane at the poles while back proteins accumulate at the cleavage furrow together with the acto-myosin ring (Figure 2E) (50). In epithelial cells, front events are localized to the basolateral surfaces, and back events are at the apical side (51) (Figure 2F). In multinucleated mutants or fused giant *Dictyostelium* cells, which display waves of actin polymerization, the same complementary patterns of front and back events are again observed as shown in Figure 2G (52). Most of the basal surface is occupied by back markers, except in the region of actin polymerization where the front molecules appear.

We have observed that cytoskeletal activity alone produces only transient, narrow extensions. Upstream signal transduction networks are needed to provide coordination of cytoskeletal activities across protrusive cellular structures. When accompanied by signal transduction

events, such as Ras and PI3K activation or PTEN inhibition, the protrusions are sustained, reaching out wider or longer (53). The complementary distributions of these front and back events observed have an important role in regulating protrusions. In *Dictyostelium*, the coordinated activity of at least thirteen biosensors suggests that activation of the entire signal transduction network accompanies each protrusion. The molecular components involved in cell migration are remarkably conserved between the social amoeba, *Dictyostelium* and mammalian cells. *Dictyostelium* cells are easily cultivable in the laboratory, well suited for live cell imaging and are naturally migratory cells and have a haploid genome which is completely sequenced and annotated. This makes the amoeba an excellent model system for studies of eukaryotic cell migration (54).

Furthermore, as described below, small shifts in these upstream events can elicit a striking transition in different protrusive activities and migratory modes (44, 55). These observations are not accounted for in the classical view of cell migration. It is believed that different types of protrusions, such as filopodia and lamellipodia, are the results of activations of specific regulators of the actin-myosin cytoskeleton, such as Arp2/3 and formins (56-58), and signal transduction networks merely provide directionality to these protrusions. In the following sections, we discuss emerging insights into the role of spontaneous signal transduction events in the formation of the protrusions.

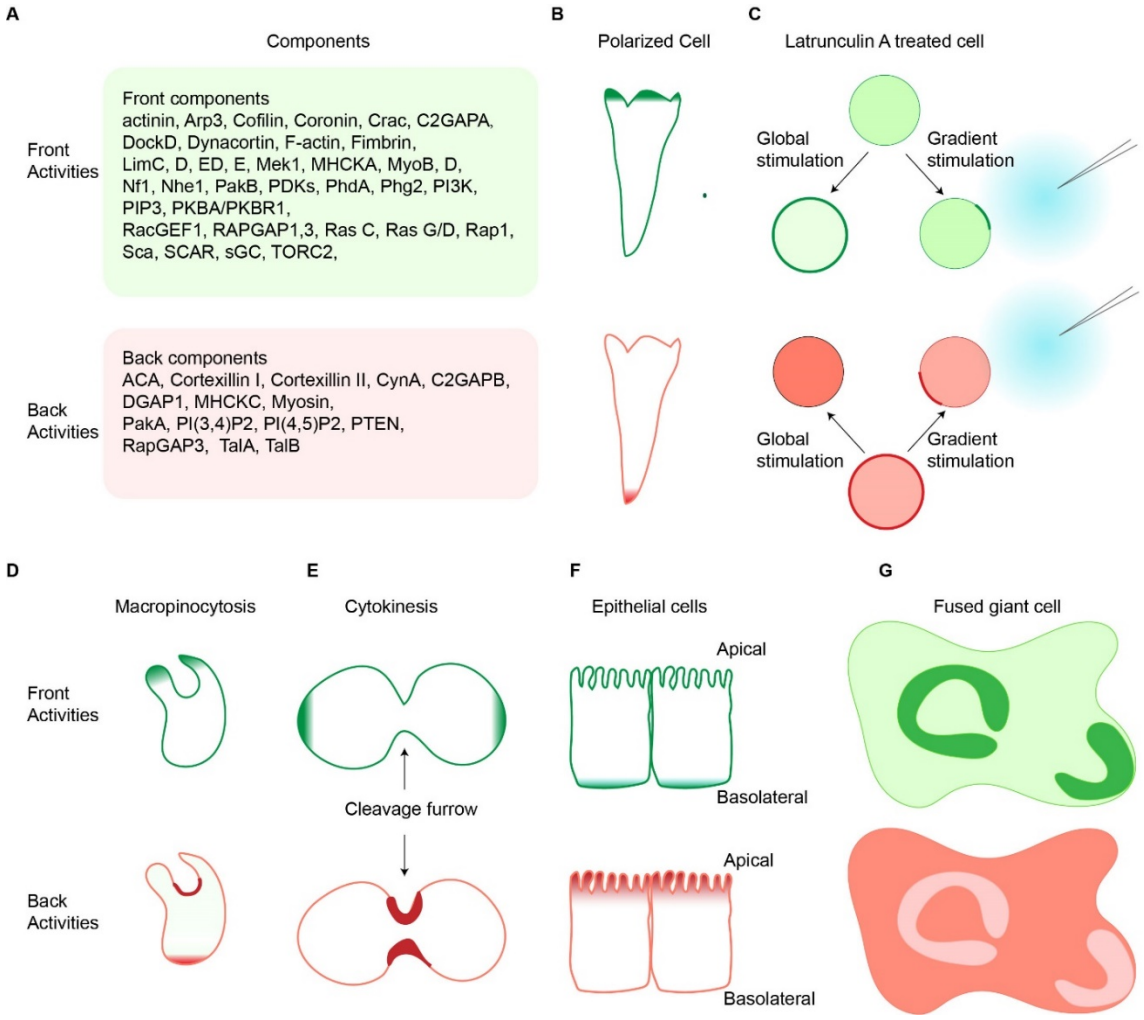

Figure 2. Complementary front and back cellular events.
A. Components of front (up) and back (bottom) are listed. (B). Front activities, such as Ras or PI3K activation, occur at the protrusions of migrating polarized cells, respectively (denoted in dark green, top row). These front activities are complemented with back activities, which localize to the trailing edge of the cells (denoted in red, top row). (C). Upon global or gradient chemoattractant stimulation, latrunculin A-treated cells also show opposite distribution of front (top) and back (bottom) activities. (D). During macropinocytosis, front activities is at the macropinocytic cup, and back activities are at the back of the cup and cell. (E). During cytokinesis, these front molecules are found at the poles of the dividing cells and the back molecules accumulate at the cleavage furrow. (F). In epithelial cells, the front events are localized to the basolateral surfaces (green, top), and the back events are at the apical side (red, bottom). (G). This complimentary pattern of front and back molecules is conserved in fused *Dictyostelium* cells.

1.4 Excitability of signal transduction and cytoskeletal networks

Accumulating evidence points to the fact that these signal transduction and cytoskeletal activities are excitable. Excitability has served as an emerging framework to decipher numerous biological systems, from neuronal action potentials to cardiac calcium waves, from yeast glycolytic oscillations to vertebrate segmentation. Excitable systems have characteristic

hallmarks such as all-or-none response, refractoriness and wave propagation. Quantitative measurement in *Dictyostelium* has directly demonstrated the excitable nature of the signal transduction and cytoskeletal networks. For example, Huang et al. showed that activation of Ras, in response to short and long supra-threshold stimuli is the same and are followed by a refractory period of ~50 seconds (59). Consistently, signal transduction and cytoskeletal constituents propagate as waves on the cortex and annihilate when oppositely-directed waves collide, further supporting the existence of excitability (see Figure 2E) (60). With similar observations being described in other cell types including neutrophils (61, 62), macrophages (63), and mast cells (64-66), excitability is likely a conserved feature of many molecular networks.

The signal transduction and cytoskeletal events appear to operate as distinct, yet closely interacting, excitable systems. In *Dictyostelium*, molecular events in cell migration can be broadly classified into two networks, the Signal Transduction Excitable Network (STEN) and the Cytoskeletal Excitable Network (CEN) (Figure 3A). Differences between STEN and CEN are manifested in their responding kinetics to global stimulus, as well as localization morphologies in spontaneous wave patterns. In response to cAMP addition, STEN components, including phospholipids, Ras/Rap small GTPases, and PKBs, show a level/activity increase with kinetics slower than CEN components including F-actin, Rac, coronin, and HPSC300. Consistently, in spontaneous traveling waves, STEN components show diffuse bands while CEN display sharp 'two-peak' morphologies and puncta associated with the trailing peak (Figure 3B). These differences in kinetics and localization highlight the intrinsic differences in excitability between STEN and CEN. On the other hand, STEN and CEN are closely coupled and entrained. Acute perturbations at different nodes suggest that STEN drives CEN to form waves. CEN also regulates the triggering of STEN, possibly through RapGAP1 and GflB (55).

Future work is required to reveal more detailed biochemical interactions and integrate them on a systematic level.

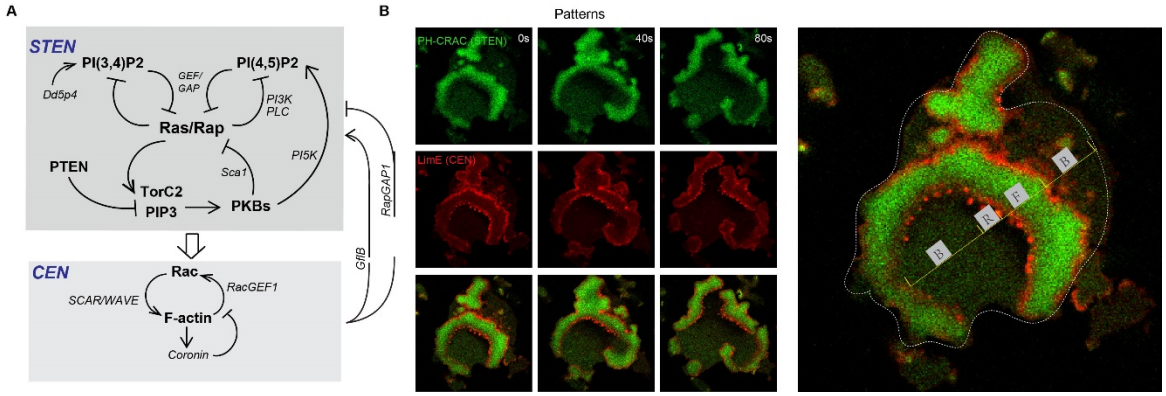

Figure 3. Summary of STEN and CEN networks with positive and negative feedback loops.
(A) Positive feedback in STEN is brought about by mutual inhibition between Ras/Rap activity and PI(3,4)P2 and PI(4,5)P2 at the cell cortex and delayed negative feedback due to PKB activation by PIP3 and TorC2. (B). The corresponding B, F, and R states are depicted on basal surface of a fused *Dictyostelium* cell. Time-lapse Confocal images (left) showing distribution of LimE (red) and PHcrac (green) during wave propagation at the basal surface of a migrating fused *Dictyostelium* cell. White dashed line marks the outline of the fused cell (Right). F represents the F state, B represents the B state and R represents the R state. The B-state region is characterized by low Rap/Ras, TorC2, and PI3K activity and high PI(3,4)P2 and PI(4,5)P2 levels. As a region transitions to the F-state, Rap/Ras activity increases, PI(3,4)P2 decreases strongly, and PI(4,5)P2 decreases slightly. There is a slower rise in PKB activity due to the elevation of TorC2 and PIP3. A refractory period (R state) follows associated with lower Rap/Ras activity and higher PI(3,4)P2/PI(4,5)P2 levels and PKB activity. The PKBs feed into CEN, promoting F-actin polymerization and loss of cortical myosin. In turn, the activated cytoskeletal activity provides fast positive and slow negative feedbacks to STEN.

1.5 Wave patterns, cortical dynamics and cellular protrusions.

The idea that wave propagation controls protrusion formation has been supported by recent evidence. It was found that fast undulations of CEN cover the cell periphery, but sustained protrusions are only formed when significant STEN activities drive CEN to support wave propagation (47, 53, 55, 59). Furthermore, the dynamic properties of wave propagation closely mirror those of pseudopods in migrating cells. Innately, waves of STEN and CEN have limited range – they gradually decrease speed and eventually extinguish rather than propagating persistently. Similarly, pseudopods only grow to a defined size before collapsing rather than expanding continually (67, 68). Thus, STEN and CEN waves, serving as the drivers of protrusions, can account for the extension and retraction dynamics of pseudopods.

Recent experiments with acute perturbations further support the causal relationship between wave properties and protrusion determination (Figure 4). First, within minutes of lowering threshold of STEN activation, by decreasing PIP2 or increasing Ras/Rap activities using chemically induced dimerization, waves propagate with elevated speed and range. Consequently, narrower pseudopods become wider lamellipodia-like protrusions and the cell migratory mode shifts from amoeboid to keratocyte-like and oscillatory (Figures 4B and F). Second, increasing PKBs activities produces negative feedback in STEN, but also promotes coupling between STEN and CEN. This raises the threshold of STEN, and simultaneously lowers threshold of CEN, leading to slower wave propagation and more wave initiation centers (Figure 3A). This generates numerous spiky filopodia-like protrusions (Figures 4C and G). Similarly, recruiting RacGEF1 to the membrane produces positive feedback in CEN, and delayed negative feedbacks in STEN. This lowers the threshold of CEN and increases threshold of STEN, leading to disrupted wave patterns and many diffuse actin patches (Figure 3A). As a result, sustained protrusions cannot be formed due to a lack of wave propagation, and the cells generate ruffles on the cortex and lose the ability to move (Figures 4D and H). All these transitions occur in a much faster time scale than that of gene regulation. Thus, tweaking the feedback loops within and between STEN and CEN leads to a range of wave patterns, which results in a spectrum of interchangeable cellular protrusions.

Future work is needed to advance the hypothesis that set points of the STEN-CEN machinery determine various types of cellular protrusions. Sophisticated higher resolution imaging is required to directly visualize and analyze wave propagation patterns at sites of different protrusions, given the challenges posed by the highly dynamic and three-dimensional nature of the cortex of migrating cells. Moreover, the extent to which this model is conserved must be tested. It is possible that different cells types have different expression levels of the STEN-

CEN components innately, which holds the networks of each cell at a specific set point. Thus, different cells display specific types of protrusions predominantly. Finally，the connection between the wave properties and specific cytoskeleton nucleators needs investigation.

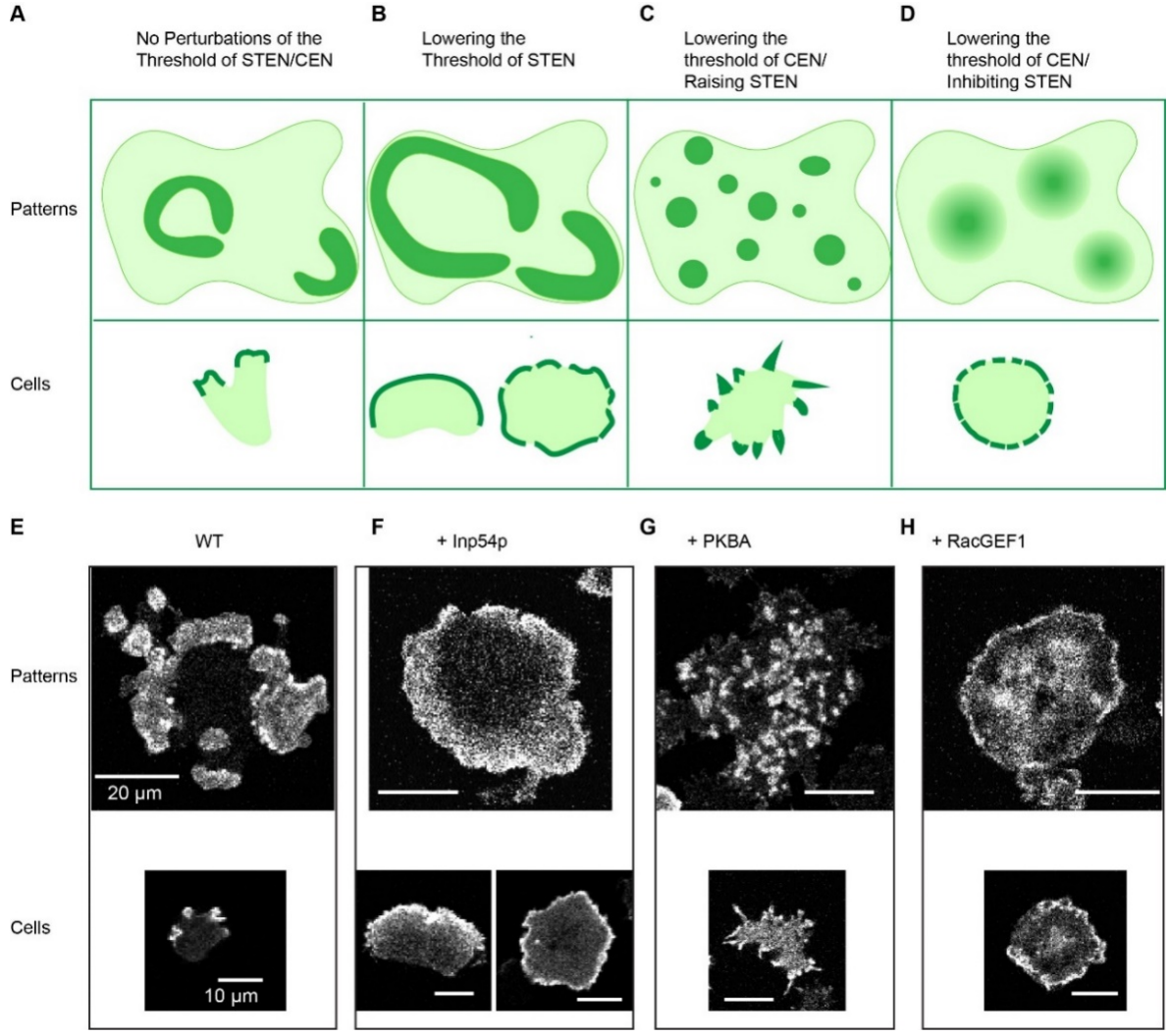

Figure 4. Cartoon of Perturbations and different wave patterns & cellular protrusions.
(A-D). Cartoons depicting the cortical wave patterns corresponding to cellular morphology in fused giant cells (top) or single cells (bottom). Cells without perturbations of the threshold of STEN/CEN (A); with perturbations of lowering the threshold of STEN (B); with perturbations of lowering of the threshold for CEN/raising that of STEN (C); with perturbations of lowering of the threshold of CEN/removing STEN (D). (E-H) Confocal images corresponding to (A-D), showing LimE patterns (CEN) on the basal surface of fused *Dictyostelium* cells (top) and on the protrusions of single cells (bottom). Cells without perturbations of the threshold of STEN/CEN. (E); with perturbations of lowering PI(4,5)P2 by recruitment of 5-phosphatase Inp54p (lowers the threshold for STEN) (F); with perturbations of recruitment of PKBA (lowers the threshold of CEN and raises that of STEN) (G); with perturbations of recruiting RacGEF1 (lowers the threshold of CEN/extinguishes STEN) (H). Scale bar top 20µm, bottom 10µm.

It is interesting to note that blebs, usually thought to be controlled by hydrostatic pressure rather than any actin regulators, are nevertheless associated with Ras activation (Figure 5), pointing to the possibility of using the STEN-CEN framework to fully comprehend bleb formation.

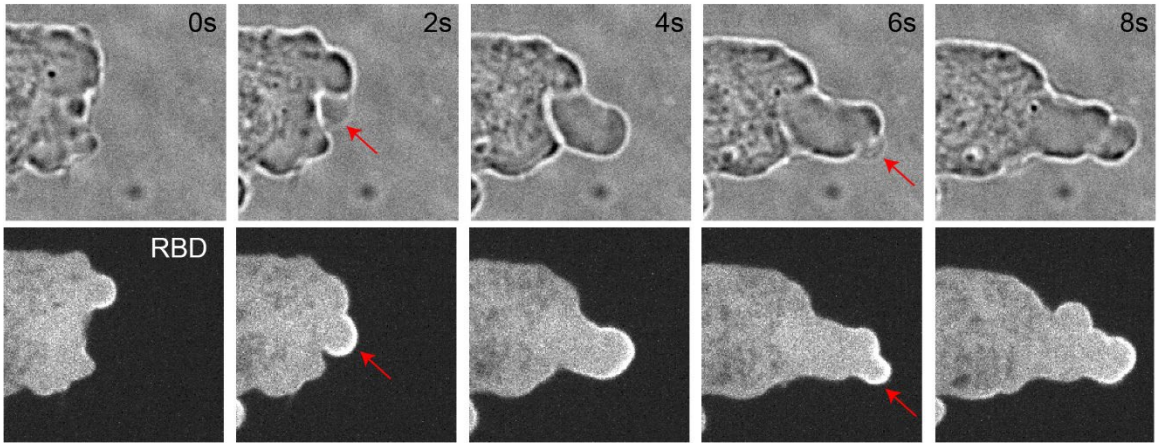

Figure 5. Blebs are associated with Ras activation.
The time-lapse confocal images of the same cell were obtained every 2 s. Confocal images showing blebs under bright field (top) and Ras activity sensor, Ras-binding domain of Raf-1 (RBD-GFP) under confinement in *a Dictyostelium* cell. Red arrows point to newly forming blebs.

1.6 Molecular mechanisms giving rise to excitability.

Activator-inhibitor systems are typically used to explain wave propagation and excitability. In these systems, the activator is controlled by an autocatalytic loop, and generates the inhibitor, which provides negative feedback to the activator (69). Further refinement of this model proposes that local regions of the cell cortex transition between inactive, active, and refractory states, designated as B, F, and R, respectively. Mutual inhibition between the B and F states creates the positive feedback loop. The F and R states are related through a delayed negative feedback loop. In resting cells, most of the cortex is in the B state. Once initiated, waves propagate outwardly because diffusion of F state components triggers activation in adjoining B but not R region (70). Computational analyses based on such reaction–diffusion equations are able to simulate the distributions of F, B and R during wave propagation.

My thesis reported the mutually inhibitory interactions between Ras/Rap and PI(3,4)P2/ PI(4,5)P2 activities comprise a positive feedback loop, consistent with assigning these components as F and B, respectively. When cells are stimulated, Ras is activated, while PI(3,4)P2 levels drop significantly, and PI(4,5)P2 levels drop slightly. When PI(3,4)P2 levels are lowered with genetic or synthetic tools in the cells，Ras/Rap activities are elevated (Figure 3A). Purified Lowe oculocerebrorenal syndrome protein (OCRL) homolog, Dd5P4, has been shown to generate PI(3,4)P2 from PI(3,4,5)P3 in vitro, and Li and Edwards et al have reported PI(3,4)P2 level is low in Dd5P4 null cells. An example is shown in Figure 6, wild-type cells display one to three small patches of Ras activity, but the Dd5P4 null cells, which have lower PI(3,4)P2 levels, display higher Ras activities.

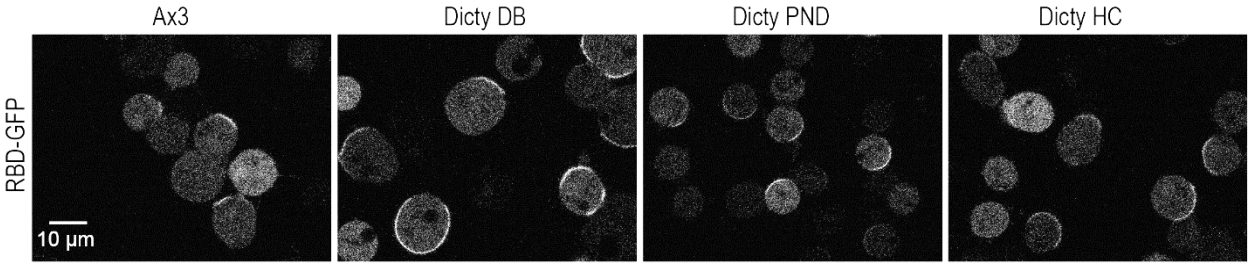

Figure 6. RBD activities in wild-type Ax3 cells and in Dd5P4- cells.
Confocal images showing RBD patches in wild-type Ax3 cells and three independently generated *Dd5P4-* cell lines. *Dd5P4-* cells from Dictybase stock center, *Dd5P4-* cells from Devreotes lab, Dd5P4- cells from Cai lab. Cells are treated with Latrunculin A for 20 min. Scale bar 10μm.

Similarly, Miao et al found that acute lowering of PI(4,5)P2 levels promotes Ras/Rap activities. These regulations of Ras/Rap activities by PI(3,4)P2/ PI(4,5)P2 may occur through GEF and GAP proteins. In fact, Li and Edwards et al found that PI(3,4)P2 binds to and regulates RasGAP and RapGAP proteins(48). These results add to the emerging role of PI(3,4)P2 in multiple cellular processes as elaborated in Figure 7.

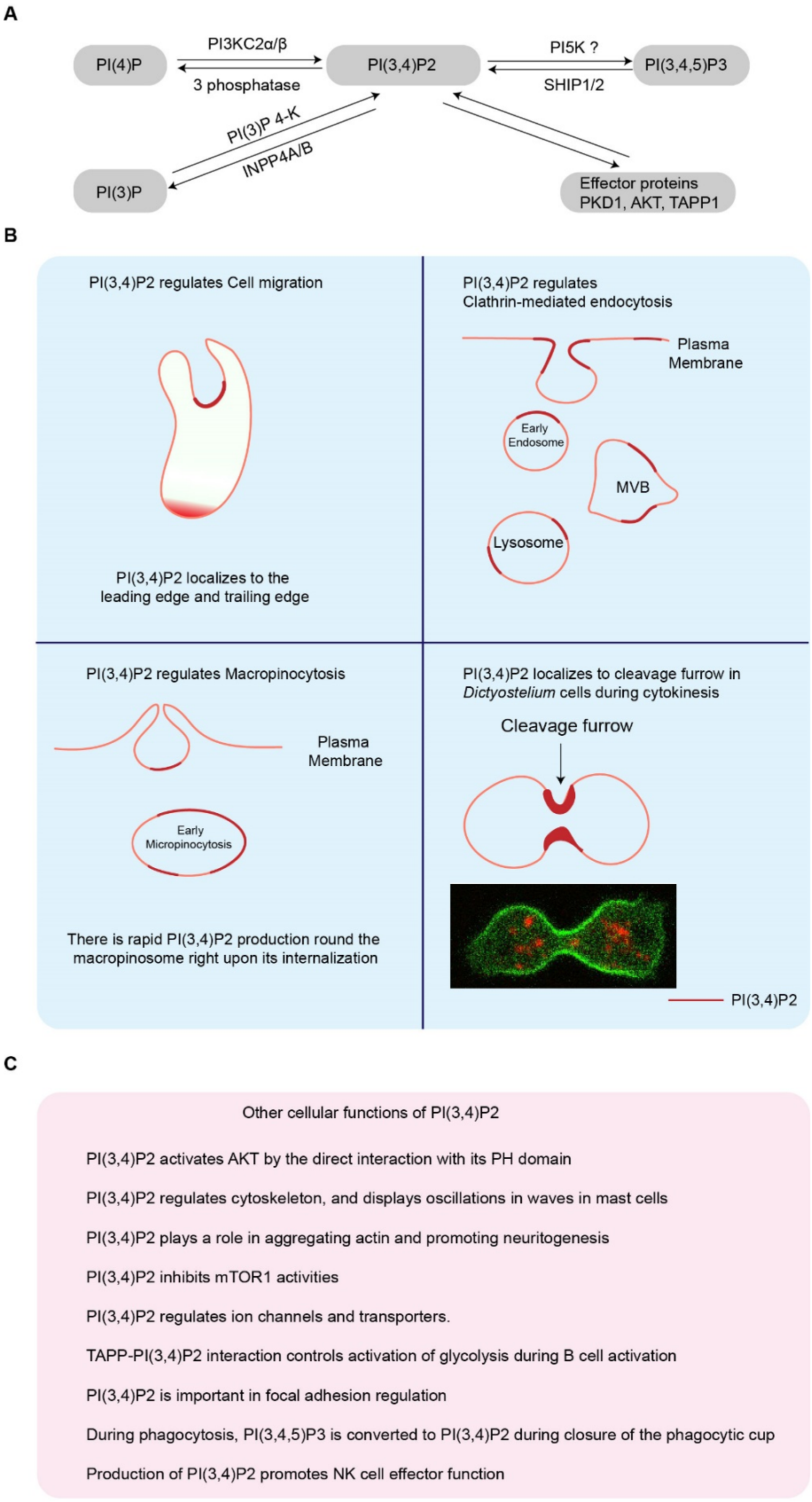

Figure 7. The cellular functions of PI(3,4)P2.

(A). PI(3,4)P2 metabolism pathways. (B). Dynamics, localization, and roles of PI(3,4)P2 during cell migration, endocytosis, macropinocytosis and cytokinesis (71-73). PI(3,4)P2 localizes to the leading edge and lagging edge

during cell migration (48, 74-76). PI(3,4)P2 localizes to the early endosome, multivesicular body (MVB), and lysosome during clathrin mediated endocytosis (77-80). PI(3,4)P2 localizes to the back of the macropinocytic cups and early macropinosomes during micropinocytosis (79, 81-85). PI(3,4)P2 localizes to the cleavage furrow during cytokinesis (C). The other cellular functions of PI(3,4)P2 highlighted in pink box. PI(3,4)P2 activates AKT by the direct interaction with its PH domain(86). PI(3,4)P2 regulates cytoskeleton, and displays oscillations in waves in mast cells (63, 65, 87). PI(3,4)P2 plays a role in aggregating actin and promoting neuritogenesis (88). PI(3,4)P2 inhibits mTOR1 activities(89). PI(3,4)P2 regulates ion channels and transporters (90, 91). TAPP-PI(3,4)P2 interaction controls activation of glycolysis during B cell activation(92). PI(3,4)P2 is important in focal adhesion regulation(93). During phagocytosis, PI(3,4,5)P3 is converted to PI(3,4)P2 during closure of the phagocytic cup(94). Production of PI(3,4)P2 promotes NK cell effector function(95).

As positive feedback grows, negative feedback builds in a delayed manner. Charest et al. found that *Dictyostelium* cells lacking PKBA and PKBR1 display persistently high RasC activity in pull-down assays, suggesting a negative feedback loop involving the phosphorylation of upstream components by downstream PKBs (96, 97) . Miao et al. showed that in immobilized cells lacking PKBs, RBD patches are more frequent but the patches are rapidly quenched by recruitment of PKBA (55). These observations suggest that activation of PKBs serves as a negative feedback loop. Possible mechanisms may include inhibition of RasGEF, Aimless, and activation of PI5K to increase PI(4,5)P2 synthesis. Interestingly, PIP3 as an activator of PKBA, plays a negative role in STEN, while it is also an important positive regulator of actin polymerization. This may occur through a series of PKBA substrates (Figure 3A).

Some other feedback loops have also been described. For example, a positive-feedback loop appears to link cytoskeletal events and PIP3 because inhibition of either reduces the spontaneous activation of the other (98, 99). There is other evidence that such a positive feedback path involving Ras exists (100). It has been reported that the cortex of vertebrate and invertebrate oocytes and embryos is also an excitable medium. Positive feedback is mediated by Rho autoactivation and negative feedback is mediated by F-actin-mediated Rho inhibition (101). Taken together, these suggest that individual molecular regulators of various protrusions are feeding into the same overall molecular machinery. Global properties and feedback loops

of the Ras/Rap-centered STEN and Rac/F-actin centered CEN are the true determinants of controlling the entire spectrum of protrusions observed in cell migration.

Chapter 2

Mutually Inhibitory Ras-PI(3,4)P2 Feedback Loops Mediate Cell Migration

Modified from:

Xiaoguang Li, Marc Edwards, Kristen F. Swaney, Nilmani Singh, Sayak Bhattacharya, Jane Borleis, Yu Long, Pablo A. Iglesias, Jie Chen, and Peter N. Devreotes. Mutually Inhibitory Ras-PI(3,4)P2 Feedback Loops Mediate Cell Migration. *PNAS*. 2018 Sep 25;115(39):E9125-E9134.

2.1 Summary

Cell migration is central in physiological and pathological conditions such as immune response and cancer metastasis. The excitable network hypothesis can account for recent observations of propagating waves of signal transduction and cytoskeleton events as well as behaviors of migrating cells. However, the molecular feedback loops involved in these networks that bring about excitability are poorly understood. Here we provide evidence for a positive feedback loop based on a mutual inhibitory interaction between Ras and the phosphoinositide PI(3,4)P2. Our results uncover a novel and important role of PI(3,4)P2 in the regulation of Ras activity, which may extend well beyond cell migration.

2.2 Introduction

Cell migration mediates a large number of key physiological activities during development and in the adult. These processes require coordination of signal transduction and cytoskeletal events, which regulate the dynamics and localization of cellular protrusions and contractions. For instance, local activations of Ras GTPases and PI3K pathways link to Rho GTPases, which mediate cytoskeletal rearrangements (10, 98-100, 102, 103).

The behavior of the signal transduction and the cytoskeleton networks suggest that they are excitable, and has led to the "excitable network hypothesis" for cell migration (69). In migrating *Dictyostelium* cells, waves of Ras and PI3K activation, propagate along the cell cortex, while back protein, PTEN, dissociates from the membrane generating coordinated "shadow" waves. Theoretical models of excitability involving activator-inhibitor feedback loops have been remarkably successful in accounting for the behaviors of migrating cells but the molecular events comprising the loops are not well understood (104-108).

Phosphoinositides have played a prominent role in the molecular definition of excitable signal transduction networks. PI(3,4,5)P3 and PI(4,5)P2, the product of PTEN, have come to characterize the front (F) and back (B) states in excitable network models (109). Evidence of PI(4,5)P2 accumulation at the rear of cells and in the furrow during cytokinesis has supported these models (110, 111). Synthetic depletion of PI(4,5)P2 leads to significant hyperactivation of cellular protrusions. However, in migrating cells, back to front gradients of PI(4,5)P2 are modest, suggesting the existence of more important regulators of back activities. PI(3,4,5)P3 can also be converted to PI(3,4)P2. This phosphoinositide has been associated with phagocytosis and pinocytosis, but its role in cell migration is relatively understudied (71, 74, 77, 79, 94, 112, 113).

In a previous study, we identified a novel pleckstrin homology (PH) domain-containing *Dictyostelium*-specific back protein, Callipygian (CynA), which binds to membranes, dissociates selectively from protrusions, and associates with the rear of polarized cells (114). This promotes polarity and increases migration efficiency. Here we characterize CynA's binding partner PI(3,4)P2 and provide evidence for the existence of a mutually inhibitory positive feedback loop between Ras and PI(3,4)P2. This regulatory feedback loop appears to be a major regulator of the signal transduction network excitability, and therefore a critical controller of cellular protrusions and migration modes.

2.3 Results

2.3.1 Back to Front Gradient and Transient Chemoattractant-Induced Depletion of PI(3,4)P2

We used a chemically inducible dimerization system in *Dictyostelium* to clamp PIP2 at low levels or the activities of Ras/Rap GTPases at high levels, as would be expected to transiently Figure 8 shows the behavior of CynA in relation to spontaneous actin polymerization in a randomly migrating cell. As previously reported (114), a tandem PH-domain biosensor, tPHCynA-KikGR, is depleted from actin-rich protrusions at the front of cells (Figure 8A). A resulting gradient in tPHCynA-KikGR membrane association from back to front is apparent. Kymographs of the cell perimeter show that this dynamic relationship is tightly maintained as the cell migrates (Figure 8B). A construct with four PH-domains, ttPHCynA-GFP, which may have greater sensitivity, detected a similar gradient but it extended further along the sides toward the front in polarized cells (Figure 9A).

Several assays of supernatants from cells expressing CynA-derived constructs indicate that these proteins are biosensors for PI(3,4)P2. When applied to filters spotted with multiple phosphoinositides ("PIP-strips"), CynA-GFP, tPHCynA-GFP, and ttPHCynA-GFP bound strongly to PI(3,4)P2, slightly to PI(3,4,5)P3, and negligibly to all other lipids (Figure 8C, and Figure 9B and C). Controls with supernatants from cells expressing PHCrac-YFP, showed preferential binding to PI(3,4,5)P3, to a lesser extent to PI(3,4)P2, while PHPLCδ-YFP showed binding to PI(4,5)P2 (Figure 9C).

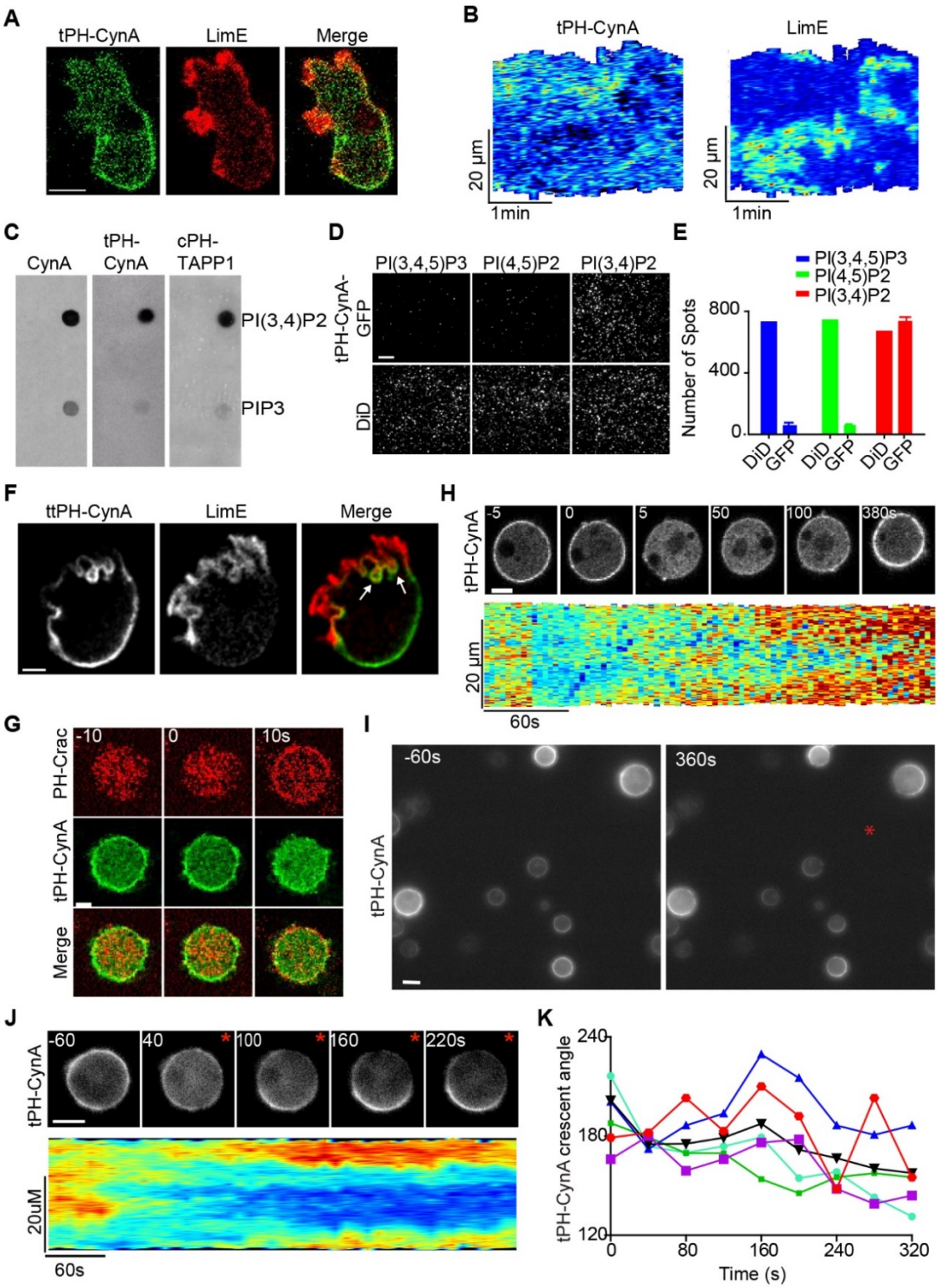

Figure 8. Back to Front Gradient of PI(3,4)P2.
(A) Growth stage wild-type Ax3 cell co-expressing tPHCynA -KikGR (green) and LimE-RFP (red). (B) Kymographs of tPHCynA and LimE intensity on the perimeter of cell in (A) undergoing random migration. Confocal images collected at 5 s intervals. Scale bars represent 5 µM.(C) Binding of supernatants from cells expressing full length CynA-GFP, tPHCynA -GFP, or cPHTAPP1 –GFP to PIP strips. (D) "Pull-down" assay showing TIRF images of tPHCynA -GFP binding to tethered vesicles containing PI(3,4,5)P3, PI(4,5)P2, or PI(3,4)P2 (top row). DiD staining of vesicles (bottom row).(E). Quantification of tPHCynA -GFP binding in "pull-down" assays. Background fluorescence spots in the GFP channel obtained by adding lysates to vesicles

lacking PIs were subtracted from all samples. Error bars are SEM.(F) Growth stage wild-type Ax2 cell co-expressing ttPHCynA -GFP (green) and LimE-RFP (red). (G) 4-hour stage wild-type Ax3 cells expressing PHCRAC -RFP and tPHCynA -GFP were treated with 5 μM latrunculin A for 20 min and then stimulated with cAMP. Time-lapse confocal representative images showing redistributions of PHCRAC -RFP (red) and tPHCynA -GFP (green) in the same cell. Images were collected at -10, 0, and 10s. Scale bars represent 5 μM.(H) Confocal images of tPHCynA -GFP (top) in independent experiment similar to that in (A) at representative times. Corresponding kymograph of cortical tPHCynA intensity (bottom). Scale bars represent 5 μM.(I) Field of 4-hour stage wild-type Ax3 cells expressing tPHCynA -KikGR 60s before and 360s after exposure to a micropipette containing 1 μM cAMP. Scale bars represent 10 μM.(J) Time-lapse images of an individual cell in the micropipette assay. Kymograph of the cortical tPHCynA -KikGR intensity is shown at bottom. Scale bars represent 5 μM. (K) Fluctuations in the angle of the tPHCynA -GFP crescents. To determine the positions of the crescents, the angle was defined by measuring the angle formed by two lines: the line drawn between the centroid of the cell and the center of the crescent, and the line drawn between the centroid of the cell and the tip of the micropipette. Crescent fluctuations of four cells from experiments in (I) are shown. (n=6).

Similarly, in a TIRF microscopy-based assay, CynA-GFP, tPHCynA-GFP and ttPHCynA-GFP bound specifically to surface-tethered lipid vesicles containing PI(3,4)P2, with little binding to vesicles containing PI(3,4,5)P3 or PI(4,5)P2, or controls (Figures 8D and E, and Figure 9D-K). Control supernatants from cells expressing PHPLCδ-GFP showed binding to PI(4,5)P2 (Figure 9L). In addition to its localization at the back, ttPHCynA-GFP was also found to be associated with focal patches at the base of protrusions at the front, as was another PI(3,4)P2 sensor, C-terminal PH domain of TAPP1 (cPHTAPP1-GFP). On “PIP-strips” cPHTAPP1-GFP associated strongly with PI(3,4)P2 and slightly with PI(3,4,5)P3 (Figure 8C), like tPHCynA-GFP.

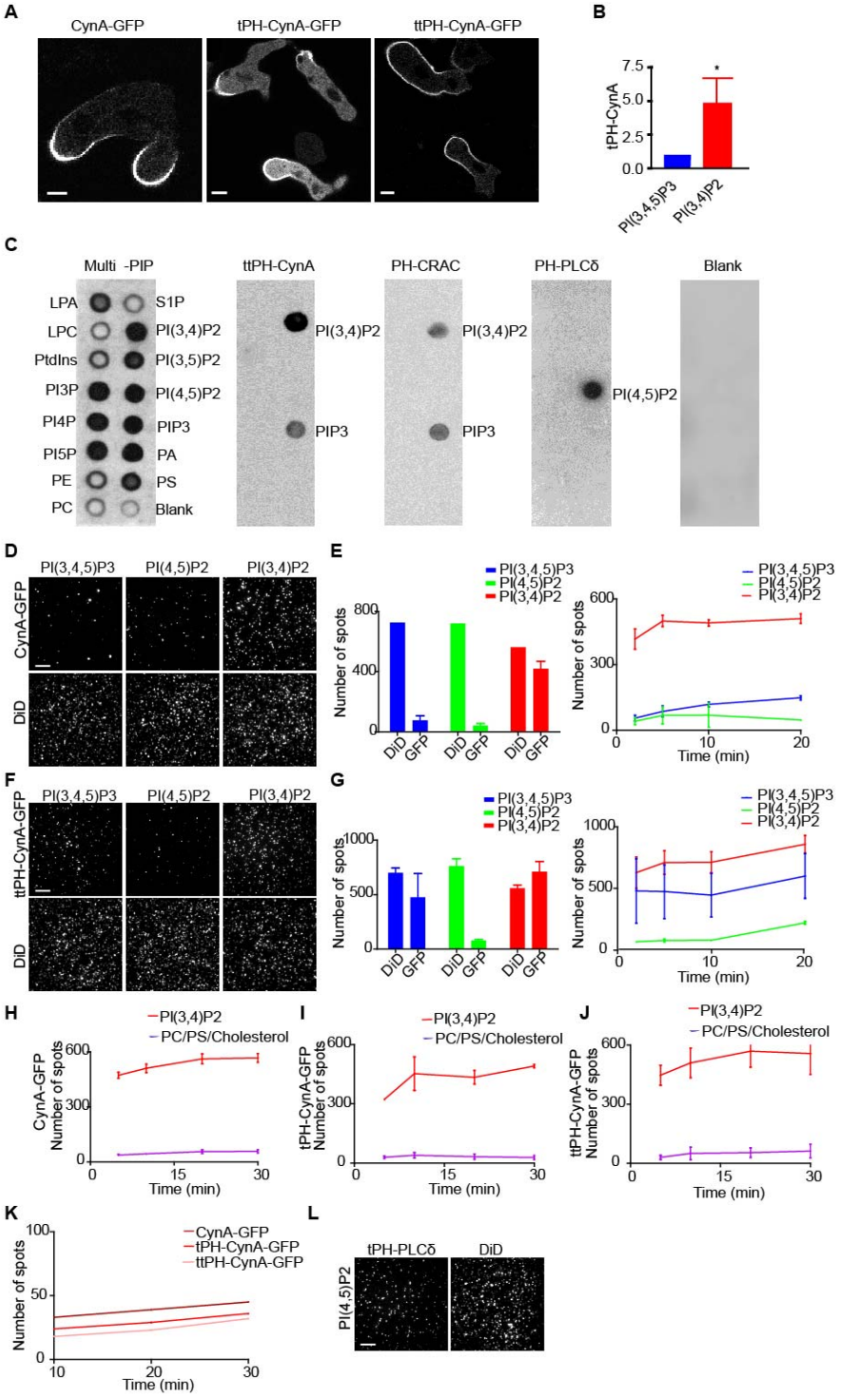

Figure 9. Binding specificities of PIs.

(A) Confocal images of CynA-GFP, tPH$_{CynA}$-GFP, and ttPH$_{CynA}$-GFP in randomly migrating growth-stage, wild-type Ax3 cells. (B) Quantification of tPH$_{CynA}$-GFP binding specificity, normalized to intensity of PI(3,4,5)P3 spot. *P < 0.05 versus; Data are represented as mean ± S.E.M. (C) "PIP" strips of multi-PIP, ttPHCynA-GFP, PH$_{Crac}$-YFP, PH$_{PLC}$-YFP and an empty vector blank control. (D and F) TIRF images of "pull-down" assays with vesicles containing indicated phosphoinositides incubated with supernatants of cells expressing CynA-GFP and ttPH$_{CynA}$-GFP (top rows). Vesicles stained with DiD (bottom row). (E and G) Quantification of CynA-GFP (E) and ttPH$_{CynA}$-GFP (F) "pull-down" assays in (D) and (F). Background fluorescence spots in the GFP channel obtained by adding lysates in the absence of lipid vesicles were

subtracted from all samples. Error bars: SD of data from 10 or more imaging areas. (H-J) Quantification of CynA-GFP (H), tPH_{CynA}-GFP (I) and $ttPH_{CynA}$-GFP (J) "pull-down" assays. Background fluorescence spots in the GFP channel obtained by adding lysates in the absence of lipid vesicles were subtracted from all samples. Error bars: SD of data from 10 or more imaging areas. (K) Quantification of CynA-GFP, tPH_{CynA}-GFP and $ttPH_{CynA}$-GFP "pull-down" assays of no vesicles control. (L) TIRF images of PI(4,5)P2 containing vesicles incubated with supernatants of cells expressing tPH_{PLC}-GFP (left) in HEK293 cells. Vesicles stained with DiD (right).

However, association of cPHTAPP1-GFP with the back of the cell was not apparent (Figure 9F, Figure 10A). In mammalian cells, TAPP1 has been reported to localize to the front (31), while in zebrafish neutrophils, it was found at the leading and trailing edges (74). To resolve these apparent discrepancies, we reexamined the distribution of the cPHTAPP1-GFP. We reasoned that perhaps the TAPP1 biosensor lacked sufficient sensitivity for detection at the back of the cell during live cell imaging. To assess this possibility, we fixed cells. Under these conditions it was clear that cPHTAPP1-RFP was also present on the membrane in a gradient from back to front which resembled that detected by tPHCynA-KikGR (Figure 10A).

Since PI(3,4)P2 is a product of PI(3,4,5)P3, which increases during cell activation, one might expect PI(3,4)P2 to also increase; instead, it decreased. In cells treated with latrunculin A, tPHCynA-KikGR displayed a relatively uniform distribution around the cell perimeter. Within 10 seconds of addition of chemoattractant, cAMP, tPHCynA-KikGR dissociated from the membrane and moved to the cytosol, indicating a decrease in PI(3,4)P2. Simultaneously, PI(3,4,5)P3 on the membrane increased as previously shown (Figure 9G). The PI(3,4)P2 decrease was transient with levels returning to baseline and exceeding it by 380s (Figure 9H, Figure 10B). The magnitude of the response in individual cells varied, but the kinetics were similar (Figure 10C). Using a fixation protocol, we also detected a drop of cPHTAPP1-RFP binding to the membrane (Figure 10D and E). We also assayed phosphoinositide levels and phosphorylation of downstream Ras effector PKBR1 following lysis in the presence and absence of cAMP plus GTPγS. Consistent with previous results, PI(3,4,5)P3 and p-PKBR1 levels increased and PI(4,5)P2 levels were unchanged, however PI(3,4)P2 levels decreased

(Figure 10F and G). Furthermore, in cells expressing constitutively active Ras mutant, RasCQ62L, which are known to have elevated PI(3,4,5)P3 levels, tPHCynA-KikGR was no longer detectable on the membrane (Figure 10H-J).

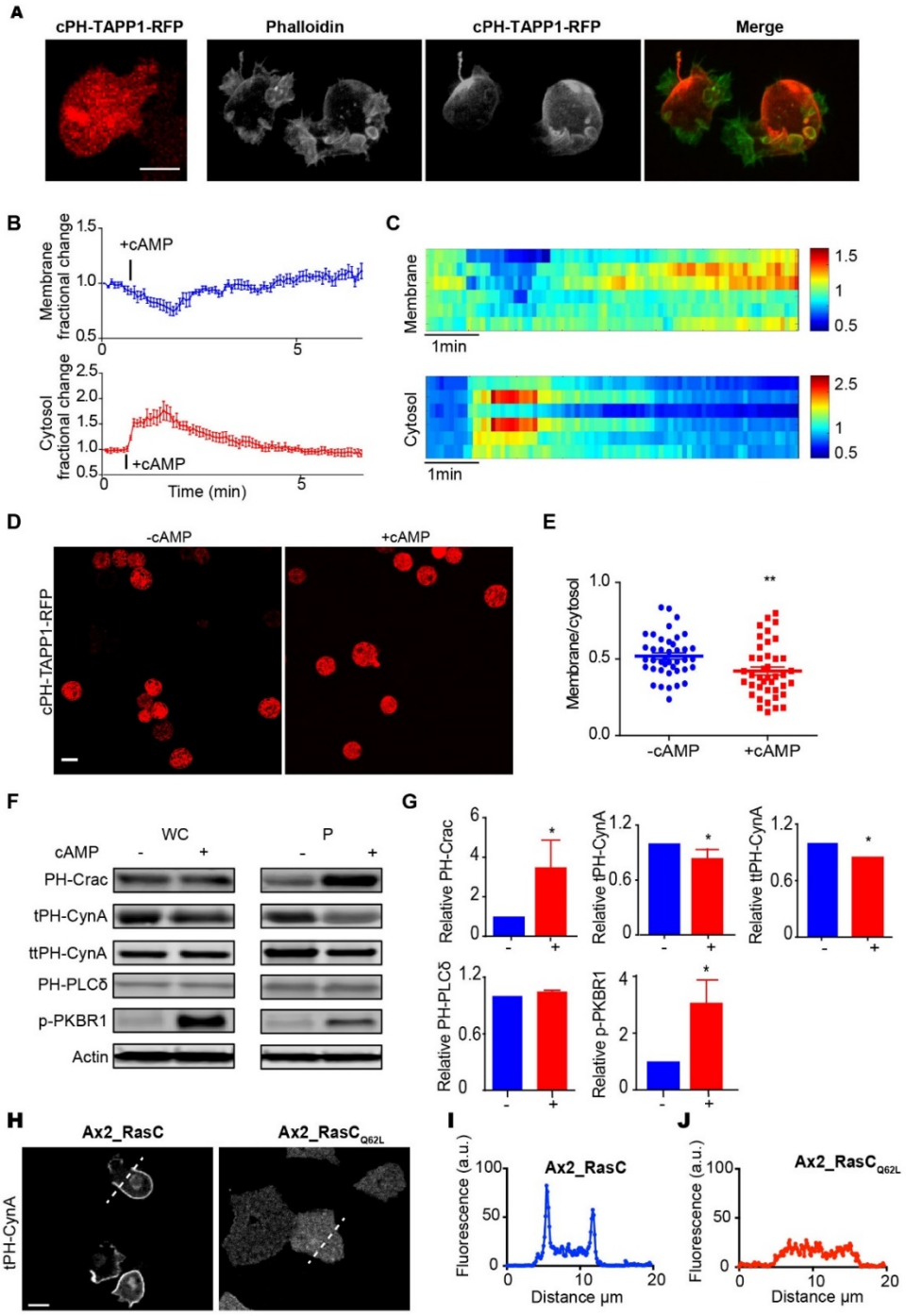

Figure 10. Transient Chemoattractant-Induced Depletion of PI(3,4)P2.
(A) Confocal images showing localization of Phalloidin (green) and cPH$_{TAPP1}$-RFP (red) in fixed cells. Scale bars represent 5 μm.(B and C) 4-hour stage wild-type Ax3 cells expressing tPH$_{CynA}$-GFP were treated with 5 μM

latrunculin A for 20 min and then stimulated with cAMP. Time-lapse confocal images were collected every 5s. Fractional changes of membrane and cytosol intensity of 6 individual cells and corresponding heat maps ordered by magnitude of tPH_{CynA}-GFP decrease were shown. (D) Sets of 4-hour stage wild-type Ax3 cells expressing cPH_{TAPP1}-RFP were treated with 5 μM latrunculin A for 20 min (left), and then taken before or 10s after addition of cAMP. Cells were fixed and imaged. Scale bars represent 10 μm. Data are represented as mean ± S.E.M. (n=41) **P < 0.01 versus –cAMP group. (E) Quantification of the ratio of total minus cytosol to cytosol intensity of cPH_{TAPP1}-RFP. (F) Cells expressing the indicated biosensors were lysed in the absence or presence of 40 μM GTPγS and 10 μM cAMP. After 2 minutes, lysates were diluted 10-fold, and pellets collected by centrifugation. Representative western blots of the PH domain translocation assay with anti-GFP for PH_{Crac}-YFP, tPH_{CynA}-GFP, $ttPH_{CynA}$-GFP, PH_{PLC}-YFP and p-PKBR1 before (-) and after (+) cAMP stimulation in the whole cell (WC) and in the pellet (P) are shown. (G) Quantification of levels of phospholipid in pellet in (F). *P < 0.05 versus –cAMP group. Data are represented as mean ± S.E.M. (n=3). (H) Confocal images showing cPH_{CynA}-GFP in Ax2 cells expressing RasC (left) and constitutively active Ras mutant, $RasC_{Q62L}$ (right). (I and J) A scan across the cell of (H) showing that cPH_{CynA}-KikGR was no longer detectable on the membrane.

When latrunculinA-treated cells were exposed to a gradient of chemoattractant, PI(3,4)P2 levels initially decreased, then within several minutes, showed a continuous accumulation toward the low side of the gradient (Figure 9 I and J). Interestingly, the angle of orientation of the rear-facing crescent of PI(3,4)P2 oscillated with respect to the axis of the micropipette (Figure 9K). Oscillations in the orientation of PI(3,4,5)P3 crescents facing the gradient have been reported (115). Taken together, these observations show that the behavior of PI(3,4)P2 is diametrically opposed to that of front events like PI(3,4,5)P3 generation and Ras activation.

2.3.2 Deletion of OCRL Homologue Dd5P4 Leads to Lowered PI(3,4)P2 and Elevated Ras and Rap Activity

Purified Lowe Oculocerebrorenal Syndrome Protein (OCRL) homologue, Dd5P4, has been shown to generate PI(3,4)P2 from PI(3,4,5)P3 in vitro and we reasoned that deletion of Dd5P4 might lower levels of PI(3,4)P2. Indeed, the membrane to cytosolic ratio of tPHCynA-KikGR was 3.3 ±0.2 in wild-type cells but 1.2 ±0.1 in Dd5P4- cells, suggesting that the PI(3,4)P2 levels are lower (Figure 11A and B).

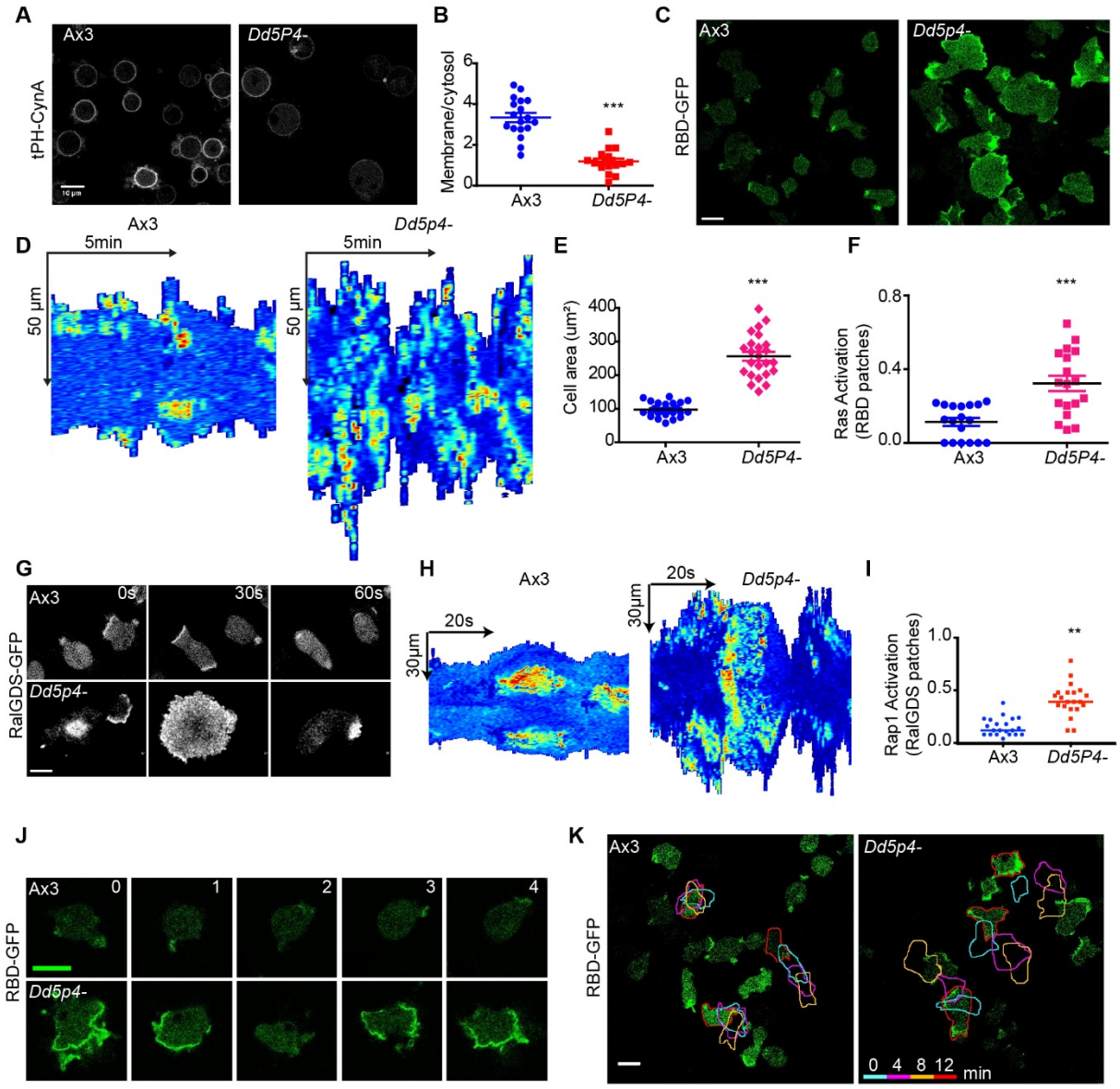

Figure 11. Deletion of OCRL Homologue Dd5P4 Leads to Lowered PI(3,4)P2 and Elevated Ras Activity. (A) Representative confocal images of tPH_{CynA}-KikGR in growth stage, wild-type Ax3 and *Dd5P4-* cells treated with 5 µM latrunculin A. (B) Ratio of membrane to cytosol intensity of tPH_{CynA}-KikGR in wild-type Ax3 and *Dd5P4-* cells; mean±S.E.M (n=18). (C) Representative confocal images of RBD-GFP in migrating growth stage, wild-type Ax3 and *Dd5P4-* cells. Scale bars represent 10 µM. (D) Kymographs of cortical RBD-GFP intensities in representative individual cells from (C). (E and F) Basal surface area (E) and fraction of cell perimeter covered by RBD-GFP patches (F) in cells from (C). *P < 0.05 versus Ax3 group; mean±S.E.M (n=18). (G) Elevated RalGDS activity in *Dd5P4-*cells. Representative confocal images of Ax3 and *Dd5P4-* cells expressing RalGDS-GFP are shown. Scale bar 5 µm.(H) Kymographs of movies of cells in G. (I) Quantification of RalGDS patch activity in Ax3 and *Dd5P4-* cells. Fraction of the perimeter occupied by RalGDS patches was quantified (see methods), n=35. (J) Time-lapse confocal images of individual cells from independent experiment similar to that in (C) highlighting oscillatory *Dd5P4-* cell. Scale bars represent 10 µM. (K). Color-coded tracing of cell outlines at 4 min intervals of several cells from independent experiment similar to that in (C). Scale bars represent 10 µM.

We noted that the Dd5P4- cells were also larger than wild-type cells. Expression of Dd5P4-GFP restored Dd5P4- cell size to wild-type proportions and PI(3,4)P2 to wild-type levels, further demonstrating the important role of this activity (Figures 12A and B).

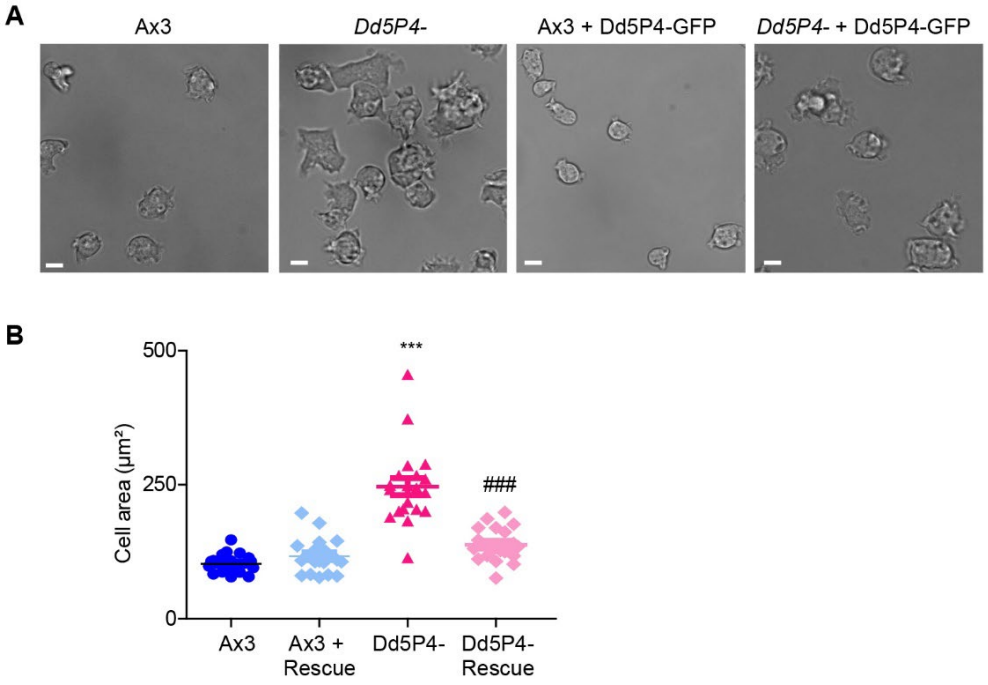

Figure 12. Expression of Dd5P4-GFP restored Dd5P4- cell size.
(A) Phase-contrast images in Ax3 cells, *Dd5P4-* cells, Ax3 cells expressing Dd5P4-GFP, and *Dd5P4-* cells expressing Dd5P4-GFP. Scale bars represent 10 µm. (B) Cell area in different groups in (A). ***P < 0.001 versus Ax3 group; ###P < 0.001 versus *Dd5P4-* group. Data are represented as mean ± S.E.M.

The Dd5P4- cells displayed significantly increased random migratory behavior and enhanced Ras and Rap activity, consistent with the role of these GTPases in regulating protrusive activity (33). Wild-type cells expressing Ras activity sensor, RBD-GFP, showed typical amoeboid profiles with several 1-2 µm-sized pseudopods with elevated activity at the membrane. In contrast, the Dd5P4- cells were dramatically spread with large wide fronts decorated with RBD-GFP (Figure 11C). Kymographs and quantification of the cell perimeter showed that while wild-type cells typically display 1-3 discreet patches of activity, the Dd5P4- cells displayed higher Ras activity which occupied a significant portion of the cell perimeter (Figure 12D). The basal surface area and relative extent of Ras activation in wild-type was 97±4.4 µm2,

and 0.11±0.02, while in Dd5P4- cells they were 256±13 μm2 and 0.32±0.04 (Figure 11E and F). Similar increases of Rap activity were observed using Rap biosensor RalGDS in Dd5P4- cells (Figures 11G-I).

Consistent with these elevated activities, the Dd5P4- cells were often observed to oscillate, displaying a nearly isometric protrusion with high Ras activity, a strong retraction during which Ras activity was extinguished, followed by another global spreading event (Figure 11J). Even though they appeared less polarized, the *Dd5P4-* cells moved apart and scattered more rapidly than wild-type cells, and move much faster than wild-type cells (Figure 11K).

2.3.3 Lowering of PI(3,4)P2 by Exogenous INPP4B Leads to Hyperactive Cell Behavior

We sought to synthetically lower PI(3,4)P2 using 4-phosphatase, INPP4B, to further demonstrate its role in regulation of cell behavior. We expressed a fragment of INPP4B fused to FRB, INPP4B510-924-FRB, in wild-type cells together with a plasma membrane tethered FKBP and various biosensors. Upon rapamycin addition, INPP4B510-924-FRB was recruited to the membrane and tPHCynA-GFP dissociated and moved to the cytosol (Figure 13A). The decrease in PI(3,4)P2 on the membrane occurred gradually and reached its lowest levels within 10 min (Figure 13B and C).

Lowering PI(3,4)P2 led to an increase in cellular spreading and protrusive activity. Figure 13D shows a control cell expressing FRB, and two examples of cells expressing INPP4B510-924-FRB. FRB recruitment had little effect, while bringing INPP4B510-924-FRB to the membrane led to a substantial increase in area, perimeter and protrusive activity (Figure 13D and E). Many cells intermittently displayed oscillations, undergoing periods of spreading and retraction, upon recruitment of INPP4B510-924-FRB (Figure 13G).

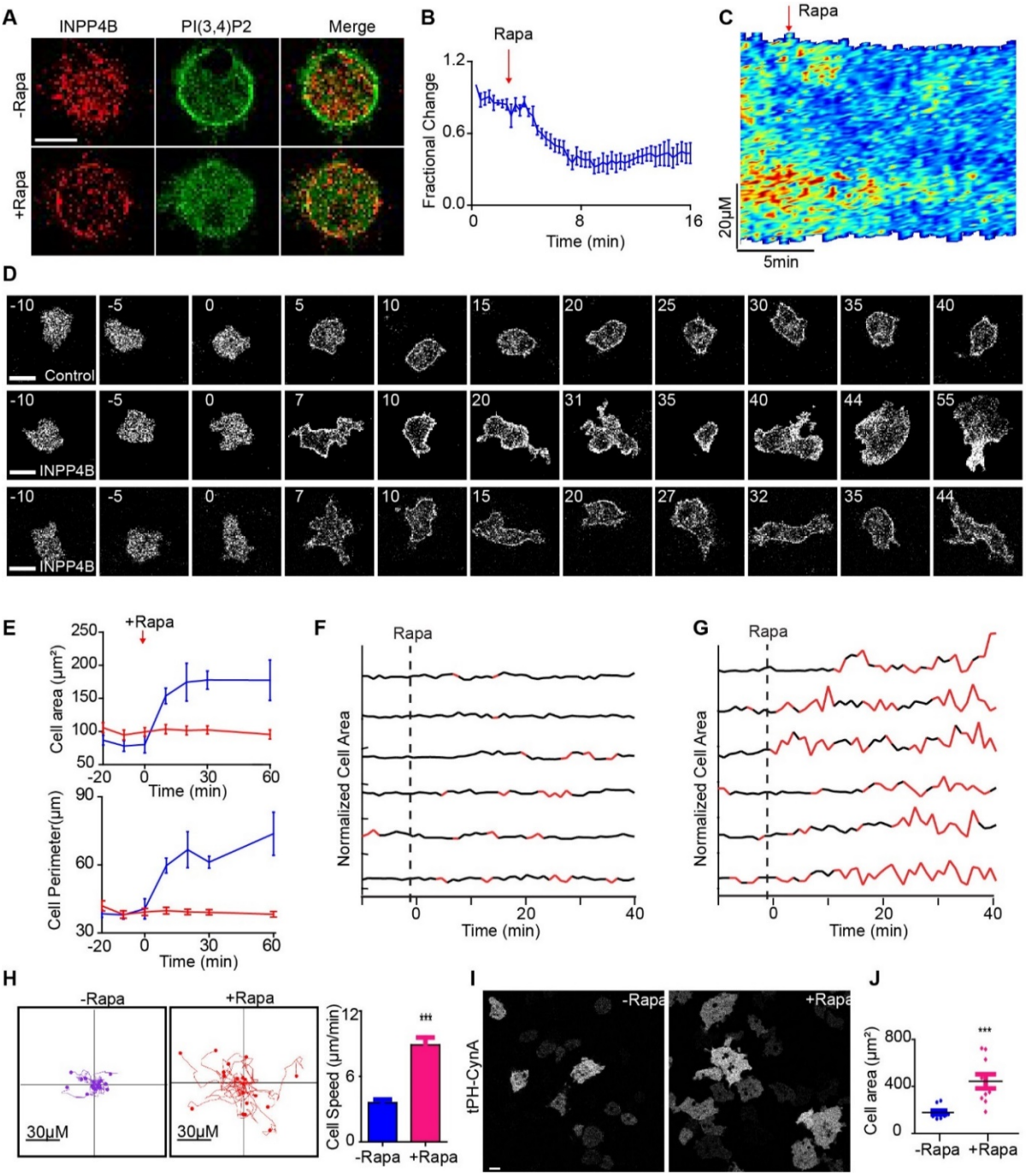

Figure 13. Lowering of PI(3,4)P2 by Exogenous INPP4B Leads to Hyperactive Cell Behavior.
(A) Growth-stage, wild-type Ax3 cells expressing mCherry-FRB-INPP4B$_{510-924}$ (red), N150-tFKBP and tPH$_{CynA}$-GFP (green) were treated with 5 μM latrunculin A for 20 min. The time-lapse confocal images of the same cell were obtained every 20 s for 1 h. Representative images before (top) and 30 min after rapamycin (Rapa) treatment (bottom) are shown. Scale bars represent 10 μM. (B) Fractional changes of ratio of membrane to cytosol intensity of tPH$_{CynA}$-GFP in experiment in (A). (n=5). (C) Kymograph of cortical tPH$_{CynA}$-GFP membrane intensity of representative cell from (A). (D) Randomly migrating growth-stage, cells were imaged every 20 sec. Confocal images of three individual cells showing the transition of the cell migratory modes before and after rapamycin treatment. Wild-type Ax3 cells expressing mCherry-FRB-INPP4B$_{510-924}$ (red) and N150-tFKBP in the second and third rows. Control cells in the first row are expressing mCherry-FRB (red) instead of mCherry-FRB-INPP4B$_{510-924}$. Scale bars represent 10 μM. (E) Cell areas and cell perimeters were quantified before and after addition of rapamycin for control (red) and experimental cells (blue) in an

independent experiment similar to that in (D). (n=12). (F and G) Normalized areas of 6 control (F) and 6 experimental cells (G) at 1 min intervals. Rapamycin was added at t=0. Cells were segmented into amoeboid or oscillatory migratory modes, black and red respectively using MATLAB. (H) Centroid tracks showing random movement of cells from (D) before and after rapamycin addition. Each track lasts 10 min and was repositioned to the same origin. Quantification of the cell speed is on the right. (n=18). (I) Time-lapse confocal images of *Dd5P4-* cells expressing mCherry-FRB-INPP4B$_{510-924}$ and N150-tFKBP before (left) and 30 min after (right) rapamycin treatment. Scale bars represent 10 μm. (J) Basal surface area covered by tPH$_{CynA}$-GFP in cells from (I). ***P < 0.001 versus AX3 group; mean±S.E.M (n=10).

In contrast, control cells with recruitment of FRB showed only infrequent gentle oscillations (Figure 13F). The highly active cells with recruited INPP4B510-924-FRB displayed greater random motility. The average speed increased from 3.6 ± 1.2 μm/min to 8.9 ± 2.9 μm/min (Figure 13H).

We combined the two independent perturbations of lowering PI(3,4)P2 by expressing INPP4B510-924-FRB in the Dd5P4- cells. As shown in Figure 13I and J, the cells became extremely spread on the surface with larger basal area, suggesting that the effects of the two perturbations were additive. Recruitment of INPP4B510-924-FRB is not expected to increase PI(3,4,5)P3 levels as likely occurs in *Dd5P4-* cells. This suggests that the increase of cell spreading and enhanced random motility in these cells is primarily due to lowered PI(3,4)P2.

2.3.4 The contribution of PI(3,4,5)P3 to Ras activity

We further dissected the relative contributions of PI(3,4,5)P3 to PI(3,4)P2 levels and Ras activity by inhibiting PI3K. The sensitivity of the elevated Ras activity in wild-type and Dd5P4- cells to PI3K inhibition was time dependent. Wild-type cells treated with LY294002 immediately round up with few RBD patches; after about 30-45 min the RBD patches largely return, and the cells resume random motility (116) (Figure 14A and B). Surprisingly, PI(3,4,5)P3 depletion led to dramatically increased PI(3,4)P2 levels as the cells rounded up. The Dd5P4- cells are more resistant to LY294002 treatment, remaining more active than wild-type cells.

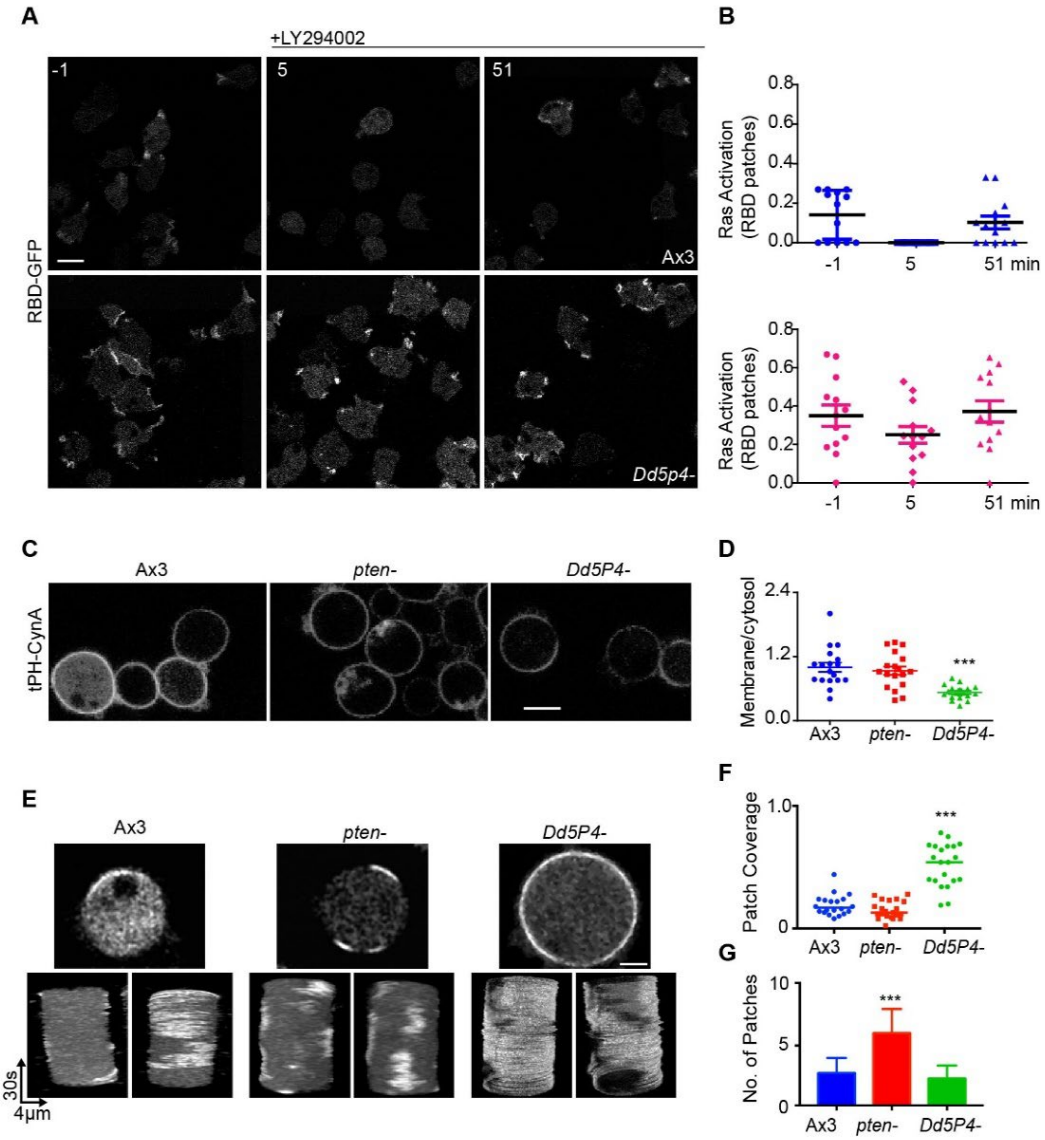

Figure 14. The contribution of PI(3,4,5)P3 to Ras activity.
(A) Confocal representative images of vegetative, wild-type Ax3 (top row) and *Dd5P4-* cells (bottom row) expressing RBD-GFP treated with 50 µM LY294002 for -1(left), 5 (middle) and 51 min (right). Scale bars represent 10 µM. (B) Quantification of fraction of cell perimeter covered by RBD-GFP patches in (A). (C) Representative confocal images of tPH_{CynA}-GFP in growth stage wild-type Ax3, *Pten-* and *Dd5P4-* cells treated with 5 µM latrunculin A. (D) Ratio of membrane to cytosol intensity of tPH_{CynA}. mean±S.E.M (n=18).(E) RBD patch dynamics in Latrunculin A treated cells. Representative images from time-lapse movies of Latrunculin A treated cells expressing RBD-GFP are shown above 180° rotated views of t-stacks generated from 4 min time-lapses. (F) Quantification of the fraction of the perimeter from cells in (E), occupied by RBD patches. (n=18). *** p<.005. (G) Quantification of the number of RBD patches generated during four minute time-lapse movies of cells in (E) Error bars standard deviation (n=18). *** p<.005.

The broad bands of RBD along the cell perimeter were broken into 2-3 smaller patches but after about 25-40 min the cells recovered to the original phenotype (Figure 14A). Also, in Dd5P4- cells, the increase in PI(3,4)P2 upon PI(3,4,5)P3 depletion was blunted.

Next we examined PI(3,4)P2 levels and Ras activities in pten- cells which have elevated PIP3 levels, and compared them with those in the Dd5P4- cells. In latrunculin A treated cells, the relative PI(3,4)P2 levels were 1, 0.94 and 0.53 in wild-type, pten- and Dd5P4- cells respectively (Figure 14C and D); Ras activity is confined to 0-2 patches in Ax3 cells, whereas in Dd5P4- cells the patches occupied almost the entire cell perimeter. In pten- cells the patches of Ras activity were smaller than those in wild-type cells, however, there were many more patches over time (Figure 14E-G). Taken together, these observations suggest that the elevated Ras activity in Dd5P4- cells is largely dependent on decreased PI(3,4)P2. Nevertheless, there is a contribution of feedback from PI(3,4,5)P3.

2.3.5 RasGAP2 and RapGAP3 Bind to and are Regulated by PI(3,4)P2

In order to further explore the activation of Ras and Rap coinciding with the decreases in PI(3,4)P2, we examined the behavior of RasGAP family member, RasGAP2 (RG2), and RapGAP family member, RapGAP3 (RG3) (117). The position of these proteins in the family hierarchies and domain structures are shown in Figures 15A and B. We first noticed that these proteins localized to cup-shaped protrusions at the leading edge of the cell but were displaced to the base of the structures away from F-actin biosensor LimE (Figure 15C and D). In addition, RG2 and RG3 associated strongly with the rear of the cell, away from the sites of protrusion. Careful examination of the kinetics of the formation of the cup-shaped protrusions showed that RG2 and RG3 appeared late in the lifetime of these structures as the levels of LimE were waning (Figure 15E-H). Although the lifetime of different protrusions varied, we were able to

compile the kinetic behavior of LimE versus RG2 or RG3 by dividing the total duration of each protrusion into 10 time segments (Figure 15F and H).

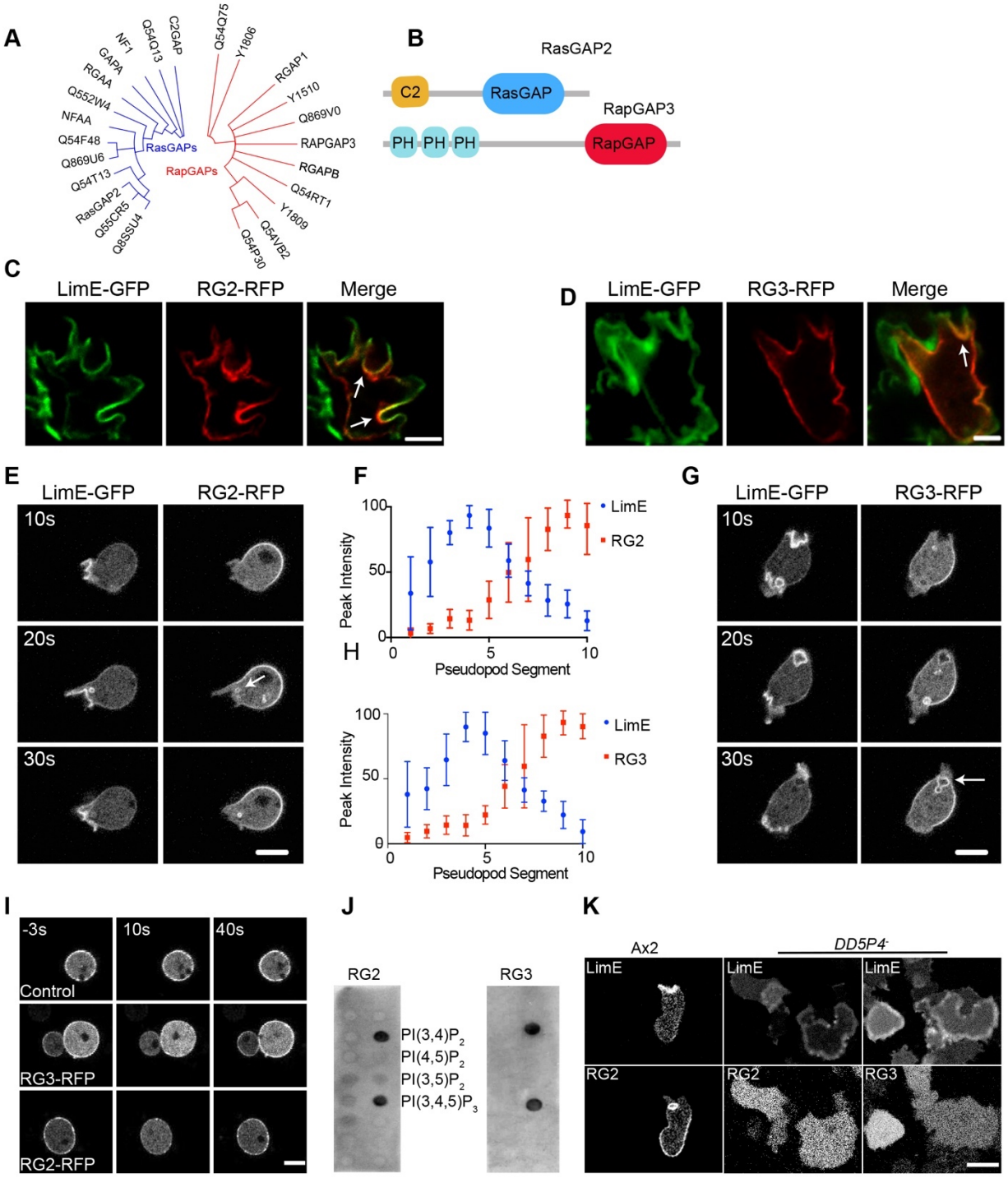

Figure 15. RasGAP2 and RapGAP3 Bind to and are Regulated by PI(3,4)P2.

(A) Unrooted phylogenetic trees of *Dictyostelium* genes with consensus RasGAP and RapGAP domains. Uniprot IDs are listed for uncharacterized genes. (B) Domain organization of RasGAP2 (RG2), accession number DDB_G0278483, and RapGAP3 (RG3), accession number DDB_G0271806. (C and D) Single confocal sections of cells co-expressing RFP tagged RG2 (C) or RG3 (D) with LimE-GFP. Arrows point to the localization of GAP proteins to the base of cup-shaped macropinosome crowns. (E) Selected frames from time-lapse movies of RG2-RFP and GFP-LimE co-expressing cells. Arrows point to the accumulation of RG2 at the base of macropinocytotic crowns and nascent macropinosomes. (F) Analysis of RG3 localization as in (E). (G) Selected frames from time-lapse movies of RG3-RFP and GFP-LimE co-expressing cells. Arrows point to the accumulation of RG3 at the base of macropinocytotic crowns and nascent macropinosomes. (H) Analysis of RG3 localization as in (G). (I) 4-hour stage Ax2 cells expressing RG3-RFP were treated with 5μm Latrunculin A for 10 minutes prior to beginning the time course. cAMP was added at time zero. (J) Binding of RG2-GFP and RG3-GFP to the indicated lipids immobilized on "PIP strips" see methods. (K) Confocal representative images of Ax3 and Dd5P4 null cells co-expressing LimE and one of RG2-GFP, or RG3-GFP.

Further evidence suggested that RG2 and RG3 behave kinetically like PI(3,4)P2 biosensors and in fact bind to PI(3,4)P2. In latrunculin A treated cells, RG2 and RG3 distributed uniformly around the cell perimeter. Within 10 seconds of addition of chemoattractant, RG2 and RG3 dissociated from the membrane, moved to the cytosol, and then returned to the membrane by 40 s (Figure 15I). Controls showed that the response was specific for chemoattractant. On PIP-strips, both RG2 and RG3 bound to PI(3,4)P2 and PI(3,4,5)P3 (Figure 15J).

To further demonstrate the role of PI(3,4)P2 in regulating RG2 and RG3, we investigated the distribution of these proteins in Dd5P4- cells, which have low levels of PI(3,4)P2 (Figure 11A and B). While F-actin activity was excessively elevated in the form of rapidly propagating actin waves in Dd5P4- cells, RG2 and RG3, were absent from the membrane (Figure 15K). Taken together these results suggest that RG2 and RG3 bind to PI(3,4)P2 and are regulated by the dynamic distributions of this phosphoinositide.

2.3.6 Deletion of RasGAP2 and RapGAP3 Leads to Ras and Rap Activation and the Hyperactive Phenotype

We next examined the changes in wave behavior that accompanied the transitions to different RG2 and RG3 suppressed Ras and Rap activity and controlled protrusion size and number.

Deletion of RG2 led to significantly elevated Ras activity. In wild-type cells, activity patches are confined to about 1 µm, while in RG2- cells, they nearly covered the cell perimeter (Figure 16A). Similarly, in RG3- cells, patches of Rap activity and protrusions were also elevated (Figure 16B). In latrunculin A treated RG2- and RG3- cells, the respective patches occupied more than half of the cell perimeter, whereas in wild-type cells, they occupied less than 20%. Kymographs of latrunculin A treated cells further demonstrated the dramatic change in the amount of active Ras and Rap in RG2- and RG3- cells, respectively (Figure 16C-F). These elevated activities led to increases in random motility. Tracks of individual cells demonstrated that the RG2- and RG3- cells moved further from starting points compared to the wild-type cells. The average speed of wild-type cells was 5± 0.25 µm/min, while those of the RG2- and the RG3- cells were 8± 0.34 µm/min and 8 ± 0.3 µm/min respectively (Figure 16G and H). These results implicate RG2 and RG3 as important regulators of protrusion dynamics and motility.

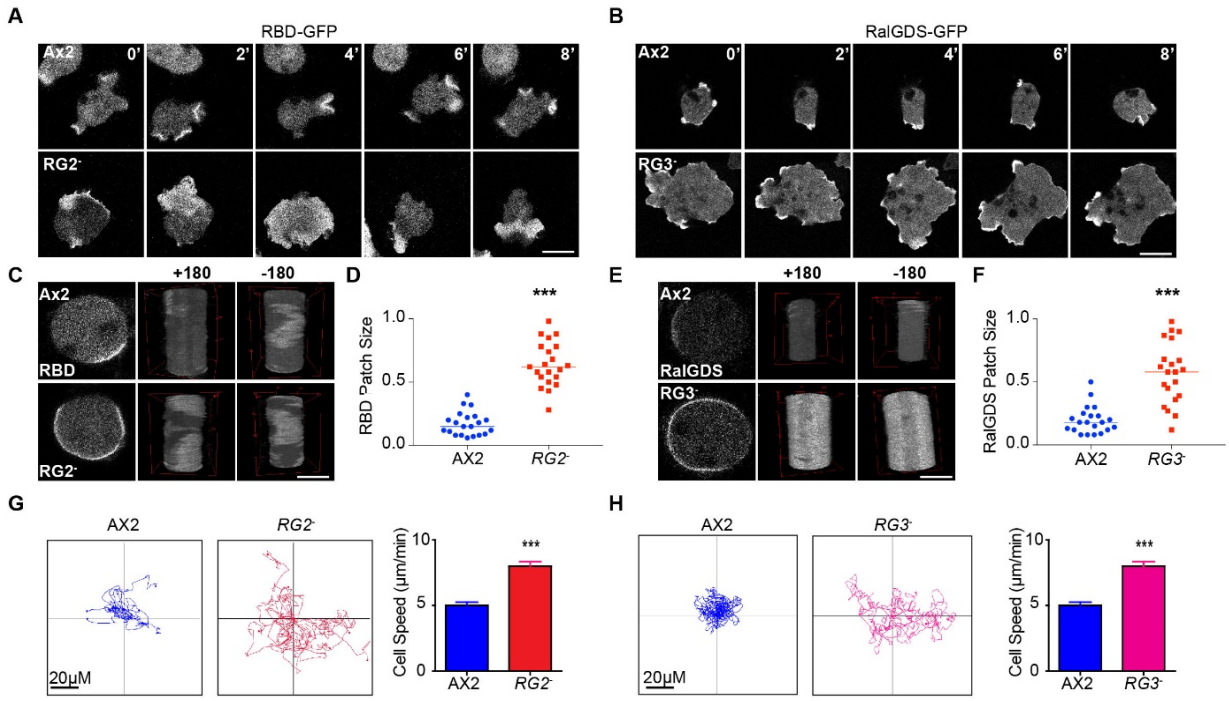

Figure 16. Deletion of RasGAP2 and RapGAP3 Leads to Ras and Rap Activation and the Hyperactive Phenotype.

(A) Ras patch dynamics in wild-type and RG2-cells. Selected frames from time lapse movies of Raf1-RBD-GFP expressing wild-type and RG2- cells. (B) Similar experiments as in A showing Rap1 (of RalGDS-GFP) patch dynamics in RG3- cells. (C) Comparison of Ras patch dynamics in latrunculin A treated cells. Frames from time lapse movies were stacked vertically to create –time stacked kymographs which are shown in two 180degree rotated views. (D) Quantification of the portion of the cell perimeter from C encompassed by RBD patches. *** p<.001. (E) Similar experiments as in C illustrating Rap1 patch dynamics using RalGDS-GFP biosensor. (F) Experiments in E were quantified as in D. Scale bar 7µm. *** p<.001. (G and H) Rose plots of cell tracking data from time lapse movies of RG2- and RG3- cells. Quantification of the cell speed is on the right respectively.

2.3.7 Deletion of Dd5P4 Allows Axenic Growth in The Presence of NF-1

Elevated Ras activity is associated with increased macropinocytosis and previous studies have shown that mutations that confer axenic growth to *Dictyostelium* cells map to the RasGAP, neurofibromin homolog, NF-1. Since Dd5P4-, RG2- and RG3- cells have more protrusive activity than wild-type axenic cells, we tested the extent to which NF-1 expression would prevent their growth in axenic media. The growth of wild-type, RG2- and RG3- cells was largely inhibited. However, Dd5P4- cells expressing NF-1 were able to grow, albeit slowly, in axenic media (Figure 17A and B). Consistently, pinocytosis was elevated in NF-1 expressing Dd5p4- cells (Figure 17C). These results show that significant lowering PI(3,4)P2 elevates Ras activity sufficiently to allow cells to grow under axenic conditions.

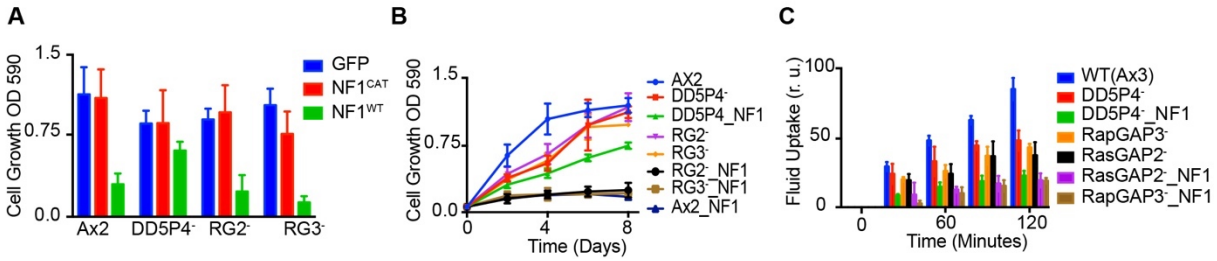

Figure 17. Ax3 carries a loss of function mutation at the NF-1 locus which confers axenic growth.
Expressing NF-1-WT in these and Ax3 derived RG2- and RG3- cells leads to cell death under axenic growth conditions.
(A) Cells expressing, GFP (vector control) NF-1 WT or an NF-1 'arginine finger' mutant were removed from bacterial co-culture and grown under axenic conditions for two days before cell growth was scored (see methods). (B) Cell growth time course over 8 days as in A. Error bars standard error. (C) Pinocytosis assays using fluorescent dextran. Error bars standard error.

2.3.8 Simulation of Cell Behavior Based on Mutually Inhibitory Positive Feedback Loop

The mutual inhibition between Ras activity and PI(3,4)P2 described here would be expected to comprise a positive feedback loop, providing a molecular basis for the excitable network hypothesis. Previous implementations of these models employed an activator which positively regulates itself, and a delayed inhibitor which returns the system to basal. Here we introduce three states: F, B and R, in which mutual inhibition between F (reflected by Ras activity), and B (reflected by PI(3,4)P2) constitutes the positive feedback loop, and R serves as the delayed inhibitor (Figure 18A and B). Computational analysis showed that during activation, F rises rapidly as B falls. These events are followed by a delayed rise of R, which returns the system toward its basal state. There is an undershoot in F and an overshoot in B before they return to the basal state (arrows), which is generated by the transient excess in R over F (Figure 18B). When F, B and R are allowed to diffuse, spontaneously triggered waves of F and R propagated laterally as in previous models. Correspondingly, regions devoid of B create shadow waves in the F enriched zones (Figure 18C).

We used a 1D model of this modified excitable system coupled to a viscoelastic cell model in the level set framework to determine the distribution of F, B, and R states on the protrusive structures which drive migration. In the absence of a protrusion, the membrane is in the B state. As noise triggers a protrusion, there is a local decline in B state, and a corresponding rise in F state. These activities propagate outwardly generating a cup-like protrusion. At the base of the cup-like protrusion, B state activity transiently rises above its basal level, corresponding to the overshoot of B (Figure 18D and E). These simulations are consistent with our observations of the distributions of front and back markers along the membrane and at the cup-shape

protrusions (Figure 18F, 5C and D). As expected, R state activity trails the outwardly propagating F state (Figure 18D and E).

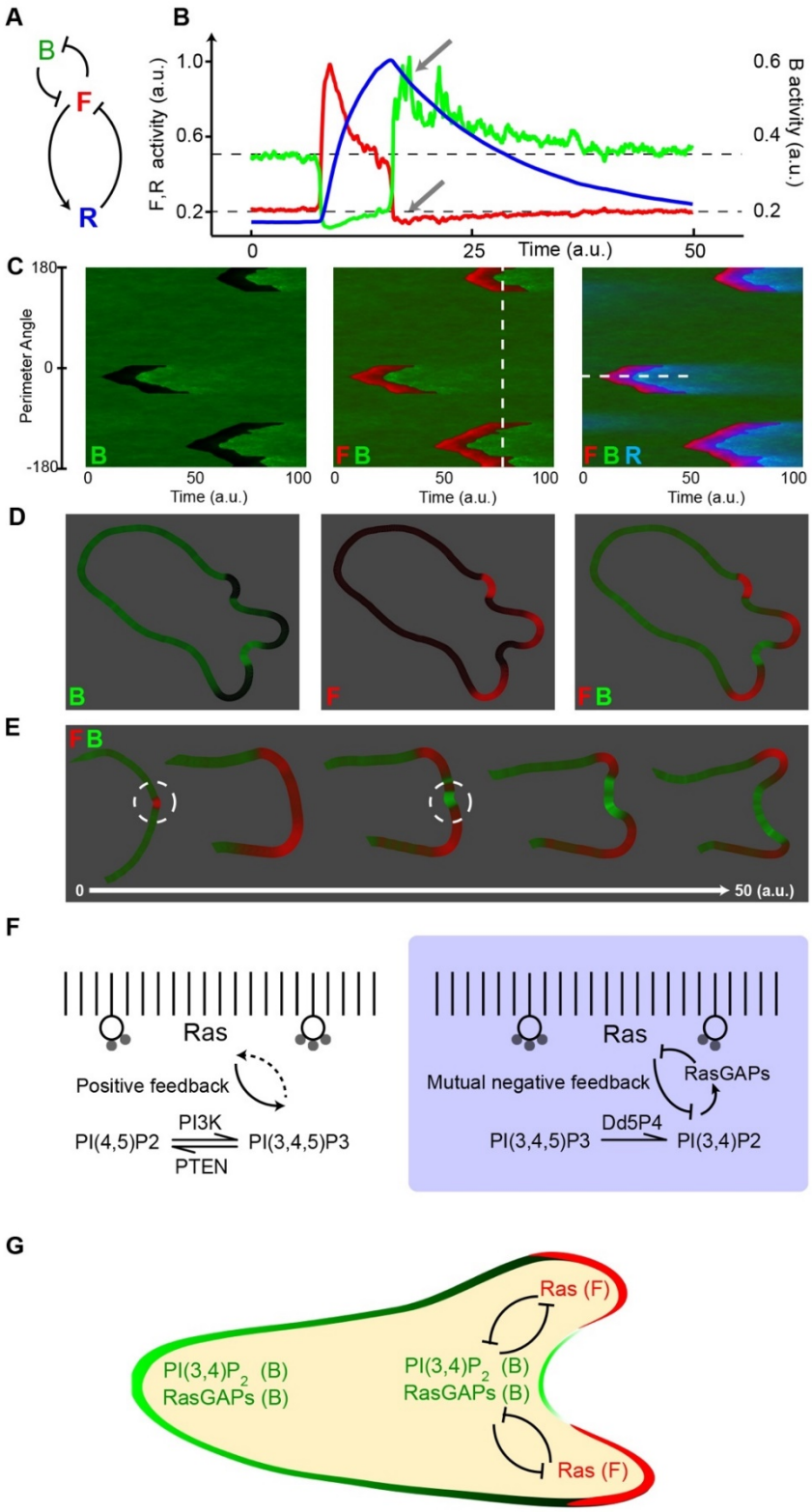

Figure 18. Simulation of Cell Behavior Based on Mutually Inhibitory Positive Feedback Loop.

(A) Three state model of excitability. Front (F) in red, Back (B) in green, and Refractory (R) in blue are connected by positive (arrows) and delayed negative (bars) feedback loops. (B) Typical responses of the F, B and R states when the system is triggered. Arrows emphasize the undershoot and overshoot in F and B respectively. (C) Simulated kymographs generated using a one-dimensional discretized domain resembling the cell perimeter. Left, shadow wave activity of B, with the dark regions denoting the lowest levels and bright green the overshoot; middle, F and B activity; right, all three states. The horizontal dashed white line corresponds to the time-course shown in (B). (D) Level set simulations modeling the protrusion forces corresponding to the dashed line in the center panel of (C). (E) Close up of the the time course, left to right, of a single protrusion from (D). (F) Left, Ras regulation of PI(3,4,5)P3 production showing positive feedback. Right, molecular architecture of the mutually Inhibitory Ras-RasGAPs-PI(3,4)P2 feedback loop. (G) Schematic representation of the opposing spatial and temporal patterns of Ras activity and PI(3,4)P2 in migrating cells.

2.4 Discussion

Our results reveal a mutual inhibitory interaction between Ras activation and PI(3,4)P2 that is central for cell migration. We show that chemoattractants, which activate Ras, as well as expression of RasCQ62L, lead to a reduction of PI(3,4)P2. Since RG2 binds to PI(3,4)P2, its dissociation from the membrane leads to a further increase in Ras activity, which in turn further decreases PI(3,4)P2, creating a powerful positive feedback loop (Figure 18F and G). There is a similar loop involving RG3. Rap1 has been reported to lie upstream of RasC (33), but the regulation of both GAPs by PI(3,4)P2 suggests there are separate, interconnected loops. This model is consistent with our observations of the patterns of Ras and Rap activities and PI(3,4)P2 in migrating cells and the phenotypes resulting from perturbations. Moreover, the discovery of these positive feedback loops provides critical insight to molecular mechanisms of excitability.

The Role of PI(3,4)P2 in Cell Migration

The localization of PI(3,4)P2 at the back of the cell as well as at protrusions at the leading edge of the migrating cells can be explained by our model (71, 74, 118-120). High resolution time-resolved observation of protrusions at the leading edge revealed that PI(3,4)P2 is actually depleted during the early stage of a protrusion but then becomes enriched late in the cycle as PI(3,4)P2 rebounds onto the membrane during retraction at the central region of the protrusion. Thus, back proteins can transiently localize to the front at the base of the protrusions. The fact that the TAPP1 biosensor underrepresents PI(3,4)P2 at the back likely explains why most previous investigators have reported that PI(3,4)P2 is exclusively a leading edge component.

Gene deletions that modify PI(3,4)P2 levels have been previously reported to create migratory and growth phenotypes in mammalian cells. SHIP1 null granulocytes have been reported to

show increased responses to cytokines and chronic progressive hyperplasia (121). The hyperactive phenotypes in SHIP1 gene deletions have been attributed to elevated PI(3,4,5)P3 levels present in these cells (122). However, our results raise the possibility that these phenotypes are due to lowered PI(3,4)P2 rather than elevated PI(3,4,5)P3 levels. PI3K inhibition only partially reduced the hyperactivity of Dd5P4- cells, strongly suggesting that the lowered PI(3,4)P2 leading to high Ras activity, is the major mediator of this phenotype (Figure 13, and 18F). Our observations that inhibition of PI3K partially reduced Ras activity and elevated PI(3,4)P2, while loss of Pten increased Ras activity, are consistent with the existence of a PI(3,4,5)P3-Ras feedback loop (59).

Other RasGAPs including NFaA, NF-1 and C2GAP have also been implicated in the regulation of Ras activity in *Dictyostelium*. The reported loss of functions of these phenotypes (123-125) are consistent with our observations of RG2- and RG3- cells. Remarkably, this suggests that each of these five GAPs independently contribute to the regulation of Ras or Rap activities. Going forward, it will be important to determine whether NFaA, NF-1 and C2GAP are also regulated by PI(3,4)P2 as are RG2 and RG3. Only deletion of NF-1 confers the ability to grow in axenic media, suggesting that it might be the major regulator of macropinocytosis (123). Interestingly, deletion of Dd5P4 did allow cells to grow in axenic media, indicating that depleting PI(3,4)P2 might produce a level of Ras activation similar to the loss of NF-1. However, the exact relationship between Ras activity and axenic growth remains to be determined

PI(3,4)P2, Excitable Networks, and Cellular Protrusions

There appears to be a consistent pattern of phospholipid regulation involved in cup-like protrusions in migrating cells and in various internalization events. The PI(3,4)P2 found in the central region of an expanding protrusion persists at that zone and is internalized on

macropinosomes (126). It has been previously reported that PI(3,4)P2 decorates phagocytic cups and internalized phagosomes (127). This suggests that as we found here for macropinocytosis, PI(3,4)P2 may also act as a negative regulator during phagocytosis. PI(3,4)P2 is associated with the late stage of endosomes, indicating similarity to phagosomes and macropinosomes (71, 79). It will be interesting to determine whether PI(3,4)P2 binding proteins also negatively regulate all of these events.

The regulation of the localization of PI(3,4)P2 interacting GAPs RG2 and RG3, is also consistent with the observed elevation of Ras and Rap activity at the initiation and edges of an expanding protrusion and its rapid decline in the central, older region of the cup-shaped protrusions (128). Furthermore, the back to front gradient, which we observed with all the PI(3,4)P2 biosensors, is largely derived from the depletion of PI(3,4)P2 at the protrusions at the leading edge, while PI(3,4)P2 production at the back might also play a role.

The excitable network hypothesis which comprises positive and delayed negative loops between hypothetical F and Rstates has been remarkably successful in accounting for wave propagation and the spectrum of behaviors of migrating cells. The Ras-PI(3,4)P2 feedback loop we identified, provides significant insights into the molecular mechanism of excitability. Our findings suggest that in addition to F and R states, a separate B state is characterized by high PI(3,4)P2 and low Ras activity, whereas the F state is characterized by low PI(3,4)P2 and high Ras activity. The switch between the states is controlled in part by the reversible recruitment of PI(3,4)P2-binding RasGAPs, and as yet uncharacterized regulation of the enzymes that control PI(3,4)P2. The excitable network model is therefore consistent with the observed localization of B state associated proteins along the membrane and at the base of protrusions at the leading edge of the cell.

The interaction between Ras and PI(3,4)P2 that we identified here provides the most complete description of a feedback loop that mediates cell migration and raises interesting questions for further research. First, what are the key enzymes, in addition to Dd5P4, which control PI(3,4)P2 levels and how are all of these enzymes regulated by Ras? How is this regulation achieved in the presence and absence of PI(3,4,5)P3? Second, what is the mechanism by which the GAPs, RG2 and RG3, bind to PI(3,4)P2? What are the key domains in these proteins that mediate the binding? Do other Ras Gaps, such as NF-1 and C2Gap, also bind to PI(3,4)P2 and are they coordinately regulated with RG2 and RG3? Finally, how are the various Ras regulatory loops, which have been previously suggested, synchronized with the Ras-PI(3,4)P2 positive feedback loop delineated here?

2.5 Methods

Cell Culture and differentiation

Wild-type *Dictyostelium discoideum* cells of the AX3 strain, which is an established lab cell line because of its ability to form fruiting bodies upon starvation and its morphology and behavior during chemotactic assays, were used in this study. All cells were grown at 22 °C axenically in HL5 media on tissue culture dishes for cell line maintenance or in suspension to obtain high cell densities in preparation for cell differentiation. Cells expressing LimEΔcoil-RFP, PH_{CRAC}-RFP, PH_{TAPP1}-GFP, PH_{PLC}-YFP, RBD-GFP, RalGDS-GFP, $INPP4B_{510-924}$-FRB, RG2-GFP, RG3-GFP, or various CynA constructs were generated by electroporation of the appropriate plasmids. Cells were selected and maintained in HL5 media containing 20 μg/mL G418, 50 μg/mL Hygromycin B, or both. To induce differentiation, cells were washed twice in development buffer (DB: 5 mM Na_2HPO_4, 5 mM KH_2PO_4, 2 mM $MgSO_4$, and 0.2 mM $CaCl_2$) and then starved in suspension in DB at 2 × 107 cells/mL for 1 h. Cells were then pulsed with 50 nM cAMP every 6 min for 4–6 h. Differentiation and imaging experiments were conducted at room temperature. Cells were used within 2 months of thawing from frozen stocks. For experiments using pharmacological inhibitors, Latrunculin A or LY294002 were diluted in DB from stock solution in dimethylsulfoxide (DMSO). For microscopy, cells were plated in DB buffer to reduce the auto fluorescence associated with HL5 and the photosensitivity of growing cells, which allowed for prolonged and frequent imaging.

Plasmid Construction

To make membrane-anchored FKBP constructs, sequences encoding the first 150 amino acids at the N terminus of PKBR1, and tandem FKBPs were linked and cloned into pCV5. Sequences encoding mCherry, FRB, and 510-924 amino acids of INPP4B were linked and cloned into pCV5. The linker sequence between mCherry and FRB is 5′-GGAGCAAGTGGA-3′and two

repeats of 5′-AGTGCTGGTGGT-3′ were used between FRB and $INPP4B_{510-924}$. cPH_{TAPP1} and tPH-CynA-KikGR were cloned into KF2 (10). Dd5P4-GFP construct was gift from Peter J M Van Haastert, University of Groningen, Groningen. LimE -RFP, PH_{CRAC}-RFP and PH_{PLC}-YFP and various of CynA-GFP plasmids were created in previous studies. RG3-GFP constructs were a gift from Dr. Taeck Jeon Chosun University. RasGAP2, RG2, was cloned from genomic DNA using primers Fwd GCTCGAG ACAATAC CGTTTGGAAAAGTAGTAAT AAAAATTTTA GGAG CA AGGG and Rev TTATTTTTTT GATTTT TCAATTA ATATCTTTGGTTCTTG into expression vector KF2. A combination of biosensor (pCV5), mCherry-FRB-$INPP4B_{510-924}$ (pCV5), and myr-FKBP-FKBP (pCV5) was used, and the cells were cultured with G418 (20 μg/ML).

Deletion strains

Dd5P4- cells were from DictyBase. The *Dd5P4-* strain was previously created and reported. The new *RG2-* and *RG3-* strains were created by replacing the ORF region + 951936 to +954731 with a Blasticidin S resistance (BSR) cassette. The deletion construct was created by amplifying the 5' and 3' end for homologous recombination using Primers 5' Fwd; GACAATACCGTAATTTG GA AAAGTAGTAATAAAAATTTTAGG 5'Rev;GAGGCGACAAACACACC AGCGTCGC ATAAAATTAC and 3'Fwd; CTCA AC AAA AACAAGAAC CAAAGATATTAATTG 3' Rev; CCAACAGGAATCGAACC TGTTATT CAGC TT TG AATGTTGGG respectively. These PCR products were cloned using the pLPBLP plasmid. The final cassette was amplified and transformed into the AX2 strain. Clonal isolates were selected on a K. aerogenes lawn. The single clones were screened for appropriate genes disruption by PCR and southern blotting.

Microscopy

Growth-phase cells were placed in an eight-well coverslip chamber (Lab-Tek, Thermo Scientific, Nunc) and allowed to adhere for 5-20 min before imaging. Cells were incubated with latrunculin A (5 mM stock solution in DMSO) in DB for 10-30 min before imaging started. 5 μM rapamycin (553210, Calbiochem) or 50 μM LY294002 (50 mM stock solution in DMSO) was used and added into the chamber during live cell imaging. Confocal imaging was performed using a Zeiss LSM780 single-point laser-scanning microscope (Zeiss AxioObserver with 780-Quasar confocal module; 34-channel spectral, high-sensitivity gallium-arsenide phosphide detectors, GaAsP). Time-lapse images were acquired with DIC, GFP, and RFP (where applicable) illumination at 3- to 25-s intervals for 20-180 min. Images are quantified using MATLAB to isolate signal on the membrane to convert to time kymographs. Phase image acquisition and micropipette assay were performed using phase illumination on a Zeiss Observer.Z1 inverted microscope (Axiovision software) equipped with a 40 X oil objective.

Phosphoinositide assays

As previously described (1) cells expressing PH_{CRAC}-YFP, cPH_{TAPP1}-GFP, PH_{PLC}-YFP, RG2-GFP, RG3-GFP, multi-PIP control or various CynA-GFP constructs were washed, resuspended and starved in DB at 2×10^7 cells/mL for 3 h. Then cells were washed twice, and resuspended in cold 10 mM sodium phosphate buffer (pH 7.2) with protease inhibitor (complete tablets, Roche). Samples were filter lysed and were centrifuged for 10 min at 10,000 × g at 4 °C. The supernatant was collected and added to an equal volume of 2× Binding Buffer [300 mM NaCl, 10 mM sodium phosphate buffer, 0.5% Nonidet P-40] and incubated with the previously blocked PIP Strips (P-6001, PIP Strips, Echelon) at 4 °C for 3 h. Samples of the supernatant before and after incubation with PIP Strips, were collected for immunoblotting. PIP strips were washed three times with PBST and then incubated with anti-GFP primary antibody (mouse, monoclonal; Roche) overnight at 4 °C. The next day the PIP strips were washed with PBST,

incubated with an HRP conjugated anti-mouse secondary antibody (GE Healthcare). The signal was then detected by chemiluminescence imager. MultiPIP Grip (G-9901, PIP Strips, echelon) was performed as a positive control, which contains lyophilized, recombinant GST-tagged LL5α-PH domain protein which has affinity for all phosphoinositide polyphosphates.

Single-molecule binding assay

Lipid vesicles were prepared by probe sonication with 1,1'-dioctadecyl-3,3,3',3'-tetramethylindodicarbocyanine percholorate (DiD) as a label. Lipids were presented on unilamellar vesicles, containing phosphatidylcholine (PC), biotin-phosphatidylethanol-amine (PE), DiD, and specific phospholipids (PI(3,4)P2, PI(4,5)P2 or PI(3,4,5)P3). The lipid vesicles were immobilized on biotin-PEG-passivated microscope slides aided by neutravidin at single-vesicle resolution and visualized by a prism-type total internal reflection fluorescence (TIRF) microscope. As described above, cells supernatants from cells expressing cPH_{TAPP1}-GFP, PH_{CRAC}-YFP, PH_{PLC}-YFP and various CynA-GFP constructs were collected and were present in the flow chamber during data acquisition. Standard deviation from mean was calculated from 10 or more different imaging areas. Single-molecule co-localization and assembly plot analysis are described previously (99).

Cell fixation

Dictyostelium cells expressing cPH_{TAPP1}-GFP, cPH_{TAPP1}-RFP or Dd5P4-GFP were allowed to attach to coverglass in a two-well chamber and cultured overnight in low fluorescence media (ForMedium, Norfolk UK). Cells were fixed with 2% buffered paraformaldehyde with .25% Glutaraldehyde and 0.1% Triton X-100 in HL5 for 10 minutes at room temperature, then quenched in 1mg/mL Sodium Borohydride for three minutes, then washed twice with TBS (supplemented with 0.25% BSA and 0.05% Triton X-100). The cells were visualized using the

Zeiss LSM800 confocal microscope. In each experiment, images from different samples were taken consecutively using identical settings.

cAMP Stimulation Assay

Cells were developed in suspension, by pulsing with 50 nM cAMP every 6 min at 2×10^7 cells/mL for 4-5 h. Then, cells were diluted in 450 µl DB and were plated in 8-well chambers and allowed to adhere for 5-20 min. Cells were incubated with latrunculin A for 20-30 min. Time-lapse images at 5 s intervals were acquired using confocal microscope during which 50 µl cAMP solution (10 µM) was added. The chamber and the cells could not be perturbed to keep observing the same cells in the same field. Time-lapse confocal imaging was performed again with stimulation by the same concentration of cAMP. The same process was repeated three times using other wells of cells.

Micropipette assay

Differentiated cells were plated on one-well coverslip chambers (NalgenNunc; LabTek) filled with 1-2 mL DB. A micropipette filled with 1 µM cAMP was placed into the middle of the field. Chemotaxis assays using a micropipette were recorded under the Zeiss Observer Z.1 inverted microscope. Images were taken at 10% lamp intensity, 200 msec exposure, and 40x oil objective. All experiments were performed at RT.

PH domain translocation assay

The assay was performed as described previously (100). Briefly, differentiated cells were shaken at 200 rpm in DB treated with 5 mM caffeine for 30 min at a density of 8×10^7 cells/mL, washed with PM buffer (5 mM Na2HPO4, 5 mM KH2PO4, and 2 mM MgSO4) twice, resuspended to 2×10^7 cells/mL in PM buffer, and kept on ice before assay. 200 µl aliquots of cells were filter lysed in PM buffer (with protease and phosphatase inhibitors) and in the absence or presence of 40 µM GTPγS and 10 µM cAMP. Reactions were incubated on ice for

2 min before being stopped by addition of 1 mL cold PM. Membranes were collected by centrifugation for 5 min at 15,000 × g. The cell lysates (whole cell) and membrane fractions (pellets) were collected.

Immunoblotting

Samples were resuspended in SDS sample buffer and boiled for 5 min. Electrophoresis was performed using 4–15% Tris·HCl polyacrylamide gels (#5671085, Criterion, Bio-Rad), and proteins were then transferred to a polyvinylidene fluoride membrane. The membranes were blocked and incubated with primary antibodies in 5% BSA in TBST overnight. Then specific fluorescent conjugated secondary antibody was applied and prepared for imaging as per manufacturer's protocol (LI-COR Biosciences). Blots were then imaged on a LI-COR Odyssey CLx at high resolution and signal intensities were measured using image J. The primary antibodies used in the studies were: Anti–phospho-PKC (pan) antibody (rabbit monoclonal antibody), which was used to detect the phosphorylation of the ALs of both PKBA and PKBR1; Anti-Actin C4 1:1000 (MAB1501) (Cell Signaling); anti-GFP antibody (mouse, monoclonal; Roche).

The cell outlines were obtained manually and imposed on the images. The cell outline overlays were obtained using the 'Find Edges' and 'Time-Lapse Color Coder' in Fiji.

The cell tracking presented were analyzed using the Tracking tool available from Gradientech (Uppsala Sweden).

Simulation of the front (F), back (B) and refractory (R) system

The excitable network is described by three interacting states. State F is mutually inhibitory to state B and initiates a negative feedback loop through state R. The system can be described by the following three partial differential equations:

$$\frac{\partial F}{\partial t} = D_F \nabla^2 F - \ a_1(F - a_F) - a_2(R - u_n) + \frac{a_3}{a_4^2 + B_n^2} + a_5$$

$$,where\ B_n = \left(\frac{1}{B} - \frac{b_1 a_F}{b_2}\right)^{-1}$$

$$\frac{\partial B}{\partial t} = D_B \nabla^2 B - \ b_1 B + \frac{b_2}{F}$$

$$\frac{\partial R}{\partial t} = D_R \nabla^2 R - \ c_1 R + c_2 F + \ c_3$$

The input signal is the stochastic variable un which is modeled as a normal random process with a decay term:

$$\frac{\partial u_n}{\partial t} = D_n \nabla^2 u_n - \ d_1 u_n + U_N$$

,where U_N is a normal random process of zero-mean and 0.2 variance.

The constants b1 and b2 are large so as to ensure a quasi-stationary distribution, such that:

Substituting this reciprocal relation to the excitable state equation, one can get the standard excitable two-species system described previously published work. These simulations were done on a one-dimensional space system – discretized into 314 points. Diffusion was simulated through the central difference approximation. The SDE toolbox of MATLAB was used for this purpose.

The simulations of cellular morphology were done using the level set framework (LSM). The LSM method and the parameters used are exactly similar to those discussed in our previous work.

Image Analysis

All images were processed using Fiji (like ImageJ) (National Institutes of Health) and MATLAB R2016a (MathWorks). To quantify the translocation of biosensors upon cAMP stimulation, the mean intensity of the membrane portion and cytosol portion were measured and the ratio was calculated using image J. Cells were segmented by a multistep process using

commands from the Image Processing Toolbox in MATLAB, and the kymographs were also created by MATLAB. Colors were assigned linearly in the same fashion across all kymographs, with blue indicating the lowest intensity and red the highest intensity. Biosensor patches were defined regions of fluorescent intensity that are two-fold over background.

Statistical Analysis

Mean values and standard deviations/ standard error of the mean were calculated and used to assess differences between two groups by GraphPad Prism 5.0. One-way ANOVA was carried out for multiple comparisons by GraphPad Prism 5.0. P-values < 0.05 was considered a statistically significant difference. Representative images presented in figures were repeated in more than three independent experiments.

2.6 Author contributions

X.L. performed most experiments, and M.E. performed experiments regarding RasGAP and RapGAP. N.S. and J.C. performed single-molecule binding assays. S.B. conducted computational simulations. J.B. and Y.L. made the constructs and RG2- and RG3- cell lines. P.N.D supervised the study.

Chapter 3

Reverse Fountain Flow of PI(3,4)P2 Polarizes Cells

Modified from:

Xiaoguang Li, Dhiman Sankar Pal, Debojyoti Biswas, Pablo A. Iglesias, and Peter N. Devreotes*. Reverse fountain flow polarizes cells. *EMBO J* (Accepted).

3.1 Summary

The ability of cells to polarize and move toward external stimuli plays a crucial role in development, as well as normal and pathological physiology. Migrating cells maintain dynamic complementary distributions of Ras activity and phosphatidylinositol-3,4-bisphosphate (PI(3,4)P2). Here we show lagging edge component PI(3,4)P2 also localizes to retracting leading edge protrusions and nascent macropinosomes, even in the absence of phosphatidylinositol 3,4,5-trisphosphate (PIP3). Once internalized, the macropinosomes break up into smaller PI(3,4)P2-enriched vesicles, which fuse to the plasma membrane at the cell rear. The phosphoinositide then diffuses towards the front, where it is degraded. A computational model confirmed that this cycle brings about a stable back-to-front gradient. These results uncover a surprising “reverse fountain flow” of PI(3,4)P2 that regulates polarity.

3.2 Introduction

Chemotaxis or directed cell migration, is fundamental for a multitude of physiological and pathophysiological processes including organ formation during development, angiogenesis, wound healing, immune responses and cancer metastasis (44, 47, 128, 129). In response to chemical stimulus, migrating cells display functionally distinct leading and lagging edges by relocating proteins or their activities selectively to the poles. Some events such as Ras and PI3K activation, or PIP3 accumulation are selectively activated or localized at the leading edge and are referred to as 'front' events. Others, like Myosin II and PTEN distributions, behave in a complementary fashion and are referred to as 'back' events. These distributions of front and back molecules or activities are a crucial first step in establishing polarity and guiding cell migration, and are maintained even in the absence of a chemoattractant gradient (67, 102, 130-133).

There exist different physiological situations such as macropinocytosis that parallel cell migration where such complementary distributions of molecules are conserved. Both macropinocytosis and migration require extensions of actin driven protrusions. During macropinocytosis in *Dictyostelium* amoeba, the extending edges of the forming cups are decorated with front components, such as activated Ras and PIP3, whereas back components like PTEN, Myosin II, PI(3,4)P2, and GAP proteins localize to the base (48, 49, 83, 102, 134-137). The conserved arrangement of these molecules in the macropinocytic cups and along the cell perimeter of migrating cells suggests a relationship between these two processes.

PI(3,4)P2 is reported to be important in both macropinocytosis and cell migration. In macropinocytosis, transient and sequential emergence of PI(3,4,5)P3 and PI(3,4)P2 is necessary (71, 82, 126, 135, 138). In migrating *Dictyostelium* cells and zebrafish neutrophils, PI(3,4)P2 is distributed in a back-to-front gradient (48, 74). There is a mutual inhibition

between PI(3,4)P2 and Ras activities: when Ras is activated in the front, PI(3,4)P2 goes down; conversely, depletion of PI(3,4)P2 leads to elevated Ras activity. This mutual inhibitory feedback loop ensures that the back of the cell is silent, and the front is active. The resemblance between the back-to-front gradient across the cell and across the macropinocytic cups led us to hypothesize that PI(3,4)P2-decorated macropinosomes could be a crucial component linking macropinocytosis and cell migration.

Here, we demonstrate that there is an ongoing flow of vesicular PI(3,4)P2 through the cell and a compensatory forward flow along the membrane, which establishes a back-to-front gradient of this phosphoinositide. Previous models have suggested that such vesicular and plasma membrane flows are important for cell migration, although the directions were reversed (139-141). Our findings show that PI(3,4)P2 is internalized on macropinosomes and transported on microtubules into the cytosol. These anterior macropinosomes break up into several smaller PI(3,4)P2-enriched vesicles, which dock and fuse at the rear of the migrating cell. This surprising reverse fountain flow of PI(3,4)P2 and its role in establishing the back-to-front gradient may be essential for polarity in specific modes of cell migration.

3.3 Results

3.3.1 PI(3,4)P2 at the back diffuses towards the front

In migrating *Dictyostelium* amoeba, PI(3,4)P2, observed using a tandem PH-domain biosensor tPH-CynA, is distributed to the back and is complementary to F-actin and active Ras (Figures 19A and B). To investigate the dynamic distribution of PI(3,4)P2 at the back, we fused a green-to-red photoconvertible fluorescence Kikume Green-Red (KikGR) with tPH-CynA and expressed it in the cells. Using the Zeiss 780 bleaching mode with a 405 nm laser, photoconversion caused a decrease in green fluorescence and a simultaneous increase in red fluorescence. We photo-converted tPH-CynA-KiKGR in a small region of the membrane at the back of the cell and tracked the green and red channels. Photoconverted tPH-CynA diffused symmetrically along the membrane towards the front by 50 s (Figure 19C and D). The signal decreased by less than 10 percent in the first 60 s (and less than 20% in the first 5 minutes) following photoconversion, indicating there is little exchange of membrane and cytosolic PI(3,4)P2 biosensor (Figure 19E). The lateral diffusion of the photoconverted tPH-CynA on the membrane was found to be 2.05 $\mu m^2/s$ by comparing the experimental profiles with the simulated profiles from a stochastic simulation for a wide range of diffusion constants (see Methods). At the side of the cell, the distribution of photoconverted PI(3,4)P2 biosensor spread asymmetrically, skewed towards the back of the cell and the total fluorescence decreased gradually during 145 s, the increase in the skewness was 52% in 60 s (Figure 19F and G). We reasoned that PI(3,4)P2 diffuses bi-directionally on the membrane on the side of the cell, but it is degraded faster toward the front. Taken together, these observations suggest that there is a source of PI(3,4)P2 at the rear of the cell and that PI(3,4)P2 is degraded as it diffuses toward the front.

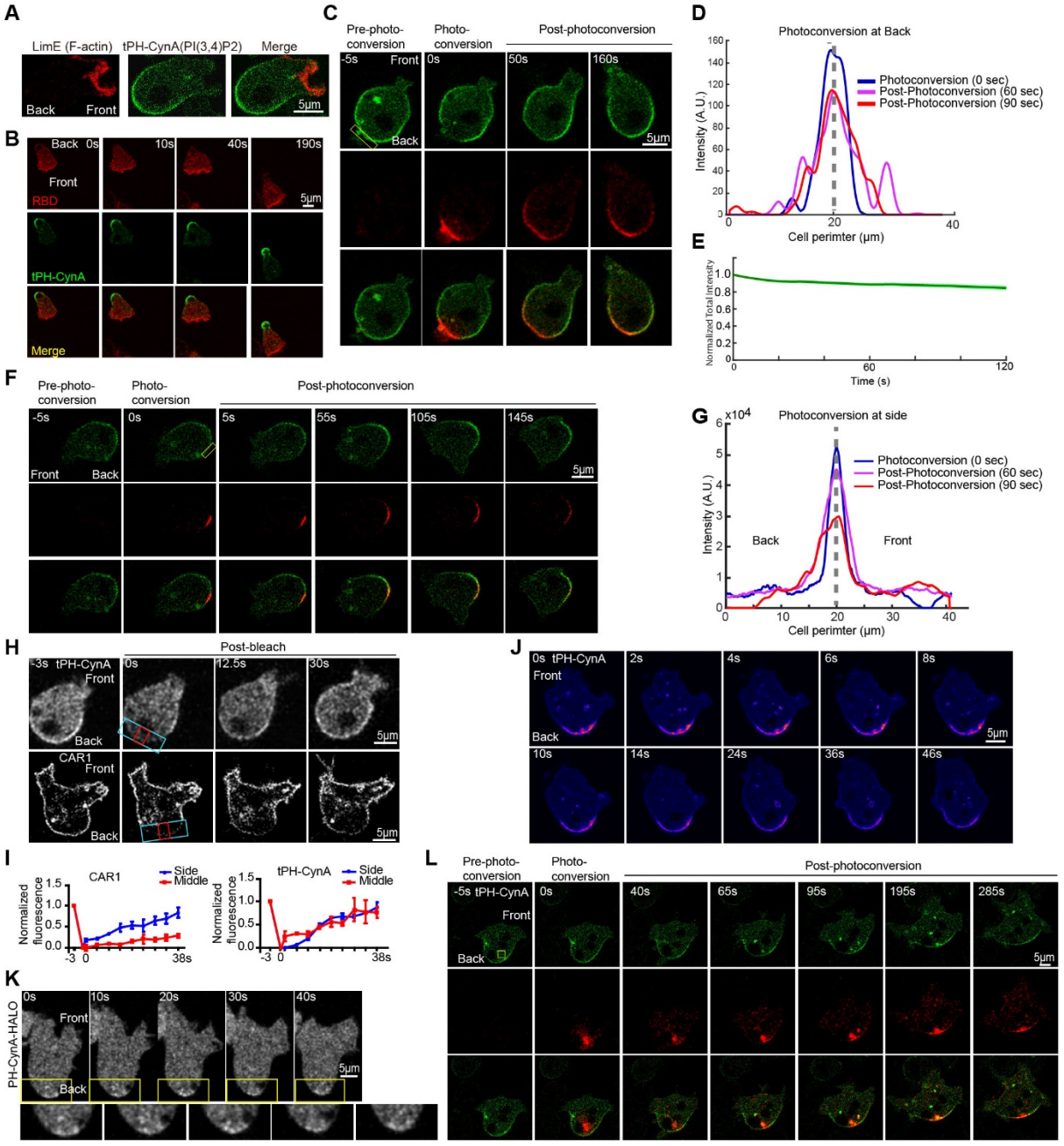

Figure 19. Small PI(3,4)P2 vesicles supply PI(3,4)P2 to the back of migrating *Dictyostelium* cells.
(A). Confocal images of growth stage wild-type *Dictyostelium* AX3 cell co-expressing tPH-CynA-KikGR (green) and an F-actin biosensor LimE-RFP (red). Front and back of the cell are shown. (B). Time lapse confocal images of growth stage AX3 cell co-expressing tPH-CynA-KikGR (green) and an activated Ras biosensor, RBD-mCherry (red). Front and back of the cell are shown. (C). Time-lapse confocal images of tPH-CynA-KikGR expressing AX3 cells. Back region of cells was photoconverted from green fluorescence to red at t=0s. Front and back of the cell are shown, box showing the photoconverted region. (D). Profiles of the converted red fluorescence at the back remain almost symmetric over time. (E)..Temporal profile of normalized intensity of total converted red fluorescence. Mean ± SEM is shown for n = 14 cells. (F). Time-lapse confocal images of tPH-CynA-KikGR expressing AX3 cells during photoconversion. Side region of cells was photoconverted at time 0. Green fluorescence was converted to red. Front and back of the cell are shown. Box shows the photoconverted region. (G). Profiles of the converted red fluorescence at side become skewer (steeper near the front) over time. (H). Confocal fluorescent images of tPH-CynA-KikGR (top) and CAR1-mcherry (bottom) *Dictyostelium* AX3 cell showing the bleached area and the side (blue) and middle (red) boxes where

the fluorescence recovery is monitored. Front and back of the cell are shown. (I). The graphs depict the recovery of CAR1-mcherry (left) and tPH-CynA-KikGR (right). (J). Time-lapse confocal images of tPH-CynA-KikGR expressing AX3 cells showing docking events at the back of a migrating *Dictyostelium* cell. Front and back of the cell are shown. (K). Time-lapse confocal images of PH-CynA-HALO expressing AX3 cells showing high PH-CynA vesicles accumulation at the back of a migrating *Dictyostelium* cell. Front and back of the cell are shown. (L). Time-lapse confocal images of tPH-CynA-KikGR (green) expressing AX3 cells. Back cortical region of cell was photoconverted at time 0. Green fluorescence was converted to red. Front and back of the cell is shown, box showing the photoconverted region.

3.3.2 Small PI(3,4)P2 vesicles supply PI(3,4)P2 to the back of migrating cells

To determine the nature of the source of PI(3,4)P2 at the back, we conducted fluorescence recovery after photobleaching (FRAP). As a control we used chemoattractant receptor cAR1, which is uniformly distributed on the plasma membrane of cells. We photobleached a small portion of the periphery at the back of the cell and carefully monitored the fluorescence recovery. As expected, for cAR1, the recovery proceeds in a vectoral fashion from the adjacent unbleached areas of the membrane, since the receptor diffuses in the plane of the membrane. In contrast, for tPH-CynA there was an even fluorescence recovery in the middle and boundaries of the bleached zone (Figure 19H and I). Since the biosensor stably marks PI(3,4)P2 (Figure 19E), this shows that there is a cytosolic source of PI(3,4)P2.

We next carefully examined the dynamic behavior of PI(3,4)P2 at the back using two similar biosensors with different affinities and tags, tPH-CynA-KikGR and PH-CynA-HALO. With both biosensors, we observed small PI(3,4)P2-containing vesicles docking in the back region (Figures 19J and K). To confirm this result, we photoconverted the intracellular pool of small vesicles close to the membrane at the back of the cell. We found that PI(3,4)P2-containing small intracellular vesicles moved close to the membrane, and appeared to dock with it, whereupon PI(3,4)P2 diffused away quickly (Figure 19L). We propose that small vesicles fuse with membrane and diffuse fast, but we allow the possibility that vesicles dock at the back and then slide along the membrane to the front.

3.3.3 PI(3,4)P2 trails F-actin and PIP3 on the leading edge macropinosomes

Having established that the STEN and CEN patterns could be recreated, we next considered the kinetics of wave propagation. To understand the origins of these vesicles, we sought the first appearance of enriched PI(3,4)P2. There was a low amount of PI(3,4)P2 on the membrane at the front of the cells, which disappeared from newly formed actin-rich protrusions. PI(3,4)P2 then appeared de novo as the leading edge protrusions retracted or evolved into nascent macropinosomes(Li et al., 2018). We directly compared the localization of PI(3,4)P2 with newly polymerized F-actin. Time lapse two-color images showed that F-actin appeared on the tips of forming macropinosomes in the regions where PI(3,4)P2 had disappeared, then gradually dissipated as the structures closed. Simultaneously, PI(3,4)P2 appeared and remained on the fully formed macropinosomes. The changes in intensity and distribution of these two biosensors on the forming macropinosomes were shown (Figure 20A). Quantification of relative intensities of F-actin and PI(3,4)P2 on macropinosomes at different time points showed that PI(3,4)P2 lags F-actin and lasts longer (Figure 20C).

Next, we compared the dynamic localization of PI(3,4)P2 with PIP3, detected by the biosensor PH-Crac. PIP3 resembles the pattern of F-actin, increasing and then decreasing during the formation of macropinosomes. Again, dynamic distributions of tPH-CynA showed a complementary pattern only appearing on the forming macropinosomes (Figures 20B and D). This distribution of PI(3,4)P2 was further demonstrated by another established biosensor PH-TAPP1, which localized to macropinosomes only as PIP3 is subsiding (Figure 20E). These data showed that lagging edge component PI(3,4)P2 localized to retracting protrusions and nascent macropinosomes in a distinct pattern compared with F-actin and PIP3.

To determine the prevalence of PI(3,4)P2-enriched vesicles in membrane trafficking, we applied the lipophilic dye, FM4-64. It fluoresces only when it is incorporated in the plasma membrane and, once internalized, it becomes trapped in intracellular vesicles (46). Thus, FM4-64 labelling is a useful tool to visualize the membranes of pre-macropinosomes. When FM4-64 was added during a live cell imaging sequence, we observed increasing plasma membrane labeling within 100 s. By 110s the signal internalizes to label intracellular compartments or macropinosomes, which were labelled by PI(3,4)P2. Taken together, PI(3,4)P2 is detectable on majority of the dye labeled macropinosomes at the leading edge of the cells (Figure 20F).

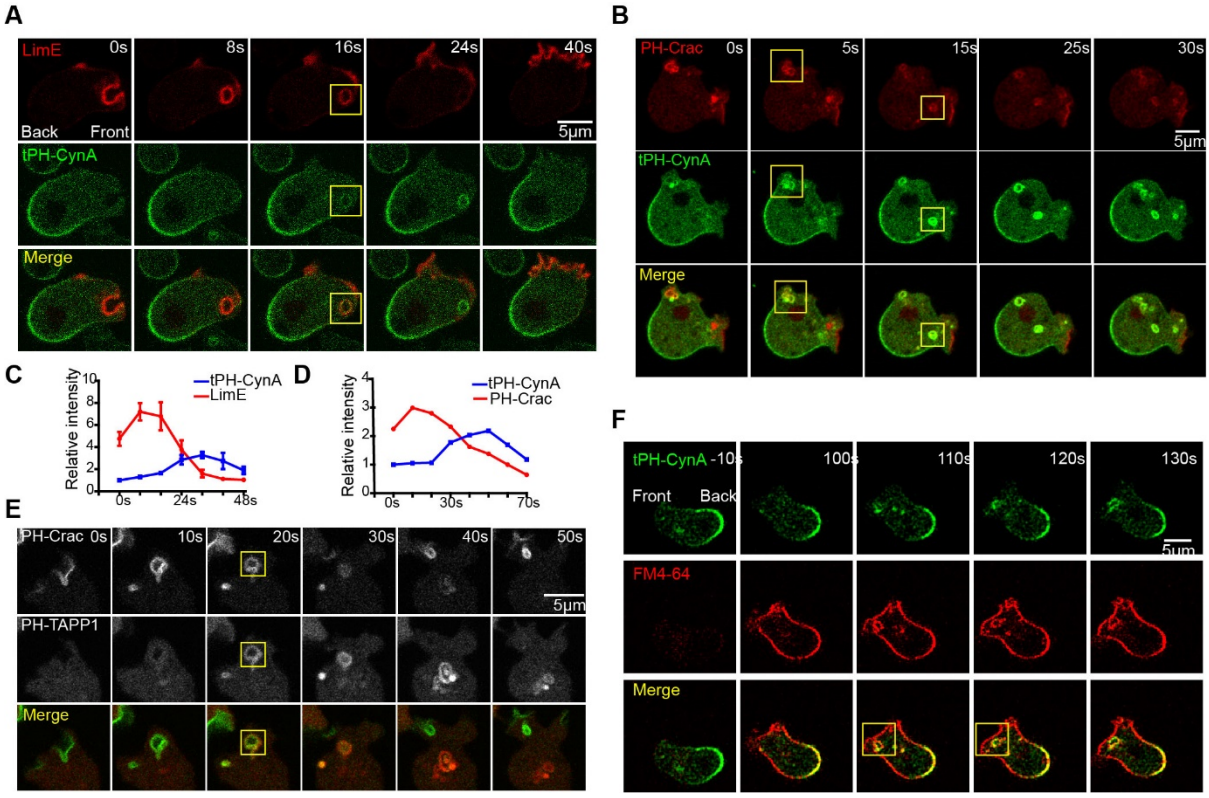

Figure 20. PI(3,4)P2 trails F-actin and PIP3 on the leading edge macropinosomes.
(A). Time-lapse confocal images of *Dictyostelium* AX3 cell co-expressing tPH-CynA-KikGR (green) and LimE-RFP (red). Front and back of the cell is shown. (B). Time-lapse confocal images of *Dictyostelium* AX3 cell co-expressing tPH-CynA-GFP (green) and PH-Crac-RFP (red). (C). Relative intensities of tPH-CynA-KikGR on macropinosomes and LimE-RFP on macropinosomes in experiments in A. (D). Relative intensities of tPH-CynA-KikGR on macropinosomes and PH-Crac-RFP on macropinosomes in experiment in B. (E). Time-lapse confocal images of AX3 cell co-expressing PH-Crac-GFP (green) and another established PI(3,4)P2 biosensor tPH-TAPP1-RFP (red). (F). Time-lapse confocal images of tPH-CynA-KikGR (green) expressing wild-type AX3 cells. FM4-64 (red) was added at time 0 during live cell imaging. Front and back of the cell are shown.

3.3.4 PI(3,4)P2 appears in absence of PIP3

We next assessed the relative contribution of PIP3 degradation to PI(3,4)P2 levels on the vesicles and plasma membrane with PI3K inhibitors and in PI3K1-2- cells. In wild-type cells, we investigated PI(3,4)P2 dynamics before and after addition of PI3K inhibitor, wortmannin. Surprisingly, PI(3,4)P2 remained on the plasma membrane at the back of the cell after wortmannin treatment while PIP3 was depleted (Figure 21A). Kymograph showed that over time PIP3 disappeared and line scan quantification demonstrated that dynamics distribution of PI(3,4)P2 is similar before and after PI3K inhibition (Figure 21B and C). To verify this result, we first treated cells with Latrunculin A to eliminate the cell shape changes, and then treated cells with the well-established PI3K inhibitor LY2924002. Again, PI(3,4)P2 remained on the membrane and, in fact, its level was even higher (Figures 21D and E). To confirm this observation, we treated PI3K1-2- cells with latrunculin A and found that even though there is no detectable PIP3 on the membrane, PI(3,4)P2 levels are nearly maintained (Figures 21F and G). Furthermore, PI3K1-2- cells expressing tPH-CynA-KiKGR and LimE-RFP showed that localization of PI(3,4)P2 on macropinosomes was also maintained (Figures 21H and I). Taken together, these observations suggest that PI(3,4)P2 dynamics can be regulated in the absence of PIP3, and this regulation is conserved in diverse cell types.

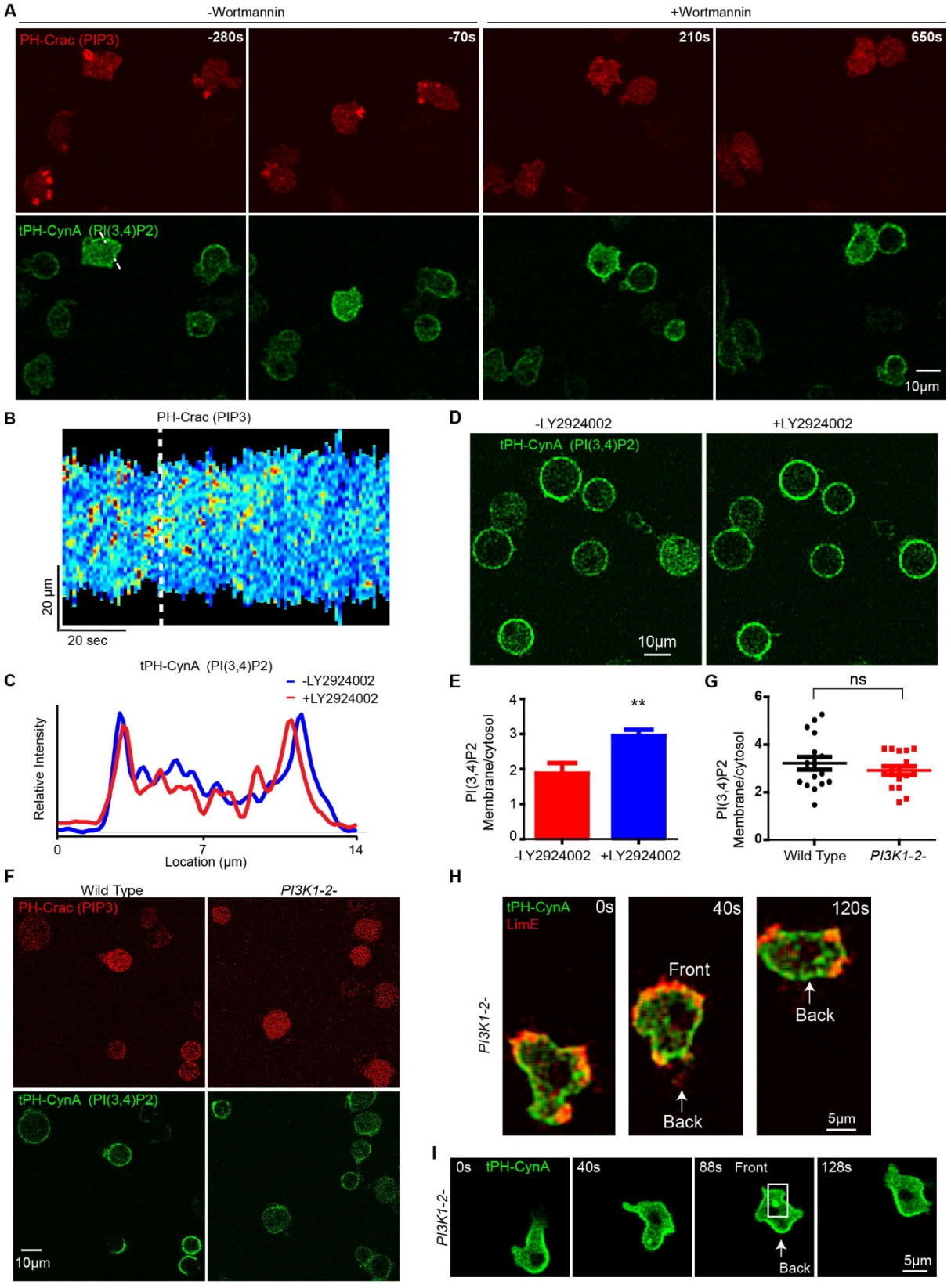

Figure 21. PI(3,4)P2 appears in absence of PIP3.
(A). Time-lapse confocal images of wild-type AX3 cells expressing tPH-CynA-KikGR (green) and PH-crac (red) before and after PI3K inhibition by 2 μM Wortmannin. (B). Kymographs of PH-Crac intensity on the

perimeter of one cell undergoing random migration in (A). (C). Intensity plot across the white dotted line in tPH-CynA-KikGR expressing cell before and after Wortmannin treatment in (A). (D). Confocal images of tPH-CynA-KikGR expressing wild-type *Dictyostelium* AX3 cells before (left) and after (right) LY2924002 treatment. (E). Ratio of membrane to cytosol intensity of tPH-CynA-KikGR in wildtype *Dictyostelium* AX3 cells before and after LY2924002 treatment, **P ≤ 0.01 versus -LY2924002 group (mean±SEM, n = 7). (F). Confocal images of tPH-CynA-KikGR (green) and PH-Crac (red) expressing wild-type *Dictyostelium* AX3 cells (left) and PI3K1-2- *Dictyostelium* cells (right) treated with 5 µM Latrunculin A. (G). Ratio of membrane to cytosol intensity of tPH-CynA-KikGR in wildtype Ax3 and PI3K1-2- cells. There was no statistically significant difference of the biosensor on the membrane between the two groups (mean±SEM, n = 17). (H). Confocal images of tPH-CynA-KikGR (green) and LimE (labeling F-actin) expressing PI3K1-2- cells. Front and back of the cell are shown and white arrow showing the back localization. (I). Confocal images of tPH-CynA-KikGR (green) expressing PI3K1-2- cells, white box showing the vesicle, and white arrow showing the back localization.

3.3.5 PI(3,4)P2 macropinosomes are transported along microtubules and break apart

To determine the relationship between PI(3,4)P2-enriched vesicles and the microtubule network, we fixed cells expressing the PI(3,4)P2 biosensor, tPH-CynA-KikGR, stained them with an anti-α-tubulin antibody, and performed z-stack confocal microscopy. In untreated wild-type AX3 cells, the microtubular network was intact and PI(3,4)P2-enriched vesicles appeared to be associated with microtubules (Figure 22A).

Treatment of the wild-type AX3 cells with 20 µM Nocodazole for 5 min caused a substantial disassembly of the microtubule network. Simultaneously, more PI(3,4)P2-enriched vesicles were seen, which were no longer associated with the microtubules and were clustered around the closure of the macropinocytic cups (Figure 22B). The LimE channel demonstrated that macropinocytic cups continued to form, but the increase in the number of vesicles in the tPH-CynA channel was due to a slower disappearance (Figures 22C and D). The macropinosomes were trapped along the membrane and were unable to be internalized in 50 sec (Figure 22E). The number of vesicles viewed per minute and the vesicle lifetime increased upon Nocodazole treatment (Figure 22F).

We investigated whether inhibition of processing of PI(3,4)P2-enriched macropinocytic vesicles by genetic perturbation would abrogate its accumulation at the back of a migrating

Dictyostelium cell. To test this hypothesis, we used a racH- *Dictyostelium* strain whose vesicle trafficking is disrupted due to defective acidification of early endosomes. This impairs macropinocytosis and chemotaxis (142, 143). As shown in Figure 22G, whereas a back-to-front gradient in PI(3,4)P2 membrane association was apparent in wild-type *Dictyostelium* AX2 cells, in the racH- null cells "back" regions were weaker and there were more cytosolic PI(3,4)P2-enriched vesicles. Line scans of pixel intensity across wild-type or mutant cells confirmed greater PI(3,4)P2 accumulation at the back of wild-type cells (Figure 22H).

Next, we quantified the lifetimes of the PI(3,4)P2-enriched vesicles, their numbers per unit of time, surface areas, and membrane-cytosol ratio. In racH- cells, the vesicles were almost twice as long-lived as those in wild-type AX2 cells (Figure 22I). The vesicles in the mutant were also 40% greater in number and 63% larger (Figures 22J and K). Moreover, the plasma membrane-to-cytosol ratio of PI(3,4)P2 was 2.30 ± 0.67 in wild-type AX2 cells but 0.88 ± 0.76 in racH-null cells (Figure 22L and M). Assuming that the degradation rate of PI(3,4)P2 is the same in the mutant and wild-type, this result suggests that at least 50% of the PI(3,4)P2 on the membrane depends on vesicular trafficking.

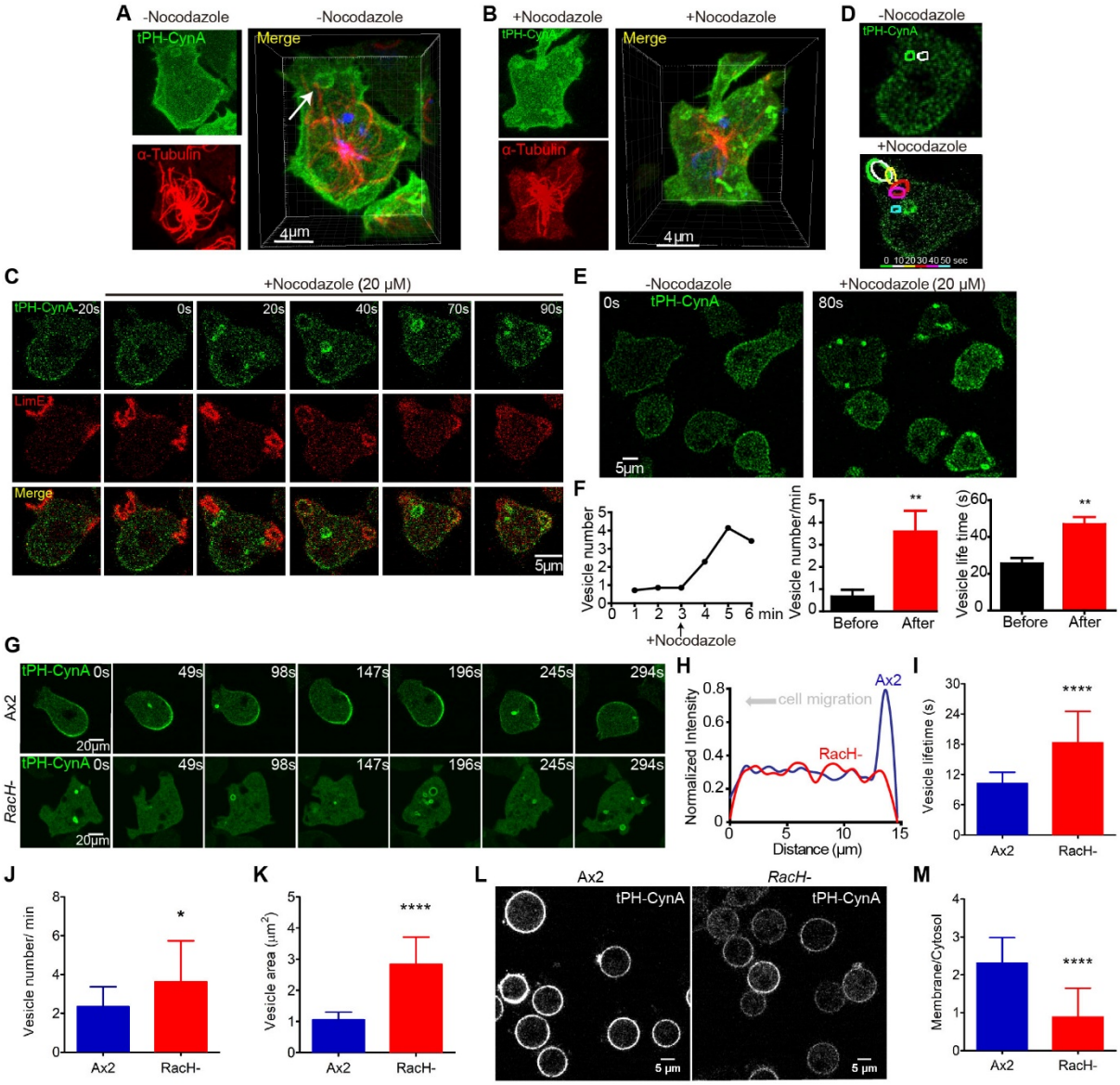

Figure 22. Macropinocytic vesicle processing is necessary for PI(3,4)P2 enrichment at the back of migrating cells.

(A). Confocal images showing localization of PI(3,4)P2 (tPH-CynA-KiKGR ; green) and α-tubulin (red) in fixed wild type *Dictyostelium* AX3 cells in 3D. (B). Confocal images showing localization of PI(3,4)P2 (green) and α-tubulin (red) in fixed AX3 cells after Nocodazole treatment in 3D. (C). Time-lapse confocal images showing dynamic localization of PI(3,4)P2 (green) and F-actin (red) in wild-type *Dictyostelium* cells. Nocodazole was added at time 0 during live cell imaging. (D). Color-coded tracing of vesicle at 10-sec intervals from experiment in C. (E). Time-lapse confocal images showing dynamic localization of PI(3,4)P2. Nocodazole was added at time 0 during the live cell imaging. (F). Quantification of vesicle number, vesicle number/min, and vesicle lifetime (s) from experiment in E. **P ≤ 0.01 versus After Nocodazole group; mean±SEM (n = 10). (G). Time-lapse confocal images of individual cells of growth-stage wild-type *Dictyostelium* AX2 or RacH- strain highlighting tPH-CynA-KikGR-coated macropinocytic vesicles and back-to-front membrane gradient. Images were captured every 7 sec.

(H). Intensity plot across wild-type *Dictyostelium* AX2 or RacH- strain in image "147 s" shown in (G). (I). Lifetime, (J) number or (K) area of tPH-CynA-KikGR coated macropinocytic vesicles in wild-type AX2 and RacH− cells. *P ≤ 0.05, ****P ≤ 0.0001 versus AX2 group; mean ± SEM (n = 20). (L). Representative confocal images of tPH-CynA-KikGR in wild-type *Dictyostelium* AX2 or RacH− cells treated with 5 μM latrunculin A

Scale bar: 5 μm. (M) Ratio of membrane to cytosol intensity of tPH-CynA-KikGR in wild-type *Dictyostelium* AX2 and RacH− cells. ****P ≤ 0.0001 versus AX2 group; mean ± SEM (n = 33).

Under live-cell 3D super-resolution imaging, we further found the macropinosomes are transported into the cytosol where they appear to break apart into smaller "satellite" vesicles and disappear (Figure 23A). In Nocodazole treated or RacH- cells, macropinosomes remained on the perimeter and were not processed into the smaller vesicles. Taken together, these results suggest that PI(3,4)P2-enriched macropinosomes are transported along microtubules into the cytosol where they are likely to be processed into smaller vesicles and disperse.

3.3.6 A link between PI(3,4)P2 on front macropinosomes and the back to front gradient of PI(3,4)P2

Our observations on the "satellite" vesicles suggest these might be the same as the docking vesicles at the back (Figure 19J-L). To gain insight into the connection between PI(3,4)P2 on the front macropinosomes and the back-to-front gradient of plasma membrane, we photoconverted the PI(3,4)P2 biosensor, tPH-CynA-KiKGR, on late-macropinosomes at the leading edge of the cells and tracked the signal. Figure 23B shows an example of photo-conversion of a front macropinosome which eventually resulted in increased signal at the back of the cell. We quantified the relative percentage of green and red signal upon photoconversion. An average 4.97% of green fluorescence was converted to red while 51.43% of the generated red fluorescence ended up at the back, indicating that vesicles labelled with PI(3,4)P2 biosensor travel all the way to the back of membrane before the biosensor dissociates (Figure 23C). The data argues against the alternative possibility that the biosensor dissociates from the macropinosomes and rebinds to smaller vesicles which go to the back (Figure 23D).

Observation of docking and fusing events in single cells are limited by the small cell boundary. Electrofused "giant" cells provide a more accessible system for characterizing these dynamics.

Giant cells have multiple “front” regions, which include F-actin, ruffles, and macropinosomes, and “back” regions which lack these events(Gerhardt, Ecke et al., 2014, Gerisch, Ecke et al., 2013). In these cells, we observed large and small PI(3,4)P2 vesicles arising in multiple front regions and others docking at the nearby back regions. This is consistent with docking activities observed in single cells (Figure 23E).

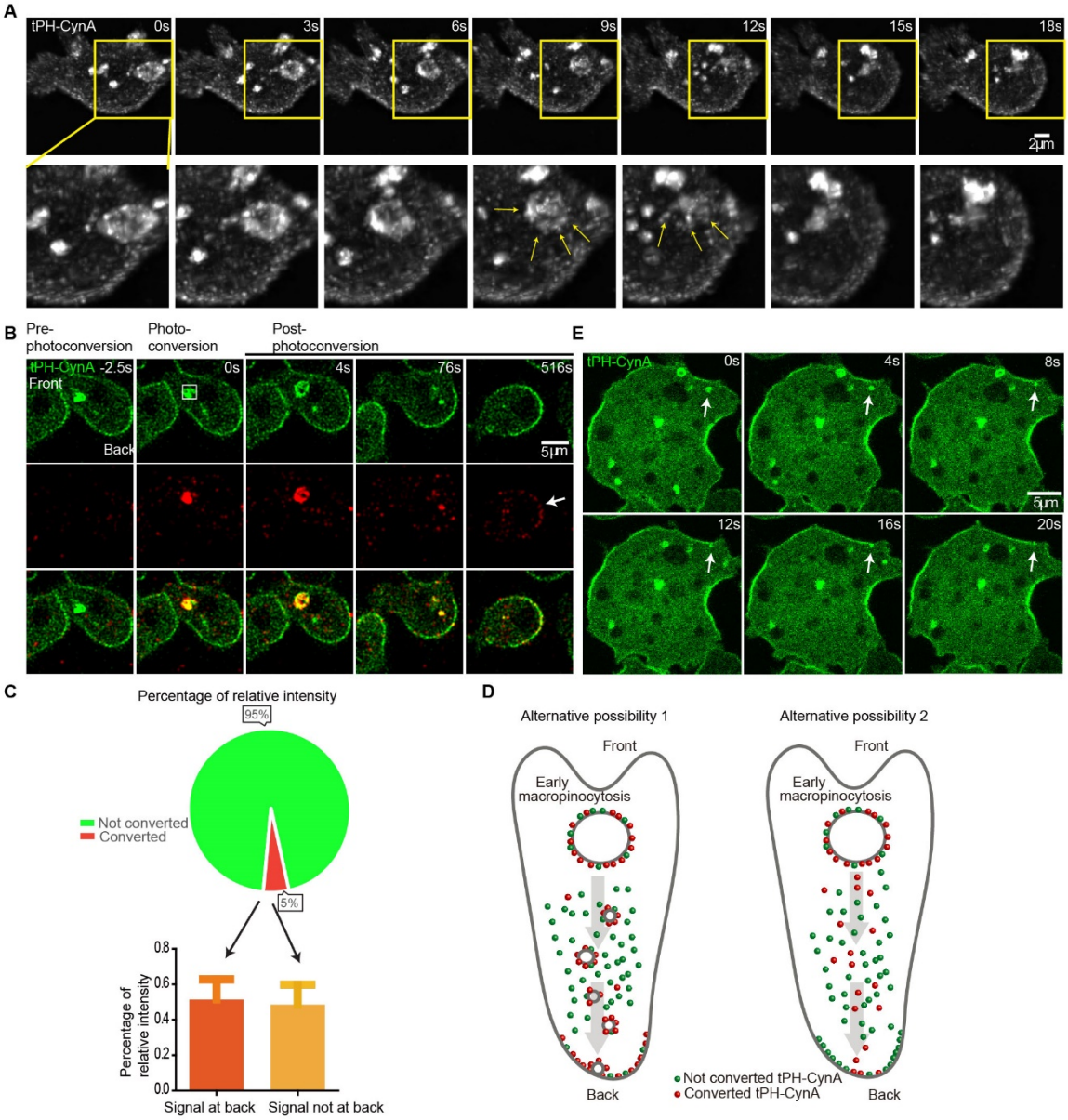

Figure 23. A link between PI(3,4)P2 on front macropinosomes and the back to front gradient of PI(3,4)P2.

(A). Time-lapse confocal images of tPH-CynA-KikGR expressing *Dictyostelium* AX3 cells. Below are zoomed in images from images above. Yellow arrows point to small satellite vesicles. (B). Time-lapse confocal images

of tPH-CynA-KikGR expressing *Dictyostelium* AX3 cells. The macropinosome at the front of the cell was photoconverted at time 0. White arrow points to PI(3,4)P2 localization at the back of the membrane. Cell front and back are shown, box showing the photoconverted region. (C). Pie chart quantification of percentage of relative intensity of total green fluorescence (not converted) and converted red fluorescence (converted), showing 4.97% of total fluorescence was converted to red (top). Bottom: 4.97% of total fluorescence was converted to red, and around 50% of converted red fluorescence end up at the back of membrane (red), less than 50% of the converted red fluorescence not at back (orange). (D). Schematic representation of two potential working alternative possibilities. Red dots show photoactivated tPH-CynA, green dots show not converted tPH-CynA. Left shows that if the biosensor remains associated with the vesicles, a larger proportion of the red signal will appear at the back. Right shows that if the biosensor disassociates from the vesicles, a much smaller amount of the red signal will appear at the back. (E). Time-lapse confocal images of tPH-CynA-KikGR in giant *Dictyostelium* AX3 cells.

We developed a stochastic mathematical model to explore the effect of different vesicle fusion parameters on the creation and maintenance of a stable back region in a cell (see methods). We found that for creation of a stable back, the directed insertion of the satellite vesicles into the regions of highest PI(3,4)P2 levels on the membrane was an important condition (Figure 24A).

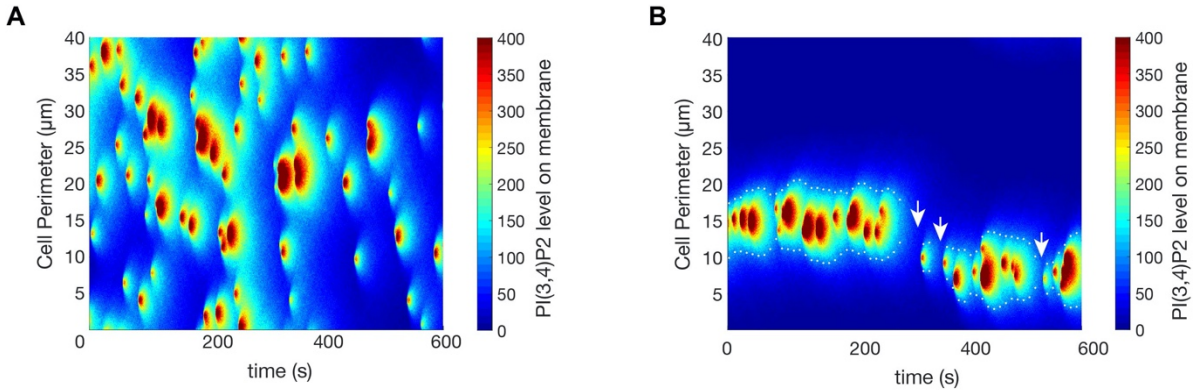

Figure 24. Simulated kymographs.
(A). Kymograph with random insertion of the satellite vesicles with same set of parameters as used in the case of less polarized cell. (B). Kymograph with directed insertion of the satellite vesicles with increased mean arrival time (20 sec) and the same decay rates as of the less polarized cell. The longer arrival time results discontinuities in the back profile (indicated by the white arrows) as explained in the results section of the manuscript.

Other important parameters were the mean arrival time of the PI(3,4)P2 vesicles, and the rate of PI(3,4)P2 diffusion and decay (Figures 25A and B). Increase in the mean arrival time resulted discontinuity in the back profile unless the decay rate was reduced appropriately (Figures 24B). Figures 25A and B show the results of increasing the mean arrival time of the PI(3,4)P2 vesicles and decreasing the PI(3,4)P2 decay rates. These changes created a broader

back without causing a large change in the overall amount (the change was less than 10%). A broader distribution of PI(3,4)P2 at the back would imply a larger fraction of the cell is inactive, which would make the cell more polarized. Consistently, our experimental results showed that the decay rate in more polarized cells was indeed four-fold lower than that in less polarized cells, and the extent of cell membrane covered by PI(3,4)P2 is smaller in less polarized cells compared to more polarized cells. The mean relative width of the back regions and decay rate obtained from the simulated kymographs was consistent with experimental results (Figures 25C and D).

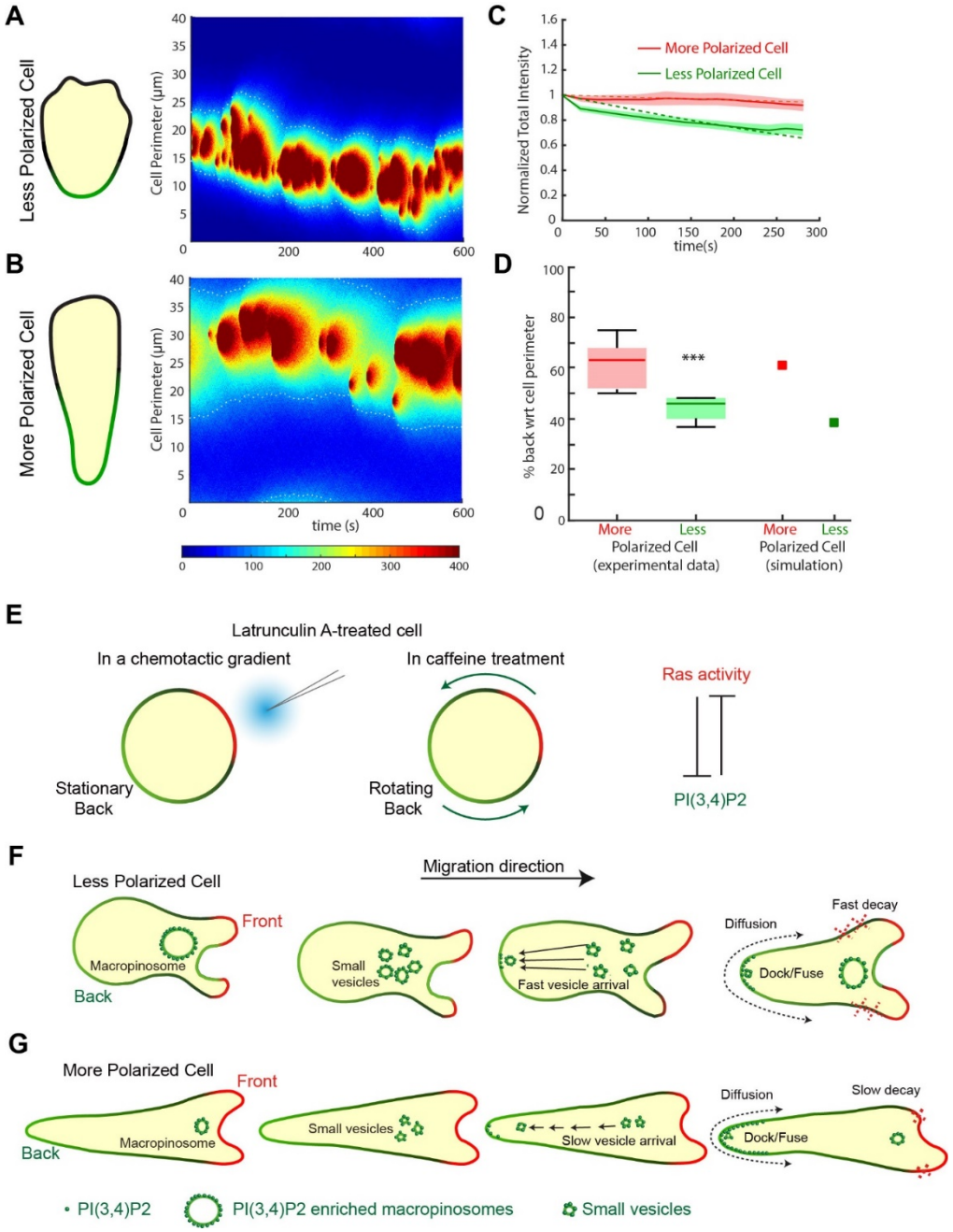

Figure 25. A link between PI(3,4)P2 on front macropinosomes and the back to front gradient of PI(3,4)P2.

(A). Simulated kymograph of a less polarized cell with a narrow PI(3,4)P2 enriched region. The white dashed lines correspond to the periphery of the back regions which spanned on average 30% of the cell perimeter. (B). Simulated kymograph of a more polarized cell with broader PI(3,4)P2 enriched region compared (A). Slower vesicle arrival time and reduced decay rate for PI(3,4)P2 was assumed in comparison to parameters used for the simulation in (A). (C). Total intensity profiles (Mean ±SEM) of tPH-CynA-KikGR on the membrane over time show different decay rates for less polarized (green, n = 5) and more polarized (red, n = 8) *Dictyostelium* cells. The dashed lines show the respective single exponential fit to the data. Mean half time for vegetative cells = 7.5 min; for developed cells = 55 min (from single exponential fit to the data). (D). The boxplot shows the relative width of the back regions in less (green) and more (red) polarized *Dictyostelium* cells. The square markers of respective colors show the mean relative width of the back regions obtained from the simulated kymographs in (A) and (B). *** $P < 0.001$ (n = 5). (E). Schematic representation of our previous study demonstrating the mutual inhibition between Ras activity and PI(3,4)P2 which establishes polarity even in immobilized latrunculin

A treated cells in a chemotactic gradient (with stationary back) or in caffeine treatment (with rotating back). In *Dictyostelium*, caffeine is used to inhibit the synthesis of the chemoattractant cAMP. (F). Schematic representation of the working model in less polarized *Dictyostelium* cells. PI(3,4)P2 is internalized on macropinosomes and transported into the cytosol. These anterior macropinosomes break up into smaller PI(3,4)P2 vesicles, which dock and fuse at the rear of the cell. (G). Schematic representation of the working model in more polarized *Dictyostelium* cells. Slow vesicle arrival of the PI(3,4)P2 vesicles and slower decay rates of PI(3,4)P2 created a broader back.

To access how much the vesicular trafficking contributes to the overall production of PI(3,4)P2, we measured turnover before and after Latrunculin A treatment. Latrunculin A acutely blocks macropinosomes formation. After Latrunculin A treatment, there was a 30% decrease of tPH-CynA on the membrane and a photoconversion experiment showed that the degradation rate of PI(3,4)P2 decreased 3-fold (Figures 26, and Figure 19E). Together these data suggest that the vesicular trafficking is responsible for more than 50% of the levels of PI(3,4)P2, which is consistent with the estimate made above when vesicular trafficking is blocked by racH- mutant cells (Figures 22L and M).

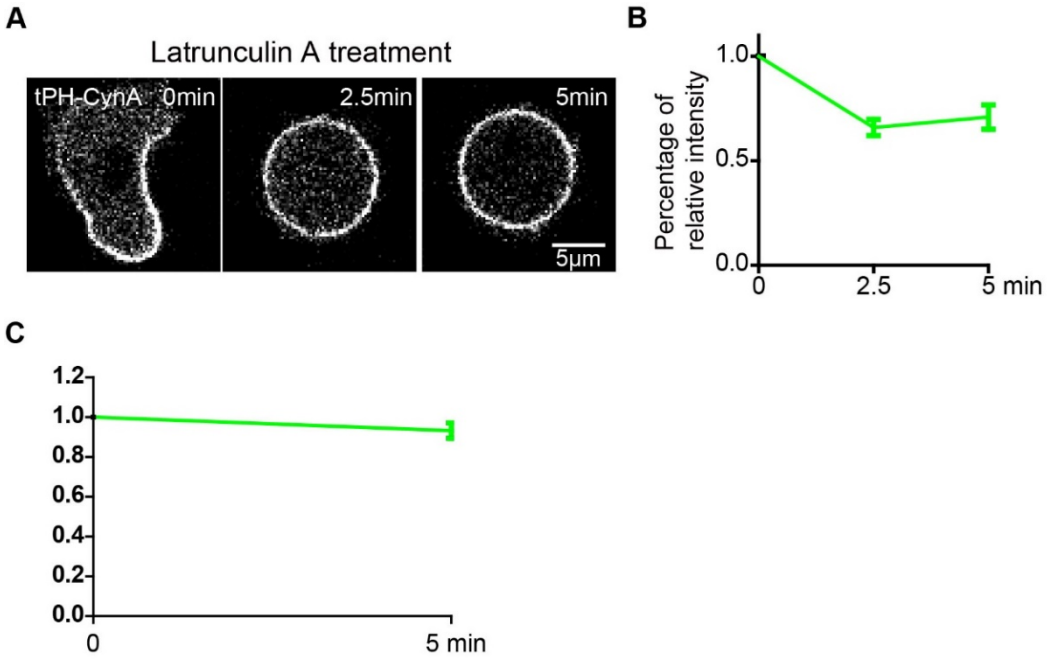

Figure 26. Temporal profile of PI(3,4)P2 on the membrane.
(A). Confocal fluorescent images of tPH-CynA-KikGR in *Dictyostelium* AX3 cell before and after Latrunculin A treatment were shown. Latrunculin A was added during images at time 0. (B). Temporal profile of normalized intensity of total fluorescence of tPH-CynA-KiKGR on the membrane of cells in (A) was shown (Mean ± SEM). (C). Small membrane region of Latrunculin A treated cells was photoconverted at time 0. Temporal profile of normalized intensity of total converted red fluorescence was shown (Mean ± SEM). The signal decreased by less than 8 percent in the first 5 minutes following photoconversion.

3.3.7 Dynamics of PI(3,4)P2 in human neutrophils

As PI(3,4)P2 is distributed to the back of migrating *Dictyostelium*, complementary to F-actin and active Ras (Figures 19A and B), we sought to investigate its spatio-temporal distribution in migrating human leukemia neutrophil-like HL-60 cells. In *Dictyostelium* cells, the two biosensors for PI(3,4)P2, tPH-CynA and PH-TAPP1, display slightly different patterns, despite the fact that they are identical on lipid strips and have preference to PI(3,4)P2. Li and Edwards et al. have previously established in *Dictyostelium* that tPH-CynA and PH-TAPP1 colocalize to the base of macropinocytic cups and back of the cell membrane (48, 144). However, while tPH-CynA labeled both structures strongly, the labelling of the back by PH-TAPP1 was relatively weaker (Figures 27A-C). In fixed cells with depleted cytosolic signal, the presence of PH-TAPP1 as a sharp band on the membrane at the back was detectable and colocalized with tPH-CynA (Figures 27D).

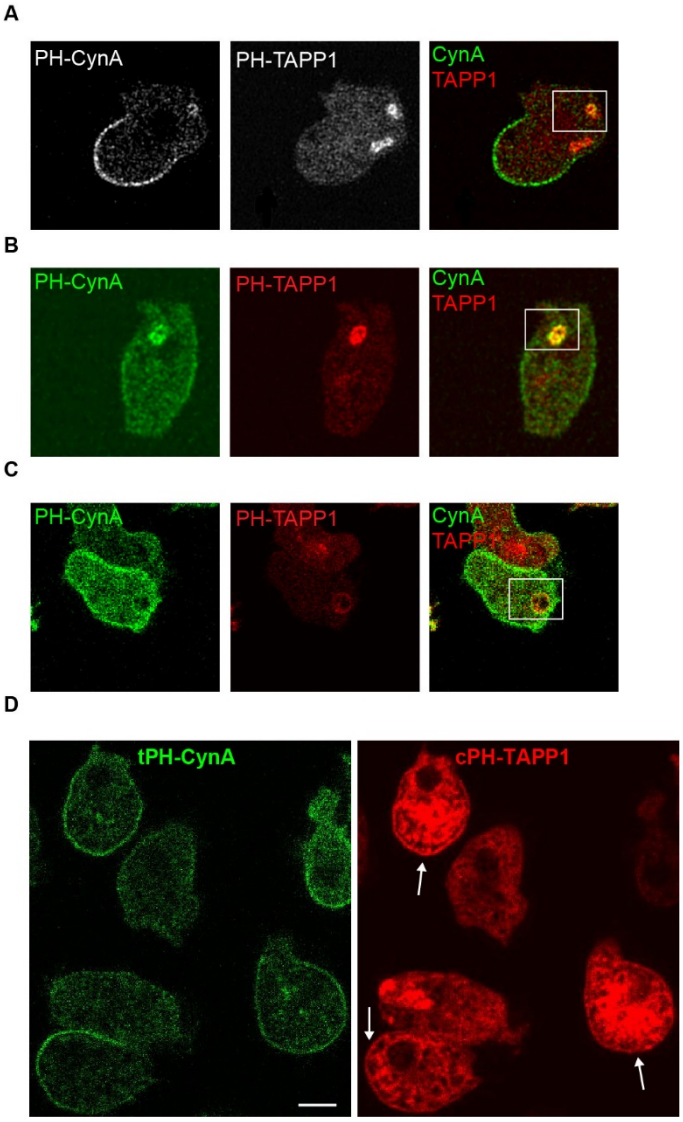

Figure 27. Comparison of PH-TAPP1 and tPH-CynA in *Dictyostelium*.
(A-C) Three examples of confocal images showing localization of PI(3,4)P2 (tPH-CynA-KiKGR; green) and cPH-TAPP1-RFP (red) in wild type *Dictyostelium* AX3 live cells. (D). Confocal images showing localization of PI(3,4)P2 (tPH-CynA-KiKGR ; green) and cPH-TAPP1 (red) in fixed wild type *Dictyostelium* AX3 cells.

Whereas tPH-CynA did not express in HL-60 cells, the distribution of PH-TAPP1 was similar in HL-60 cells and *Dictyostelium*. We used cPHX3-TAPP1-GFP, recently developed in the Hammond lab, as the biosensor for PI(3,4)P2 in HL-60 cells. We generated a stable HL-60 cell line expressing both RFP-LifeAct (another F-actin biosensor in human cells) and cPHX3TAPP1-GFP. Under live cell imaging, PI(3,4)P2 accumulated on the membrane, in a broad band at the front and a thin faint line at the back of migrating neutrophils (Figures 28A-

C). We further examined the distribution of PI(3,4)P2 in fixed HL-60 cells which have depleted cytosolic signal. Under these conditions, the presence of PI(3,4)P2 as a sharp band on the membrane at the back is clear (Figures 28D and E). Consistently, PI(3,4)P2 was found at the leading and trailing edges in zebrafish neutrophils (74).

Next, we looked for PI(3,4)P2-enriched vesicles using the cPHX3TAPP1-GFP biosensor in HL-60 cells. We observed an intracellular pool of PI(3,4)P2-enriched vesicles clustered towards the back of the neutrophils (Figures 28F and G). Some of these vesicles appeared very close to the membrane at the back and then disappear, suggesting that they might be fusing at the back of the membrane.

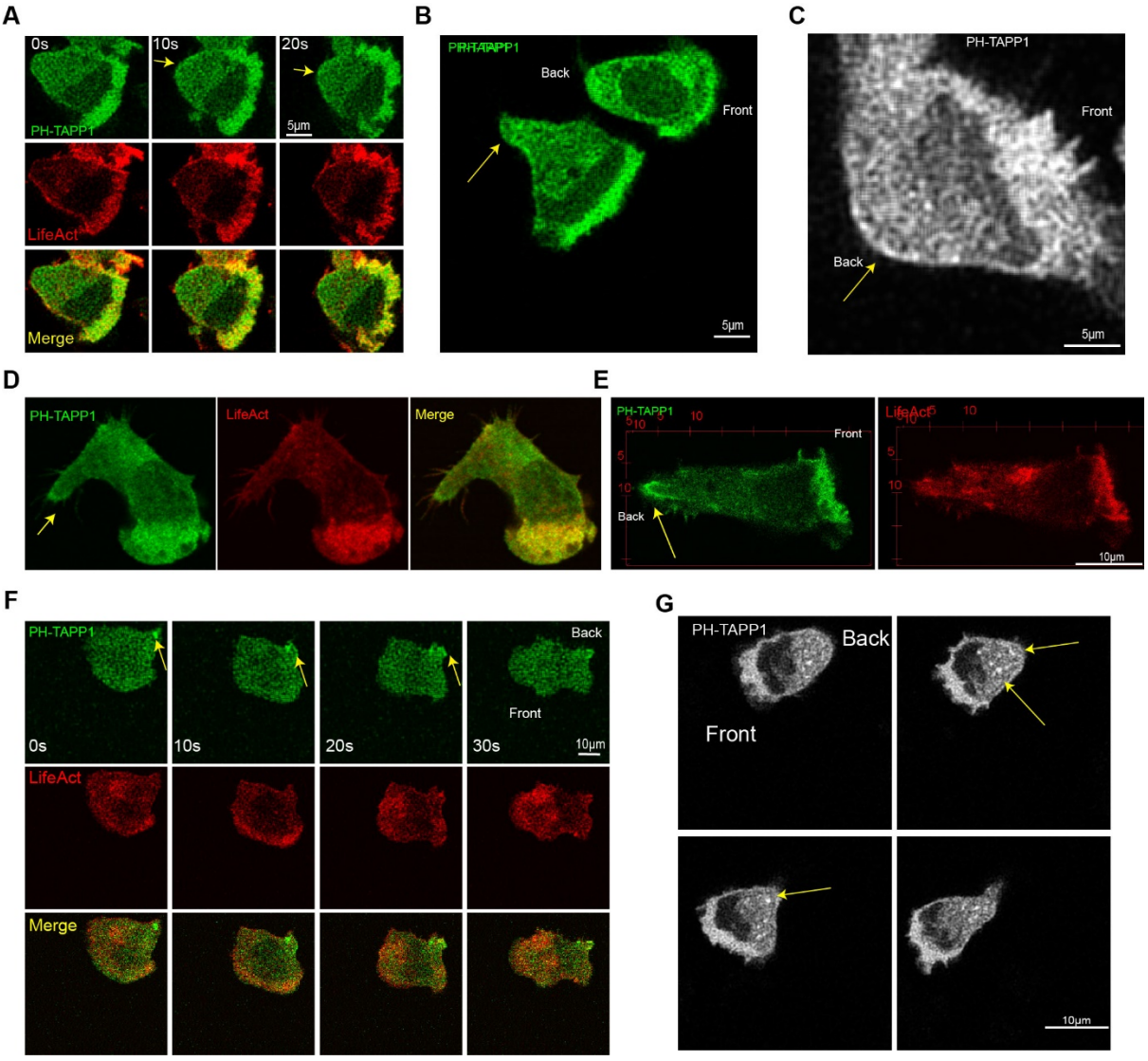

Figure 28. Dynamic localization of PI(3,4)P2 in neutrophils.
(A). Time-lapse confocal images of human leukemia neutrophil-like HL-60 cell line stably co-expressing PI(3,4)P2 biosensor, trimers of the isolated cPH (residues 169–329 in human TAPP1) (cPHx3TAPP1-GFP), and RFP-LifeAct (labelling F-actin) showing front and back localization of PI(3,4)P2. Yellow arrow points to PI(3,4)P2 localization at the back of the membrane. Front and back of the cell is shown. (B-C) Confocal images of HL-60 cell line stably co-expressing PI(3,4)P2 biosensor cPHx3TAPP1-GFP and RFP-LifeAct. Yellow arrow points to PI(3,4)P2 localization at the back of the membrane. Front and back of the cell are shown. (D). Confocal images showing front and back localization of PI(3,4)P2 in fixed HL-60 cells. Yellow arrow points to PI(3,4)P2 localization at the back of the membrane. (E). A maximum intensity projection of Z-stack of confocal images showing front and back localization of PI(3,4)P2 in fixed HL-60 cells. Yellow arrow points to PI(3,4)P2 localization at the back of the membrane.(F). Time-lapse confocal images of HL-60 cell co-expressing cPHx3TAPP1-GFP and RFP-LifeAct showing PI(3,4)P2 vesicles at the back of cells. Yellow arrow points to PI(3,4)P2 vesicle localization at the back of the HL-60 cell. (G). Time-lapse confocal images of HL-60 cell expressing cPHx3TAPP1-GFP showing PI(3,4)P2 vesicles at the back of cells. Yellow arrow points to some PI(3,4)P2 vesicles at the back of the HL-60 cell. Front and back of the cell are shown.

3.4 Discussion

All together, our studies can be summarized in the model shown in Figures 25E-G. Our previous study demonstrated the mutual inhibition between Ras activity and PI(3,4)P2 establishes polarity even in immobilized Latrunculin A treated cells in the presence of a chemoattractant gradient or caffeine (Figure 25E) (48, 103, 109). We now propose an additional mechanism involving a specific vesicle recycling path which sharpens the back-to-front gradient in migrating *Dictyostelium* cells. PI(3,4)P2 disappears from protrusions at the leading edges of macropinocytic cups, and then accumulates on the macropinosomes at the end of the internalization process. The macropinosomes are processed into smaller satellite PI(3,4)P2 tagged vesicles which then dock at the back. The PI(3,4)P2 molecules incorporated at the back diffuse along the membrane towards the front, where they are degraded (Figure 25F). In more polarized cells, owing to a slower arrival time of PI(3,4)P2 vesicles and a slower decay rate of PI(3,4)P2 on the membrane, the PI(3,4)P2 signal at the back broadens and extends further to the front (Figure 25G). Our results suggest that a similar mechanism could exist in polarized migrating mammalian cells.

Excitable network hypothesis and the formation of macropinocytic cups

This model is consistent with the excitable network hypothesis, which has been proposed to explain the behaviors of migrating cells (145). According to this hypothesis, propagating waves have an active region where front molecules are high and back molecules are low. This region is followed by a refractory region, where front molecules are very low and back components strongly accumulate (53, 59, 69). Here, our findings suggest macropinosomes are formed by a spreading wave whose trailing edge forms the base of the macropinocytic cups. This suggests that the base of the macropinocytic cups would be in a refractory state, which is heavily

decorated by the back molecule PI(3,4)P2. If PI(3,4)P2 is delivered to the back of the cell as we propose, it would shut off this region and further polarize the cell.

Many other signaling molecules such as PTEN, Myosin II, IQGAP1 and 2, cortexillin I and II, RasGAP2 (RG2) and RapGAP3 (RG3) localize to the back of the cells (47, 48, 146). Among those molecules, PTEN, RG2, RG3, and Myosin II are also reported to localize to the base of the cups or retracting protrusions. In addition, RG2 and RG3 bind to PI(3,4)P2 in vitro. Our results raise the possibility that the cells might be bringing the refractory state carrying many of those molecules from front to back.

Regulation of vesicle recycling controls polarity

In the reverse fountain flow model, we were proposing that vesicular trafficking plays an important role in polarity. Yet, the vesicle recycling mechanism we described is more obvious in less polarized cells. How can we explain this apparent discrepancy? Highly polarized cells are generally characterized by their typical elongated morphology, which is a result of having a larger proportion of the cell with elevated back markers. In fact, our simulations showed that the relatively longer arrival time of the vesicles and the slower decay rate increased the back region. Subsequently, experiment measurements did show a slower decay rate in highly polarized cells. Thus, both experimental data and simulation results are consistent in supporting the reverse fountain flow model (Figure 25).

PI(3,4)P2 is a distinct signaling component during cell migration

Our observations are consistent with an emerging view that PI(3,4)P2 is a signaling molecule on its own right, regulating cellular events (84). Numerous studies have shown PI(3,4)P2 localize to the leading/lagging edge during cell migration, early endosomes and lysosomes during clathrin-mediated endocytosis, and back of macropinocytic cups and early macropinosomes. This PI(3,4)P2 localization dynamics regulate all of these processes and there

appears to be a consistent pattern of PI(3,4)P2 localization involved in protrusion formation during cell migration and other aforementioned cellular events (79, 82, 147-149).

In some studies of cell motility and cytoskeletal events, PI(3,4)P2 acts as a negative regulator (150). Huttenlocher's group reported that Src-homology 2-containing inositol 5' phosphatase (SHIP) limits the motility of neutrophils and their recruitment to wounds in live zebrafish (75). Observations by Wu showed that PI(3,4)P2 defines the refractory period of the oscillation in cortical waves in mast cells (65, 87). Our lab reported that PI(3,4)P2 negatively regulates cell motility by inhibiting Ras activity, even in the absence of PIP3.

Our results depart from the canonical view that PI(3,4)P2 is only a byproduct of PIP3 hydrolysis (151). We demonstrated in mammalian neutrophils and in *Dictyostelium* cells that the level of PI(3,4)P2 was maintained on the plasma membrane under PI3K inhibition (Figures 21A-E). Additionally, in PI3K1-2- *Dictyostelium* cells, PI(3,4)P2 still accumulated on the membrane at the back of the cells and the macropinosomes (Figures 21F-I). This suggests that a fraction of PI(3,4)P2 must come from a source other than PIP3 and there is regulation of enzymes that generate PI(3,4)P2 from PI3P or PI4P. As there are multiple phosphoinositide kinases in *Dictyostelium* that have not been characterized, it is possible that one of these corresponds to a novel PI3K.

Endocytic trafficking of PI(3,4)P2 as a universal means of establishing polarity

Our current findings reveal that the PI(3,4)P2 decorated macropinosomes and its connection with PI(3,4)P2 gradient at the rear of the plasma membrane in regulating polarity during cell migration. Consistently, there are reports suggesting recycling of PI(3,4)P2 tagged vesicles and other endocytic events play an important role in polarity of epithelial cells. A study by the Bryant group recently described the function of PI(3,4)P2 in apical domain morphogenesis in MDCK cysts. Apical PI(3,4)P2 is supplied by the endosomal pool, rather than conversion from

basolateral PIP3 by SHIP1 and is a determinant of apical membrane identity (152). These observations reinforce the parallels between basolateral and apical surfaces of epithelial cells and front and back of migrating cells (153-155). Another parallel could be the establishment of polarity during cytokinesis, where PI(3,4)P2 is found elevated in the cleavage furrow (145). The potential role of vesicular trafficking in cytokinesis has not been investigated.

Reverse-fountain flow model of PI(3,4)P2

During migration, the additional membrane required to enable the expending protrusions could come from unfolding of invaginations of the membrane or from vesicular trafficking.

Multiple different studies have suggested that cells migrate following a fountain flow model: membrane precursor vesicles fuse with the anterior cell membrane at the protrusions, both the dorsal and ventral membranes flow toward the rear, and membrane is internalized at the rear (140, 156). In support of the fountain flow models, it has been shown that blocking of vesicular trafficking is required for movement, and that particles sticking on the outside of the cells as well as photobleached membrane patches flow from the front to the back.

In our reverse-fountain flow model, PI(3,4)P2-enriched vesicles are taken from macropinosomes at the anterior protrusion and eventually fuse to the membrane at the rear. Furthermore, plasma membrane PI(3,4)P2 at the rear diffuses towards the front. While this reverse-fountain flow model of PI(3,4)P2 sheds light on the role of this phospholipid in regulating polarity during cell migration, further study is needed to determine the direction of flow of other membrane components. One study showed that photoactivation of cAR1 did move towards the front, which support the reverse fountain flow model (Traynor & Kay, 2007). In addition, vesicles containing adenylyl cyclase fuse with the back of *Dictyostelium* cells and vesicles carrying growth factor receptor fuse at the back of cells (46, 157). A recent study by Moreau et al showed that migrating immature dendritic cells form macropinosomes at their

leading edge which traverse the cytoplasm and ultimately release their fluid content at the back (158). This agrees with our model. Membrane folding, fountain flow model or reverse fountain flow models may operate in specific cells during different migratory modes.

3.5 Methods

Cell Culture and differentiation

Wild-type *Dictyostelium discoideum* cells of AX3 and AX2 strains were used in this study. These strains are established lab cell lines because they can form fruiting bodies upon starvation and their morphology and behavior can be easily examined during chemotactic assays. *RacH*- strain, generated in AX2 background, was provided by Dr. Miho Iijima (JHU) and generated as described previously (142). All of these strains were cultured axenically in HL5 medium at 22 °C, either in suspension for obtaining high cell densities for cell differentiation or on tissue culture dishes for cell line maintenance. Cells expressing LimEΔcoil-RFP, PH-Crac-RFP, cPHx3-TAPP1-GFP, tPH-CynA-KikGR, PH_{CynA}-HALO or CAR1-KikGR constructs were generated by electroporation of the appropriate plasmids in wild-type or mutant cells. Transformed cells were selected and maintained in HL5 medium containing 20 μg/mL G418, 50 μg/mL Hygromycin B, or both. For microscopy, cells were plated in DB buffer to reduce HL5 medium-associated autofluorescence and photosensitivity of growing cells. This enabled prolonged and frequent imaging of cells.

Neutrophil-like HL-60 cells, used in this study, were procured from Dr. Orion Weiner (UCSF). Cells were grown in RPMI 1640 medium containing HEPES (ThermoFisher Scientific # 22400089) and heat-inactivated fetal bovine serum (10% v/v; Gibco). Cultures were maintained at a density of 0.1–1.0 million cells/ml at 37°C/5% CO_2. Differentiated HL-60s were obtained by adding 1.5% (vol/vol) DMSO (Sigma-Aldrich) to actively growing cells (at a density of 0.3 million cells/ml) followed by incubation for an additional 5-6 days (159).

Human embryonic kidney 293 (HEK293T) cells were used to generate lentivirus to perform lentivirus transduction in HL-60 cells. HEK293T cells were grown in DMEM (Mediatech)

containing 10% (vol/vol) heat-inactivated fetal bovine serum and maintained at 37°C/5% CO_2.

Plasmid Construction

cPHx3$_{TAPP1}$-GFP and pPamCherry1-C1-TAPP1-cPHx3 was provided by Gerald R.V. Hammond (Pitt) and Brady D. Goulden (144). It was subsequently cloned into pDM358 vector or SFFV vector. RFP-LifeAct was obtained from Stephen Desiderio Lab (JHU) and was subsequently cloned into SFFV vector (Addgene Cat # 79121). LimEΔcoil-RFP, cPH-TAPP1-RFP, PH-Crac-RFP and tPH-CynA-KikGR constructs were created in previous studies (48). C-terminal HALO-tagged PH$_{CynA}$ construct was generated by cloning the PH$_{CynA}$ ORF from tPH-CynA-KikGRk-KF2 construct using the primers 5' Fwd; TATAAGATCTAAAAAAATGAAATCCTCAAATGGTGTCGGTTGTAC and 3' Rev; TATAACTAGTTGAAATTGGTTTTGGCGGAAGAGGAG into BglII/SpeI sites of pHK12neo plasmid.

Lentivirus transduction of HL-60 cells

HEK293T cells were seeded into six-well plates and grown until 80% confluent. For each well, 5 μg cPHx3$_{TAPP1}$-GFP in SFFV vector,1.25 μg VSVG, and 3.5 μg cytomegalovirus 8.91 vector were mixed and prepared for transfection using Lipofectamine® 3000 following manufacturer's instructions. After transfection, cells were grown for an additional 1-3 days, after which virus-containing supernatants were harvested. 50-200 uL virus was mixed with 1 million HL-60 cells in growth medium supplemented with polybrene (8 μg/ml), and incubated overnight. HL-60 cells expressing cPHx3$_{TAPP1}$-GFP or RFP-LifeAct were selected by FACS after 5 days.

Microscopy

Growth-phase *Dictyostelium* or differentiated HL-60 cells were placed on uncoated or fibronectin-coated eight-well coverslip chamber slide (Lab-Tek, Thermo Scientific, Nunc). Confocal imaging was performed with the help of a Zeiss LSM780 single-point laser-scanning microscope. Time-lapse images were obtained with DIC, GFP, or RFP illumination at 3- to 25-s intervals for 20-180 min.

Confocal microscopy with FM4-64. *Dictyostelium* cells were pretreated with 0.1 M sorbitol in PB to reduce formation of contractile vacuoles, which tend to get extensively labeled with FM4-64 dye (160). 2 μM FM4-64 was added to cells during the live cell imaging.

Confocal microscopy with Photoconversion. Cells expressing tPH-CynA-KikGR were visualized using a 488 nm Argon laser and a 40X objective. For photoconversion of KikGR, a 405 nm diode laser was used with 1x5 iterations. Furthermore, a region of interest was moved to the center of the viewing field, and the field diaphragm was closed to its smallest opening to make a photoconvertible spot using a 541 nm laser for red fluorescence excitation. Imaging of both photoconverted and unconverted KikGR was done using 488 nm Ag laser for green fluorescence and 541 nm laser for red fluorescence in multi-track mode.

Fluorescence recovery after photobleaching (FRAP). To minimize the contribution of diffusion from above and below the bleach box, the box was expanded to include a portion of the top and bottom membranes. A section of the cell periphery in zoom was exposed to two iterations of saturating 488-nm laser light causing a partial bleach.

PH_{CynA}-HALO labelling and imaging using HaloTag® TMR Ligand. PH-CynA-Halo expressing *Dictyostelium* cells were harvested, washed in DB, and incubated with 3 μM TMR conjugated HaloTag ligand (Promega) for 30 mins at RT. Excess stain was washed away using DB, and cells were imaged using the Zeiss LSM780 confocal microscope.

Cell fixation. Growth stage *Dictyostelium* cells were allowed to attach to cover-glass for 30min to 2 hours in an eight-well chamber slide. Cells were incubated with freshly made fixative (2% buffered paraformaldehyde, 0.25% glutaraldehyde, and 0.1% Triton X-100 in HL5) for 10 minutes at room temperature, and subsequently quenched in 1mg/mL sodium borohydride for 3 minutes. Cells were then washed twice with TBS (supplemented with 0.25% BSA and 0.05% Triton X-100) and visualized using the Zeiss LSM780 confocal microscope. In each experiment, images from different samples were taken consecutively using identical settings.

Cell fusion by electroporation

Growth phase tPH-CynA-KikGR expressing *Dictyostelium* cells were grown in suspension, harvested, washed, and resuspended in SB (17 mM Soerensen buffer containing 15 mM KH2PO4 and 2 mM Na2HPO4, pH 6.0) at a density of 15 million cells/ml. 10 ml of cells were rolled gently for 20-45 min. 800 µl of rolled cells were transferred to a 4-mm-gap electroporation cuvette. Electroporation was carried out with the following settings: 1,000 V, 3 µF for once, and 1,000 V, 1 µF for three times, with 1–2 s between pulses. 50 µl of cells were then transferred to the center of a well in an 8-well chamber, and was allowed to adhere for 10 min. 450 µl of SB (containing 2 mM CaCl2 and 2 mM MgCl2) was added to the well, and was pipetted gently to resuspend the cells evenly. Unadhered cells were removed by washing with 450 µl of fresh SB, after which the attached cells were incubated for 1 h for recovery before imaging(55).

Computational Study

In this present study we modeled the cell membrane as a 1D spatial domain of length 40 µm with periodic boundary condition. The arrival of the satellite vesicles on the membrane was modeled as a discrete Poisson process with a variable mean arrival time – (a) for the vegetative

cell: λ_{veg} = 10 s, (b) for the developed cell: λ_{dev} = 40 s. We assumed two separate pools of PI(3,4)P2 molecules: PI(3,4)P2 on the docked vesicle (U) and on the membrane (V). For the purpose of modeling we simplified the process of vesicle fusion as follows:

(a) At a randomly chosen time instant t_a ($t_a \sim$ chosen with an exponential distribution with mean arrival time λ), n ($n \sim$ Normal distribution) molecules of U per unit length (i.e. $n \times r$ total molecules where r is the radius of the vesicle) appeared on the membrane centered around a docking site, x_d. The docking site, x_d, is randomly selected sampled either from a probability distribution with the cumulative density function, $F_V(l) = \sum_{k=0}^{l} v_k^{n_v}$ where v_k is the value of V at spatial index k (directed insertion case) or from a discrete uniform distribution (random insertion case).

(b) During the docking time interval, Δt_{dock}, U remained unchanged.

(c) After Δt_{dock}, U converted to V which diffuses freely on the membrane.

The mathematical description of the model is given as follows:

$$\frac{\partial \mathrm{U}}{\partial \mathrm{t}} = \delta_{(\mathrm{x,t})}(\mathrm{x_d}, \mathrm{t_a}) - \mathrm{k_{-u}}\left(1 - \mathbb{I}_{\Delta \mathrm{t_{dock}}}(\mathrm{t})\right)\mathrm{U}$$

$$\frac{\partial \mathrm{V}}{\partial \mathrm{t}} = \mathrm{k_{-u}}\left(1 - \mathbb{I}_{\Delta \mathrm{t_{dock}}}(\mathrm{t})\right)\mathrm{U} - \mathrm{d}\big(\mathrm{x}, \mathrm{V}(\mathrm{x,t})\big)\mathrm{V} + \mathrm{D_V}\nabla^2\mathrm{V}$$

where, $\mathbb{I}_{\Delta \mathrm{t_{dock}}}$ and $\delta_{(x,t)}(x_d, t_a)$ are, respectively, the indicator and Kronecker delta functions defined as follows:

$$\mathbb{I}_{\mathrm{t_{dock}}}(t) = \begin{cases} 1, & \text{if } t \in \Delta \mathrm{t_{dock}} \\ 0, & \text{if } t \notin \Delta \mathrm{t_{dock}} \end{cases}$$

$$\delta_{(x,t)}(x_d, t_a) = \begin{cases} 1, & \text{if } x \in x_d, t = t_a \\ 0, & \text{if } x \notin x_d, t \neq t_a \end{cases}$$

The Kronecker delta function models the arrival of a vesicle at a particular site and the indicator function restricts the fusion of U (the PI(3,4)P2 on the vesicle to the membrane) until the end of the docking period. The following decay function, $d(\cdot)$ was used:

$$\mathrm{d}\big(x, \mathrm{V}(x,t)\big) = k_1 + k_2 \frac{1}{k_3 + \mathrm{V}(x,t)^2}$$

Whereas the first part of the decay function denotes a spatially independent basal decay rate, the second part represents the effect of spatially variable decay rate as observed experimentally (the skewed distribution of the photoconverted red fluorescent profile validated this assumption).

The stochastic simulations of the model were performed using URDME(161) approach using custom code written in MATLAB 2019b (MathWorks, Natick, MA, USA). The simulation domain was considered as a 1D domain of length 40 μm with spatial grid resolution of 0.1 μm. The completely unpolarized cell membrane ((U,V) = (0,0)) was taken as the initial condition.

For the estimation of the diffusion constant in Figure 19D, a simple diffusion model was simulated using the URDME as explained above using the converted red fluorescence profile at 0 sec as the initial condition. The optimum diffusion coefficient was obtained by minimizing the following cost function:

$$\sum_k \left[V_{exp}(x,t_k) - V_{sim}(x,t_k)\right]^2$$

Quantification and Statistical Analysis

Image Analysis

All images were processed using Fiji (like ImageJ) (National Institutes of Health) and MATLAB. The mean intensity of the membrane portion and cytosol portion were measured,

and the ratio was calculated using image J as described previously(48). Cells were segmented by a multistep process using commands from the Image Processing Toolbox in MATLAB. Colors were assigned linearly in the same fashion across all kymographs, with blue indicating the lowest intensity and red the highest intensity. Biosensor patches were defined regions of fluorescent intensity that are two folds over background.

Statistical Analysis

Mean values and standard deviations/ standard error of the mean were calculated and used to assess differences between two groups by GraphPad Prism. P-values ≤ 0.05 were considered statistically significant, throughout this study. Images presented in figures are representative of more than three independent experiments.

3.6 Author contributions

X.L. designed and performed a majority of experiments; D.S.P. performed *RacH* mutant experiments, and generated PH-CynA-HALO construct; D.B and P.A.I conducted computational simulations. P.N.D supervised the project.

Chapter 4

Conclusion

Cell migration requires coordination of signal transduction and cytoskeletal events, which regulate the dynamics and localization of cellular protrusions and contractions. The behavior of the signal transduction and the cytoskeleton networks suggest that they are excitable and has led to the "excitable network hypothesis" for cell migration. In migrating *Dictyostelium* cells, waves of Ras and PI3K activation, propagate along the cell cortex, while back protein, PTEN, dissociates from the membrane generating coordinated "shadow" waves. Theoretical models of excitability involve activator-inhibitor feedback loops, and the molecular events comprising the loops provide a novel framework for understanding the behaviors of migrating cells.

In my thesis we revealed a complete description of a mutual inhibitory feedback loop between Ras activation and PI(3,4)P2 that is central for cell migration. We show that chemoattractants, which activate Ras, lead to a reduction of PI(3,4)P2. Since RG2 binds to PI(3,4)P2, its dissociation from the membrane leads to a further increase in Ras activity, which in turn further decreases PI(3,4)P2, creating a powerful positive feedback loop (Figure 18F and G). There is a similar loop involving RG3. This is consistent with our observations of the patterns of Ras and Rap activities and PI(3,4)P2 in migrating cells and the phenotypes resulting from perturbations.

The mutual inhibition between Ras activity and PI(3,4)P2 establishes polarity even in immobilized Latrunculin A treated cells in the presence of a chemoattractant gradient. We next proposed an additional mechanism involving a specific vesicle recycling path which sharpens the back-to-front gradient in migrating *Dictyostelium* cells. This "reverse fountain flow" of PI(3,4)P2 regulates polarity in cell migration: First appearing on macropinosomes derived from protrusions, it is delivered to the back on small vesicles and then diffuses to the front. A resulting back-to-front gradient contributes to polarity during cell migration. This model is consistent with the excitable network hypothesis, which has been proposed to explain the behaviors of migrating cells. According to this hypothesis, propagating waves have an active region where front molecules are high and back molecules are low. This region is followed by a refractory region, where front molecules are very low and back components strongly accumulate (53, 59, 69, 145). Here, our findings suggest macropinosomes are formed by a spreading wave whose trailing edge forms the base of the macropinocytic cups. This suggests that the base of the macropinocytic cups would be in a refractory state, which is heavily decorated by the back molecule PI(3,4)P2. If PI(3,4)P2 is delivered to the back of the cell as we propose, it would shut off this region and further polarize the cell. Our results raise the possibility that the cells might be bringing the refractory state carrying many of those molecules from front to back.

The discovery of these positive feedback loops provides critical insight to molecular mechanisms of excitability. The excitable network hypothesis for cell migration may provide a novel framework for understanding morphological changes in cells. In this thesis, we described a complete feedback loop between Ras and PI(3,4)P2 that mediates cell migration, and showed that the vesicular trafficking of PI(3,4)P2 plays an important role in polarity in cell migration. Going forward, it will be important to determine how are PI(3,4)P2 degraded from

the front of the membrane and the motor proteins that transport PI(3,4)P2 during recycling, and the extent to which the same or similar excitable networks are used in migrating cells in developing embryos as have been elaborated for *Dictyostelium* and several mammalian cells lines.

Bibliography

1. Miller LD, Russell MH, & Alexandre G (2009) Diversity in bacterial chemotactic responses and niche adaptation. *Adv Appl Microbiol* 66:53-75.
2. Swaney KF, Huang CH, & Devreotes PN (2010) Eukaryotic chemotaxis: a network of signaling pathways controls motility, directional sensing, and polarity. *Annu Rev Biophys* 39:265-289.
3. Matilla MA & Krell T (2018) The effect of bacterial chemotaxis on host infection and pathogenicity. *FEMS Microbiol Rev* 42(1).
4. Zhao M*, et al.* (2006) Electrical signals control wound healing through phosphatidylinositol-3-OH kinase-gamma and PTEN. *Nature* 442(7101):457-460.
5. Cortese B, Palama IE, D'Amone S, & Gigli G (2014) Influence of electrotaxis on cell behaviour. *Integr Biol (Camb)* 6(9):817-830.
6. Lo CM, Wang HB, Dembo M, & Wang YL (2000) Cell movement is guided by the rigidity of the substrate. *Biophys J* 79(1):144-152.
7. Whitaker BD & Poff KL (1980) Thermal adaptation of thermosensing and negative thermotaxis in *Dictyostelium*. *Exp Cell Res* 128(1):87-93.
8. Nabeshima K, Kataoka H, & Koono M (1986) Enhanced migration of tumor cells in response to collagen degradation products and tumor cell collagenolytic activity. *Invasion Metastasis* 6(5):270-286.
9. Harland B, Walcott S, & Sun SX (2011) Adhesion dynamics and durotaxis in migrating cells. *Phys Biol* 8(1):015011.
10. Artemenko Y, Axiotakis L, Jr., Borleis J, Iglesias PA, & Devreotes PN (2016) Chemical and mechanical stimuli act on common signal transduction and cytoskeletal networks. *Proc Natl Acad Sci U S A* 113(47):E7500-E7509.

11. Blaser H*, et al.* (2006) Migration of zebrafish primordial germ cells: a role for myosin contraction and cytoplasmic flow. *Dev Cell* 11(5):613-627.

12. Keller R (2005) Cell migration during gastrulation. *Curr Opin Cell Biol* 17(5):533-541.

13. Theveneau E & Mayor R (2012) Neural crest delamination and migration: from epithelium-to-mesenchyme transition to collective cell migration. *Dev Biol* 366(1):34-54.

14. Shaw TJ & Martin P (2009) Wound repair at a glance. *J Cell Sci* 122(Pt 18):3209-3213.

15. Richardson BE & Lehmann R (2010) Mechanisms guiding primordial germ cell migration: strategies from different organisms. *Nat Rev Mol Cell Biol* 11(1):37-49.

16. Wright DE, Wagers AJ, Gulati AP, Johnson FL, & Weissman IL (2001) Physiological migration of hematopoietic stem and progenitor cells. *Science* 294(5548):1933-1936.

17. Morisawa M & Yoshida M (2005) Activation of motility and chemotaxis in the spermatozoa: From invertebrates to humans. *Reprod Med Biol* 4(2):101-114.

18. Friedl P & Gilmour D (2009) Collective cell migration in morphogenesis, regeneration and cancer. *Nat Rev Mol Cell Biol* 10(7):445-457.

19. Baumann K (2014) Stem cells: moving out of the niche. *Nat Rev Mol Cell Biol* 15(2):79.

20. Lakshman R & Finn A (2001) Neutrophil disorders and their management. *J Clin Pathol* 54(1):7-19.

21. Friedl P & Alexander S (2011) Cancer invasion and the microenvironment: plasticity and reciprocity. *Cell* 147(5):992-1009.

22. Mitchell DR (2007) The evolution of eukaryotic cilia and flagella as motile and sensory organelles. *Adv Exp Med Biol* 607:130-140.

23. King JS & Kay RR (2019) The origins and evolution of macropinocytosis. *Philos Trans R Soc Lond B Biol Sci* 374(1765):20180158.

24. Lenaghan SC, Nwandu-Vincent S, Reese BE, & Zhang M (2014) Unlocking the secrets of multi-flagellated propulsion: drawing insights from Tritrichomonas foetus. *J R Soc Interface* 11(93):20131149.

25. Alexandre G (2015) Chemotaxis Control of Transient Cell Aggregation. *J Bacteriol* 197(20):3230-3237.

26. Van Haastert PJ (2010) Chemotaxis: insights from the extending pseudopod. *J Cell Sci* 123(Pt 18):3031-3037.

27. Francis EA & Heinrich V (2018) Extension of chemotactic pseudopods by nonadherent human neutrophils does not require or cause calcium bursts. *Sci Signal* 11(521).

28. Wolf K*, et al.* (2003) Compensation mechanism in tumor cell migration: mesenchymal-amoeboid transition after blocking of pericellular proteolysis. *J Cell Biol* 160(2):267-277.

29. Tyson RA, Zatulovskiy E, Kay RR, & Bretschneider T (2014) How blebs and pseudopods cooperate during chemotaxis. *Proc Natl Acad Sci U S A* 111(32):11703-11708.

30. Barnhart EL, Allen GM, Julicher F, & Theriot JA (2010) Bipedal locomotion in crawling cells. *Biophys J* 98(6):933-942.

31. Keren K*, et al.* (2008) Mechanism of shape determination in motile cells. *Nature* 453(7194):475-480.

32. Mejillano MR*, et al.* (2004) Lamellipodial versus filopodial mode of the actin nanomachinery: pivotal role of the filament barbed end. *Cell* 118(3):363-373.

33. Sixt M (2012) Cell migration: fibroblasts find a new way to get ahead. *J Cell Biol* 197(3):347-349.

34. Hou Y, Hedberg S, & Schneider IC (2012) Differences in adhesion and protrusion properties correlate with differences in migration speed under EGF stimulation. *BMC Biophys* 5:8.

35. Murphy DA & Courtneidge SA (2011) The 'ins' and 'outs' of podosomes and invadopodia: characteristics, formation and function. *Nat Rev Mol Cell Biol* 12(7):413-426.

36. Linder S, Nelson D, Weiss M, & Aepfelbacher M (1999) Wiskott-Aldrich syndrome protein regulates podosomes in primary human macrophages. *Proc Natl Acad Sci U S A* 96(17):9648-9653.

37. Roignot J, Peng X, & Mostov K (2013) Polarity in mammalian epithelial morphogenesis. *Cold Spring Harb Perspect Biol* 5(2).

38. Martin-Belmonte F & Perez-Moreno M (2011) Epithelial cell polarity, stem cells and cancer. *Nat Rev Cancer* 12(1):23-38.

39. Dai W & Montell DJ (2016) Live Imaging of Border Cell Migration in Drosophila. *Methods Mol Biol* 1407:153-168.

40. Bianco A*, et al.* (2007) Two distinct modes of guidance signalling during collective migration of border cells. *Nature* 448(7151):362-365.

41. Haas P & Gilmour D (2006) Chemokine signaling mediates self-organizing tissue migration in the zebrafish lateral line. *Dev Cell* 10(5):673-680.

42. West-Foyle H & Robinson DN (2012) Cytokinesis mechanics and mechanosensing. *Cytoskeleton (Hoboken)* 69(10):700-709.

43. Falnikar A & Baas PW (2013) Neuronal migration re-purposes mechanisms of cytokinesis. *Cell Cycle* 12(23):3577-3578.

44. Devreotes PN, *et al.* (2017) Excitable Signal Transduction Networks in Directed Cell Migration. *Annu Rev Cell Dev Biol* 33:103-125.

45. Parent CA (2004) Making all the right moves: chemotaxis in neutrophils and *Dictyostelium*. *Curr Opin Cell Biol* 16(1):4-13.

46. Kriebel PW, Barr VA, Rericha EC, Zhang G, & Parent CA (2008) Collective cell migration requires vesicular trafficking for chemoattractant delivery at the trailing edge. *J Cell Biol* 183(5):949-961.

47. Li X, Miao Y, Pal DS, & Devreotes PN (2019) Excitable networks controlling cell migration during development and disease. *Semin Cell Dev Biol*.

48. Li X, *et al.* (2018) Mutually inhibitory Ras-PI(3,4)P2 feedback loops mediate cell migration. *Proc Natl Acad Sci U S A* 115(39):E9125-E9134.

49. Veltman DM, *et al.* (2016) A plasma membrane template for macropinocytic cups. *Elife* 5.

50. Janetopoulos C, Borleis J, Vazquez F, Iijima M, & Devreotes P (2005) Temporal and spatial regulation of phosphoinositide signaling mediates cytokinesis. *Dev Cell* 8(4):467-477.

51. Shewan A, Eastburn DJ, & Mostov K (2011) Phosphoinositides in cell architecture. *Cold Spring Harb Perspect Biol* 3(8):a004796.

52. Gerisch G, Schroth-Diez B, Muller-Taubenberger A, & Ecke M (2012) PIP3 waves and PTEN dynamics in the emergence of cell polarity. *Biophys J* 103(6):1170-1178.

53. Huang CH, Tang M, Shi C, Iglesias PA, & Devreotes PN (2013) An excitable signal integrator couples to an idling cytoskeletal oscillator to drive cell migration. *Nat Cell Biol* 15(11):1307-1316.

54. Muller-Taubenberger A, Kortholt A, & Eichinger L (2013) Simple system--substantial share: the use of *Dictyostelium* in cell biology and molecular medicine. *Eur J Cell Biol* 92(2):45-53.

55. Miao Y*, et al.* (2019) Wave patterns organize cellular protrusions and control cortical dynamics. *Mol Syst Biol* 15(3):e8585.

56. Blanchoin L*, et al.* (2000) Direct observation of dendritic actin filament networks nucleated by Arp2/3 complex and WASP/Scar proteins. *Nature* 404(6781):1007-1011.

57. Yang C*, et al.* (2007) Novel roles of formin mDia2 in lamellipodia and filopodia formation in motile cells. *PLoS Biol* 5(11):e317.

58. Bailly M*, et al.* (2001) The F-actin side binding activity of the Arp2/3 complex is essential for actin nucleation and lamellipod extension. *Curr Biol* 11(8):620-625.

59. Tang M*, et al.* (2014) Evolutionarily conserved coupling of adaptive and excitable networks mediates eukaryotic chemotaxis. *Nat Commun* 5:5175.

60. Gerhardt M*, et al.* (2014) Actin and PIP3 waves in giant cells reveal the inherent length scale of an excited state. *J Cell Sci* 127(Pt 20):4507-4517.

61. Weiner OD, Marganski WA, Wu LF, Altschuler SJ, & Kirschner MW (2007) An actin-based wave generator organizes cell motility. *PLoS Biol* 5(9):e221.

62. Hepper I*, et al.* (2012) The mammalian actin-binding protein 1 is critical for spreading and intraluminal crawling of neutrophils under flow conditions. *J Immunol* 188(9):4590-4601.

63. Masters TA, Sheetz MP, & Gauthier NC (2016) F-actin waves, actin cortex disassembly and focal exocytosis driven by actin-phosphoinositide positive feedback. *Cytoskeleton (Hoboken)* 73(4):180-196.

64. Wu M, Wu X, & De Camilli P (2013) Calcium oscillations-coupled conversion of actin travelling waves to standing oscillations. *Proc Natl Acad Sci U S A* 110(4):1339-1344.

65. Xiong D*, et al.* (2016) Frequency and amplitude control of cortical oscillations by phosphoinositide waves. *Nat Chem Biol* 12(3):159-166.

66. Colin-York H*, et al.* (2019) Cytoskeletal actin patterns shape mast cell activation. *Commun Biol* 2:93.

67. Andrew N & Insall RH (2007) Chemotaxis in shallow gradients is mediated independently of PtdIns 3-kinase by biased choices between random protrusions. *Nat Cell Biol* 9(2):193-200.

68. Van Haastert PJ (2010) A stochastic model for chemotaxis based on the ordered extension of pseudopods. *Biophys J* 99(10):3345-3354.

69. Xiong Y, Huang CH, Iglesias PA, & Devreotes PN (2010) Cells navigate with a local-excitation, global-inhibition-biased excitable network. *Proc Natl Acad Sci U S A* 107(40):17079-17086.

70. Iglesias PA & Devreotes PN (2012) Biased excitable networks: how cells direct motion in response to gradients. *Curr Opin Cell Biol* 24(2):245-253.

71. Hawkins PT & Stephens LR (2016) Emerging evidence of signalling roles for PI(3,4)P2 in Class I and II PI3K-regulated pathways. *Biochem Soc Trans* 44(1):307-314.

72. Ramos AR, Elong Edimo W, & Erneux C (2018) Phosphoinositide 5-phosphatase activities control cell motility in glioblastoma: Two phosphoinositides PI(4,5)P2 and PI(3,4)P2 are involved. *Adv Biol Regul* 67:40-48.

73. Fukumoto M, Ijuin T, & Takenawa T (2017) PI(3,4)P2 plays critical roles in the regulation of focal adhesion dynamics of MDA-MB-231 breast cancer cells. *Cancer Sci* 108(5):941-951.

74. Lam PY, Yoo SK, Green JM, & Huttenlocher A (2012) The SH2-domain-containing inositol 5-phosphatase (SHIP) limits the motility of neutrophils and their recruitment to wounds in zebrafish. *J Cell Sci* 125(Pt 21):4973-4978.

75. Yoo SK, *et al.* (2010) Differential regulation of protrusion and polarity by PI3K during neutrophil motility in live zebrafish. *Dev Cell* 18(2):226-236.

76. Li H, *et al.* (2016) Phosphatidylinositol-3,4-Bisphosphate and Its Binding Protein Lamellipodin Regulate Chemotaxis of Malignant B Lymphocytes. *J Immunol* 196(2):586-595.

77. Wallroth A & Haucke V (2018) Phosphoinositide conversion in endocytosis and the endolysosomal system. *J Biol Chem* 293(5):1526-1535.

78. Watt SA, *et al.* (2004) Detection of novel intracellular agonist responsive pools of phosphatidylinositol 3,4-bisphosphate using the TAPP1 pleckstrin homology domain in immunoelectron microscopy. *Biochem J* 377(Pt 3):653-663.

79. Posor Y, *et al.* (2013) Spatiotemporal control of endocytosis by phosphatidylinositol-3,4-bisphosphate. *Nature* 499(7457):233-237.

80. Posor Y, Eichhorn-Grunig M, & Haucke V (2015) Phosphoinositides in endocytosis. *Biochim Biophys Acta* 1851(6):794-804.

81. Valenzuela-Iglesias A, *et al.* (2015) Profilin1 regulates invadopodium maturation in human breast cancer cells. *Eur J Cell Biol* 94(2):78-89.

82. Maekawa M, *et al.* (2014) Sequential breakdown of 3-phosphorylated phosphoinositides is essential for the completion of macropinocytosis. *Proc Natl Acad Sci U S A* 111(11):E978-987.

83. Dormann D, Weijer G, Dowler S, & Weijer CJ (2004) In vivo analysis of 3-phosphoinositide dynamics during *Dictyostelium* phagocytosis and chemotaxis. *J Cell Sci* 117(Pt 26):6497-6509.

84. Li H & Marshall AJ (2015) Phosphatidylinositol (3,4) bisphosphate-specific phosphatases and effector proteins: A distinct branch of PI3K signaling. *Cell Signal* 27(9):1789-1798.

85. Erneux C, Edimo WE, Deneubourg L, & Pirson I (2011) SHIP2 multiple functions: a balance between a negative control of PtdIns(3,4,5)P(3) level, a positive control of PtdIns(3,4)P(2) production, and intrinsic docking properties. *J Cell Biochem* 112(9):2203-2209.

86. Franke TF, Kaplan DR, Cantley LC, & Toker A (1997) Direct regulation of the Akt proto-oncogene product by phosphatidylinositol-3,4-bisphosphate. *Science* 275(5300):665-668.

87. Yang Y, Xiong D, Pipathsouk A, Weiner OD, & Wu M (2017) Clathrin Assembly Defines the Onset and Geometry of Cortical Patterning. *Dev Cell* 43(4):507-521 e504.

88. Zhang SX, Duan LH, He SJ, Zhuang GF, & Yu X (2017) Phosphatidylinositol 3,4-bisphosphate regulates neurite initiation and dendrite morphogenesis via actin aggregation. *Cell Res* 27(2):253-273.

89. Marat AL*, et al.* (2017) mTORC1 activity repression by late endosomal phosphatidylinositol 3,4-bisphosphate. *Science* 356(6341):968-972.

90. Rohacs T*, et al.* (2003) Specificity of activation by phosphoinositides determines lipid regulation of Kir channels. *Proc Natl Acad Sci U S A* 100(2):745-750.

91. Yamaguchi S*, et al.* (2014) Potential role of voltage-sensing phosphatases in regulation of cell structure through the production of PI(3,4)P2. *J Cell Physiol* 229(4):422-433.

92. Jayachandran N, *et al.* (2018) TAPP Adaptors Control B Cell Metabolism by Modulating the Phosphatidylinositol 3-Kinase Signaling Pathway: A Novel Regulatory Circuit Preventing Autoimmunity. *J Immunol* 201(2):406-416.

93. Oikawa T & Takenawa T (2009) PtdIns(3,4)P2 instigates focal adhesions to generate podosomes. *Cell Adh Migr* 3(2):195-197.

94. Loovers HM, *et al.* (2007) Regulation of phagocytosis in *Dictyostelium* by the inositol 5-phosphatase OCRL homolog Dd5P4. *Traffic* 8(5):618-628.

95. Sauer K, *et al.* (2013) Inositol tetrakisphosphate limits NK cell effector functions by controlling PI3K signaling. *Blood* 121(2):286-297.

96. Kamimura Y, *et al.* (2008) PIP3-independent activation of TorC2 and PKB at the cell's leading edge mediates chemotaxis. *Curr Biol* 18(14):1034-1043.

97. Charest PG, *et al.* (2010) A Ras signaling complex controls the RasC-TORC2 pathway and directed cell migration. *Dev Cell* 18(5):737-749.

98. Weiner OD, *et al.* (2002) A PtdInsP(3)- and Rho GTPase-mediated positive feedback loop regulates neutrophil polarity. *Nat Cell Biol* 4(7):509-513.

99. Inoue T & Meyer T (2008) Synthetic activation of endogenous PI3K and Rac identifies an AND-gate switch for cell polarization and migration. *PLoS One* 3(8):e3068.

100. Sasaki AT, *et al.* (2007) G protein-independent Ras/PI3K/F-actin circuit regulates basic cell motility. *J Cell Biol* 178(2):185-191.

101. Bement WM, *et al.* (2015) Activator-inhibitor coupling between Rho signalling and actin assembly makes the cell cortex an excitable medium. *Nat Cell Biol* 17(11):1471-1483.

102. Weiner OD, *et al.* (1999) Spatial control of actin polymerization during neutrophil chemotaxis. *Nat Cell Biol* 1(2):75-81.

103. Wang Y, Senoo H, Sesaki H, & Iijima M (2013) Rho GTPases orient directional sensing in chemotaxis. *Proc Natl Acad Sci U S A* 110(49):E4723-4732.

104. Meinhardt H (1999) Orientation of chemotactic cells and growth cones: models and mechanisms. *J Cell Sci* 112 (Pt 17):2867-2874.

105. Cooper RM, Wingreen NS, & Cox EC (2012) An excitable cortex and memory model successfully predicts new pseudopod dynamics. *PLoS One* 7(3):e33528.

106. Shi C & Iglesias PA (2013) Excitable behavior in amoeboid chemotaxis. *Wiley Interdiscip Rev Syst Biol Med* 5(5):631-642.

107. Miao Y*, et al.* (2017) Altering the threshold of an excitable signal transduction network changes cell migratory modes. *Nat Cell Biol* 19(4):329-340.

108. van Haastert PJ, Keizer-Gunnink I, & Kortholt A (2017) Coupled excitable Ras and F-actin activation mediates spontaneous pseudopod formation and directed cell movement. *Mol Biol Cell* 28(7):922-934.

109. Arai Y*, et al.* (2010) Self-organization of the phosphatidylinositol lipids signaling system for random cell migration. *Proc Natl Acad Sci U S A* 107(27):12399-12404.

110. Lokuta MA*, et al.* (2007) Type Igamma PIP kinase is a novel uropod component that regulates rear retraction during neutrophil chemotaxis. *Mol Biol Cell* 18(12):5069-5080.

111. Wong R*, et al.* (2005) PIP2 hydrolysis and calcium release are required for cytokinesis in Drosophila spermatocytes. *Curr Biol* 15(15):1401-1406.

112. Balla T (2013) Phosphoinositides: tiny lipids with giant impact on cell regulation. *Physiol Rev* 93(3):1019-1137.

113. Nishio M*, et al.* (2007) Control of cell polarity and motility by the PtdIns(3,4,5)P3 phosphatase SHIP1. *Nat Cell Biol* 9(1):36-44.

114. Swaney KF, Borleis J, Iglesias PA, & Devreotes PN (2015) Novel protein Callipygian defines the back of migrating cells. *Proc Natl Acad Sci U S A* 112(29):E3845-3854.

115. Senoo H, Cai H, Wang Y, Sesaki H, & Iijima M (2016) The novel RacE-binding protein GflB sharpens Ras activity at the leading edge of migrating cells. *Mol Biol Cell* 27(10):1596-1605.

116. Loovers HM*, et al.* (2006) Distinct roles of PI(3,4,5)P3 during chemoattractant signaling in *Dictyostelium*: a quantitative in vivo analysis by inhibition of PI3-kinase. *Mol Biol Cell* 17(4):1503-1513.

117. Jeon TJ, Lee S, Weeks G, & Firtel RA (2009) Regulation of *Dictyostelium* morphogenesis by RapGAP3. *Dev Biol* 328(2):210-220.

118. Krause M*, et al.* (2004) Lamellipodin, an Ena/VASP ligand, is implicated in the regulation of lamellipodial dynamics. *Dev Cell* 7(4):571-583.

119. Wullschleger S, Wasserman DH, Gray A, Sakamoto K, & Alessi DR (2011) Role of TAPP1 and TAPP2 adaptor binding to PtdIns(3,4)P2 in regulating insulin sensitivity defined by knock-in analysis. *Biochem J* 434(2):265-274.

120. Bae YH*, et al.* (2009) Loss of profilin-1 expression enhances breast cancer cell motility by Ena/VASP proteins. *J Cell Physiol* 219(2):354-364.

121. Desponts C, Hazen AL, Paraiso KH, & Kerr WG (2006) SHIP deficiency enhances HSC proliferation and survival but compromises homing and repopulation. *Blood* 107(11):4338-4345.

122. Liu Q*, et al.* (1999) SHIP is a negative regulator of growth factor receptor-mediated PKB/Akt activation and myeloid cell survival. *Genes Dev* 13(7):786-791.

123. Bloomfield G*, et al.* (2015) Neurofibromin controls macropinocytosis and phagocytosis in *Dictyostelium*. *Elife* 4.

124. Xu X*, et al.* (2017) GPCR-controlled membrane recruitment of negative regulator C2GAP1 locally inhibits Ras signaling for adaptation and long-range chemotaxis. *Proc Natl Acad Sci U S A* 114(47):E10092-E10101.

125. Zhang S, Charest PG, & Firtel RA (2008) Spatiotemporal regulation of Ras activity provides directional sensing. *Curr Biol* 18(20):1587-1593.

126. Yoshida S, Hoppe AD, Araki N, & Swanson JA (2009) Sequential signaling in plasma-membrane domains during macropinosome formation in macrophages. *J Cell Sci* 122(Pt 18):3250-3261.

127. Dewitt S, Tian W, & Hallett MB (2006) Localised PtdIns(3,4,5)P3 or PtdIns(3,4)P2 at the phagocytic cup is required for both phagosome closure and Ca2+ signalling in HL60 neutrophils. *J Cell Sci* 119(Pt 3):443-451.

128. Sasaki AT, Chun C, Takeda K, & Firtel RA (2004) Localized Ras signaling at the leading edge regulates PI3K, cell polarity, and directional cell movement. *J Cell Biol* 167(3):505-518.

129. Stuelten CH, Parent CA, & Montell DJ (2018) Cell motility in cancer invasion and metastasis: insights from simple model organisms. *Nat Rev Cancer* 18(5):296-312.

130. Iijima M & Devreotes P (2002) Tumor suppressor PTEN mediates sensing of chemoattractant gradients. *Cell* 109(5):599-610.

131. Janetopoulos C, Ma L, Devreotes PN, & Iglesias PA (2004) Chemoattractant-induced phosphatidylinositol 3,4,5-trisphosphate accumulation is spatially amplified and adapts, independent of the actin cytoskeleton. *Proc Natl Acad Sci U S A* 101(24):8951-8956.

132. Pal DS, Li X, Banerjee T, Miao Y, & Devreotes PN (2019) The excitable signal transduction networks: movers and shapers of eukaryotic cell migration. *Int J Dev Biol* 63(8-9-10):407-416.

133. Parent CA, Blacklock BJ, Froehlich WM, Murphy DB, & Devreotes PN (1998) G protein signaling events are activated at the leading edge of chemotactic cells. *Cell* 95(1):81-91.

134. Luo HR*, et al.* (2003) Inositol pyrophosphates mediate chemotaxis in *Dictyostelium* via pleckstrin homology domain-PtdIns(3,4,5)P3 interactions. *Cell* 114(5):559-572.

135. Kay RR, Williams TD, & Paschke P (2018) Amplification of PIP3 signalling by macropinocytic cups. *Biochem J* 475(3):643-648.

136. Shellard A, Szabo A, Trepat X, & Mayor R (2018) Supracellular contraction at the rear of neural crest cell groups drives collective chemotaxis. *Science* 362(6412):339-343.

137. Postma M*, et al.* (2004) Sensitization of *Dictyostelium* chemotaxis by phosphoinositide-3-kinase-mediated self-organizing signalling patches. *J Cell Sci* 117(Pt 14):2925-2935.

138. Welliver TP & Swanson JA (2012) A growth factor signaling cascade confined to circular ruffles in macrophages. *Biol Open* 1(8):754-760.

139. Bretscher MS (1996) Getting membrane flow and the cytoskeleton to cooperate in moving cells. *Cell* 87(4):601-606.

140. Tanaka M*, et al.* (2017) Turnover and flow of the cell membrane for cell migration. *Sci Rep* 7(1):12970.

141. O'Neill PR*, et al.* (2018) Membrane Flow Drives an Adhesion-Independent Amoeboid Cell Migration Mode. *Dev Cell* 46(1):9-22 e24.

142. Somesh BP, Neffgen C, Iijima M, Devreotes P, & Rivero F (2006) *Dictyostelium* RacH regulates endocytic vesicular trafficking and is required for localization of vacuolin. *Traffic* 7(9):1194-1212.

143. Balest A, Peracino B, & Bozzaro S (2011) Legionella pneumophila infection is enhanced in a RacH-null mutant of *Dictyostelium*. *Commun Integr Biol* 4(2):194-197.

144. Goulden BD*, et al.* (2019) A high-avidity biosensor reveals plasma membrane PI(3,4)P2 is predominantly a class I PI3K signaling product. *J Cell Biol* 218(3):1066-1079.

145. Li X, Miao Y, Pal DS, & Devreotes PN (2020) Excitable networks controlling cell migration during development and disease. *Semin Cell Dev Biol* 100:133-142.

146. Ramalingam N*, et al.* (2015) A resilient formin-derived cortical actin meshwork in the rear drives actomyosin-based motility in 2D confinement. *Nat Commun* 6:8496.

147. Hasegawa J*, et al.* (2011) SH3YL1 regulates dorsal ruffle formation by a novel phosphoinositide-binding domain. *J Cell Biol* 193(5):901-916.

148. Zhou K, Pandol S, Bokoch G, & Traynor-Kaplan AE (1998) Disruption of *Dictyostelium* PI3K genes reduces [32P]phosphatidylinositol 3,4 bisphosphate and [32P]phosphatidylinositol trisphosphate levels, alters F-actin distribution and impairs pinocytosis. *J Cell Sci* 111 (Pt 2):283-294.

149. Wang H*, et al.* (2018) Autoregulation of Class II Alpha PI3K Activity by Its Lipid-Binding PX-C2 Domain Module. *Mol Cell* 71(2):343-351 e344.

150. Ghosh S*, et al.* (2018) Inhibition of SHIP2 activity inhibits cell migration and could prevent metastasis in breast cancer cells. *J Cell Sci* 131(16).

151. Czech MP (2000) PIP2 and PIP3: complex roles at the cell surface. *Cell* 100(6):603-606.

152. Roman-Fernandez A*, et al.* (2018) The phospholipid PI(3,4)P2 is an apical identity determinant. *Nat Commun* 9(1):5041.

153. Bryant DM*, et al.* (2014) A molecular switch for the orientation of epithelial cell polarization. *Dev Cell* 31(2):171-187.

154. Nelson WJ (2009) Remodeling epithelial cell organization: transitions between front-rear and apical-basal polarity. *Cold Spring Harb Perspect Biol* 1(1):a000513.

155. Martin-Belmonte F*, et al.* (2007) PTEN-mediated apical segregation of phosphoinositides controls epithelial morphogenesis through Cdc42. *Cell* 128(2):383-397.

156. Lee J, Gustafsson M, Magnusson KE, & Jacobson K (1990) The direction of membrane lipid flow in locomoting polymorphonuclear leukocytes. *Science* 247(4947):1229-1233.

157. Zoncu R*, et al.* (2009) A phosphoinositide switch controls the maturation and signaling properties of APPL endosomes. *Cell* 136(6):1110-1121.

158. Moreau HD*, et al.* (2019) Macropinocytosis Overcomes Directional Bias in Dendritic Cells Due to Hydraulic Resistance and Facilitates Space Exploration. *Dev Cell* 49(2):171-188 e175.

159. Millius A & Weiner OD (2009) Chemotaxis in neutrophil-like HL-60 cells. *Methods Mol Biol* 571:167-177.

160. Millius A & Weiner OD (2010) Manipulation of neutrophil-like HL-60 cells for the study of directed cell migration. *Methods Mol Biol* 591:147-158.

161. Drawert B, Engblom S, & Hellander A (2012) URDME: a modular framework for stochastic simulation of reaction-transport processes in complex geometries. *BMC Syst Biol* 6:76.

CURRICULUM VITAE FOR Ph.D. CANDIDATES

The Johns Hopkins University School of Medicine

Xiaoguang Li

11 20th, 2020

Educational History

Ph.D. expected	2020	Program in Biological Chemistry Mentor: Peter N. Devreotes, Ph.D.	Johns Hopkins School of Medicine
M.S.	2015	Medicine	Harbin Medical University
Bachelor	2013	Medicine	Harbin Medical University

Other Professional Experiences

ORISE Fellow 04/2020-07/2020 U.S. Food and Drug Administration

Scholarships, fellowships, or other external funding

American Heart Association (AHA) Predoctoral Fellowship, award ID 20PRE35211072, 01/2020-12/2021, $63,040

Academic and other honors

2018	Lewis Travel Award Cell Biology, Johns Hopkins School of Medicine
2019	Young Investigator (Bae Gyo Jung Award), Johns Hopkins School of Medicine

Publications

1. Xiaoguang Li, Dhiman Sankar Pal, et al. Reverse Fountain Flow of PI(3,4)P2 Polarizes Cells. EMBO J. 2020 (Accepted). *co-first author

2. Yang Liu, Roger Zou, Shuaixin He, Xiaoguang Li, et al. Very Fast CRISPR On Demand. Science. 12 Jun 2020; Vol. 368, Issue 6496

3. Xiaoguang Li, Yuchuan Miao, Dhiman Sankar Pal, Peter N. Devreotesa. Excitable networks controlling cell migration during development and disease. SCDB. doi: 10.1016/j.semcdb.2019.11.001

4. Dhiman Sankar Pal* & Xiaoguang Li*, Yuchuan Miao, et al. The excitable signal transduction networks: movers and shapers of eukaryotic cell migration. The International journal of developmental biology 63 (8-9-10), 407 (*Co-first author)

5. Xiaoguang Li, Marc Edwards, Kristen F. Swaney, et al. Mutually inhibitory Ras-PI(3,4)P2 feedback loops mediate cell migration. PNAS. 2018 Sep 25;115(39):E9125-E9134.

6. Zan Chen, Hanjie Jiang, Wei Xu, Xiaoguang Li, et al. A Tunable Brake for HECT Ubiquitin Ligases. Molecular Cell 66(3), 345-357.e6. 2017 (Featured article).

Posters, abstracts, *etc*.

1. *Dictyostelium* 2018 Annual International Conference, Amsterdam, The Netherlands, August 2018. (Oral)
2. Annual Biological Chemistry Departmental Retreat at JHSOM, Baltimore, Maryland, September 2018. (Oral)
3. The Conference for International Joint Laboratory of the Ministry of Education, Heilongjiang Province, China, June 2018. (Oral)
4. 2019 Annual Meeting - Biophysical Society, Baltimore, Maryland, March 2019. (Poster)
5. ASCB | EMBO 2019 Meeting, Washington, D.C., Maryland, December 2019. (Poster)
6. 2019 Gordon Research Conference (GRC) on Directed Cell Migration, Galveston, Texas, January 2019. (Poster)
7. DARPA Biological Control Annual meeting, San Francisco, California, July 2018. (Poster)
8. ASCB | EMBO 2017 Meeting, Philadelphia, Pennsylvania, December 2017. (Poster)
9. 2017 Gordon Conference on Molecular Membrane Biology, Andover, New Hampshire, July 2017. (Poster)

Inventions, patents, and copyrights

N/A

Service and leadership

2019-present	Review Editor for scientific peer-review journals: *1) Frontiers in Medicine*, section Translational Medicine, 2) *Nanobiotechnology*: *Frontiers Bioengineering and Biotechnology, Frontiers in Molecular Biosciences*
2018	Teaching assistant, Cell Physiology for Johns Hopkins medical school
2017-present	Has reviewed for journals: 1) Molecular Therapy - Nucleic Acids, 2) Breast Care, 3) Frontiers in Medicine, section Translational Medicine, 4) Cancer Translational Medicine, 5) International Journal of Biological Sciences, 6) Biomolecules, 7) American Journal of Translational Research, 8) Cells 9) Frontiers in Bioscience, 10) Cellular Physiology and Biochemistry, 11) Phytomedicine 13) Non-Coding RNA-MDPI 13) Epigenomes 14) International Journal of Environmental Research and Public Health 15) Cell Biology International 16) Acta Pharmaceutica Sinica B
2019	Discussion leader for the Keynote session, 2019 Gordon Research Seminar (GRS) on Directed Cell Migration, USA
2018	Chair, Annual Biological Chemistry Department Retreat, JHSOM